LONG RANGE ORDERING IN POLY(3-HEXYLTHIOPHENE) FLUIDS AND FILMS: IMPLICATIONS FOR ORGANIC ELECTRONICS

A Dissertation
Presented to
The Academic Faculty

by

Nabil Kleinhenz

In Partial Fulfillment
of the Requirements for the Degree
Doctor of Philosophy in the
School of Chemistry and Biochemistry

Georgia Institute of Technology
December 2016

LONG RANGE ORDERING IN POLY(3-HEXYLTHIOPHENE) FLUIDS AND FILMS: IMPLICATIONS FOR ORGANIC ELECTRONICS

Approved by:

Dr. Elsa Reichmanis, Advisor
School of Chemical and Biomolecular Engineering
Georgia Institute of Technology

Dr. John Reynolds
School of Chemistry and Biochemistry
Georgia Institute of Technology

Dr. Mohan Srinivasarao
School of Materials Science and Engineering
Georgia Institute of Technology

Dr. David Collard
School of Chemistry and Biochemistry
Georgia Institute of Technology

Dr. Jean-Luc Brédas
School of Materials Science and Engineering
King Abdullah University of Science and Technology

Date Approved: November 2, 2016

To our son, Badi, and any other children we may be blessed to have.

ACKNOWLEDGEMENTS

I would like to thank all of the family, friends and coworkers who have supported me over these past five years and throughout my life. My advisor, Elsa Reichmanis, has been incredibly kind, patient and sincerely invested in my education. I feel her approach of giving her students freedom to independently investigate the questions they have is very empowering. My coworkers and friends Ping-Hsun Chu, Nils Persson, Mike McBride, Zongzhe Xue, Jamilah Middlebrooks, Eugenia Kim, Dalsu Choi, Gang Wang, Talanna Ruffin, Zhibo Yuan, Ji-Hwan Kang, Jeff Hernandez, Bailey Risteen, Giovanni DeLuca, Yo Han Kwon, Krysten Minnici, Guoyan Zhang, Avishek Aiyar, Rui Chang, Karthik Nayani, Jinxin Fu, Mincheol Chang, Cornelia Rosu and many others have been always willing to help, have shared enlightening discussions with me and were always so kind to assist in my experimental work. My committee members, Mohan Srinivasarao, John Reynolds, Jean-Luc Brédas and David Collard have all been very giving of their time and have generously offered valuable expertise and feedback. I relied heavily on the knowledge I gained in Dr. Brédas' fantastic Organic Electronics course, including in writing sections of the introduction to this thesis. I also thank Junk Ok Park and Paul Russo for the many helpful and encouraging conversations. In terms of financial support, I am grateful for trainee support from the NSF IGERT on Nanostructured Materials for Energy Storage and Conversion, the COPE Felloswhip, a Georgia Tech GoSTEM teaching fellowship, and the Sam Nunn Security Fellowship. I thank Sourav Chatterjee and Cornelia Rosu for their dynamic light scattering measurements. I also appreciate the efforts of Jibao He (Tulane University) for his help with cryo-TEM experiments. I would like to thank Gang Wang and

Zhibo Yuan who were gracious enough to characterize my samples with GIWAXS measurements. I also thank the many excellent and caring teachers who trained me throughout my whole life, including my AP Chemistry teacher, Ms. Watt who taught the course so well that I felt I could do well in chemistry as my college major. Lastly, I am also thankful to God for the blessing of having such a loving network of family and friends in my life. My dear wife, Jasmine, has been so joyful, strong and supportive during this whole journey. My brothers and sisters, both blood-related and not, have always been so caring, understanding and inspiring. I would like to thank Russell George for being a trusted mentor and for helping guide me on a path of serving others and striving for excellence. Finally, I am eternally grateful to my loving parents, who were both teachers, and who instilled in me, among many other things, a deep appreciation for the importance of education: “Regard man as a mine rich in gems of inestimable value. Education can, alone, cause it to reveal its treasures and enable mankind to benefit therefrom.” -Bahá’u’lláh

TABLE OF CONTENTS

LIST OF TABLES

LIST OF FIGURES

LIST OF SYMBOLS AND ABBREVIATIONS

P3HT	Poly(3-hexylthiophene)
HOMO	Highest Occupied Molecular Orbital
LUMO	Lowest Unoccupied Molecular Orbital
POM	Polarized Optical Microscopy
AFM	Atomic Force Microscopy
OPV	Organic Photovoltaic
OLED	Organic Light Emitting Diode
OFET	Organic Field Effect Transistor
W	Bandwidth
μ	Charge Carrier Mobility
LC	Liquid Crystal
LLC	Lyotropic Liquid Crystal
TCB	Trichlorobenzene
$CHCl_3$	Chloroform

SUMMARY

Understanding and controlling polymer semiconductor morphology is critical to achieving high charge carrier mobility and enabling widespread use of organic electronic devices such as organic photovoltaics, organic light-emitting diodes and organic field-effect transistors (OFETs). In the studies described herein, *micro*- and *macro*-scale ordering of model conjugated polymer poly(3-hexylthiophene) (P3HT) were achieved both in the solution state and film state and the impacts on charge transport were explored. The self-assembly of P3HT through solution aging over time formed long nanofibers that can align in the fluid state, as monitored by polarized optical microscopy, and polarized Raman spectroscopy. When induced by ultrasonication, the fibers that formed were significantly shorter than with aging and it was discovered that the length of these fibers played a critical role in their ability to align, and maintain alignment in the solid state. The *micro*structural features formed through these solution processing techniques, as determined by atomic force microscopy, were correlated with enhanced field-effect mobility as measured by OFETs. More controlled alignment of P3HT nanofibers was then explored through blade coating, a technique less wasteful than spin coating and more amenable to roll-to-roll fabrication. P3HT nanofibers were successfully aligned over large areas (tens of millimeters), enabling the investigation of *macro*-scale orientational ordering on charge transport anisotropy, and giving insight into the important roles of both intra- and intermolecular charge transport in P3HT nanofiber films for organic electronics applications.

CHAPTER 1. INTRODUCTION

Due to their light-weight nature, mechanical flexibility, low cost and solution processability, organic (carbon-based) electronics offer a wide range of benefits when compared with traditional inorganic semiconductor materials. The ability to process organic materials from solution allows for advantageous deposition methods such as screen printing, ink-jet printing, micro-contact printing and large scale, low cost roll-to-toll fabrication techniques.[1] These methods do not require high temperatures and are thus amenable to a wide variety of substrate materials including polymers. Thin-film organic active layers can be used in flexible, light-weight organic photovoltaics (OPV) for cost-effective, and clean renewable energy from the sun.[2,3] Organic light emitting diodes (OLED), are already used for displays in readily available technologies such as in smartphones and televisions and have a future in energy-efficient lighting.[4,5] Organic field effect transistors (OFET) have reached charge carrier mobilities comparable to amorphous silicon and could be used to drive flexible displays among other technologies.[6,7] The flexibility of the organic active layers enables countless other applications including flexible integrated circuits, electronic paper, electronic skin and more.[1] Continued improvements in charge carrier mobility, stability, and reproducibility at a larger scale will be essential to realizing the widespread production and use of these technologies (Figure 1.1).

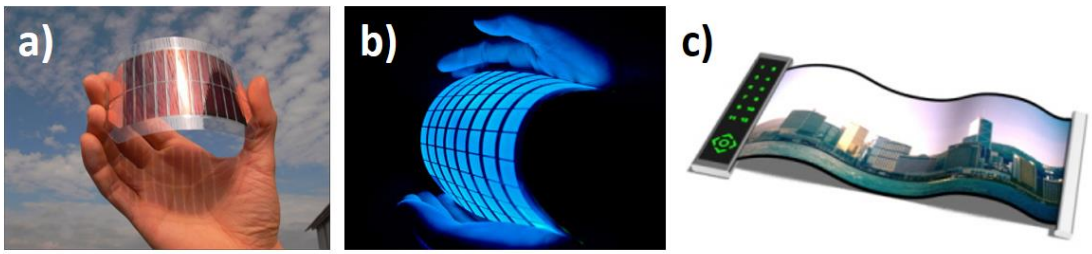

Figure 1.1 Examples of Organic Electronic Devices: a) Organic Photovoltaics (OPV), b) Organic Light Emitting Diodes (OLED), and c) futuristic flexible display driven by Organic Field-Effect Transistors (OFET). Sources.[8–10]

1.1 Brief History of Organic Semiconductors

Early discoveries hinted at the great possibilities for organic electronic materials. These findings include the 1958 report that magnesium pthalocyanine disks coated with a thin film of air-oxidized thetramethyl p-phenylenediamine showed the photovoltaic effect, harvesting light to produce electric current.[11] In 1955, electroluminescence was demonstrated in organic compounds including acriflavine, brilliant acridine orange E and carbazole as adsorbants on cellulose films which were fluorescent when mounted on dielectric cells with a voltage applied.[12] However, during the sixties, the prevailing thought among scientists was that organic materials could not be electrically conducting. This conventional wisdom was shattered in the 1970's by discoveries of the electrical properties of two classes of materials – small molecules and polymers. The first class includes families of small molecule organic molecular crystals including the electron transfer complex TTF-TCNQ (Figure 1.2) composed of electron donor tetrathiofulvalene (TTF) and electron acceptor tetracyano-*p*-quinodimethane (TCNQ)[13] along with the TMTSeF family.[14] These crystals, formed from molecular stacks, have not been heavily utilized in applications because their synthesis is a very involved process, possibly requiring months

to carry out. While small molecules continue to be heavily utilized today, what really accelerated the field of what we call organic electronics was the discovery of electrically conducting polymers.

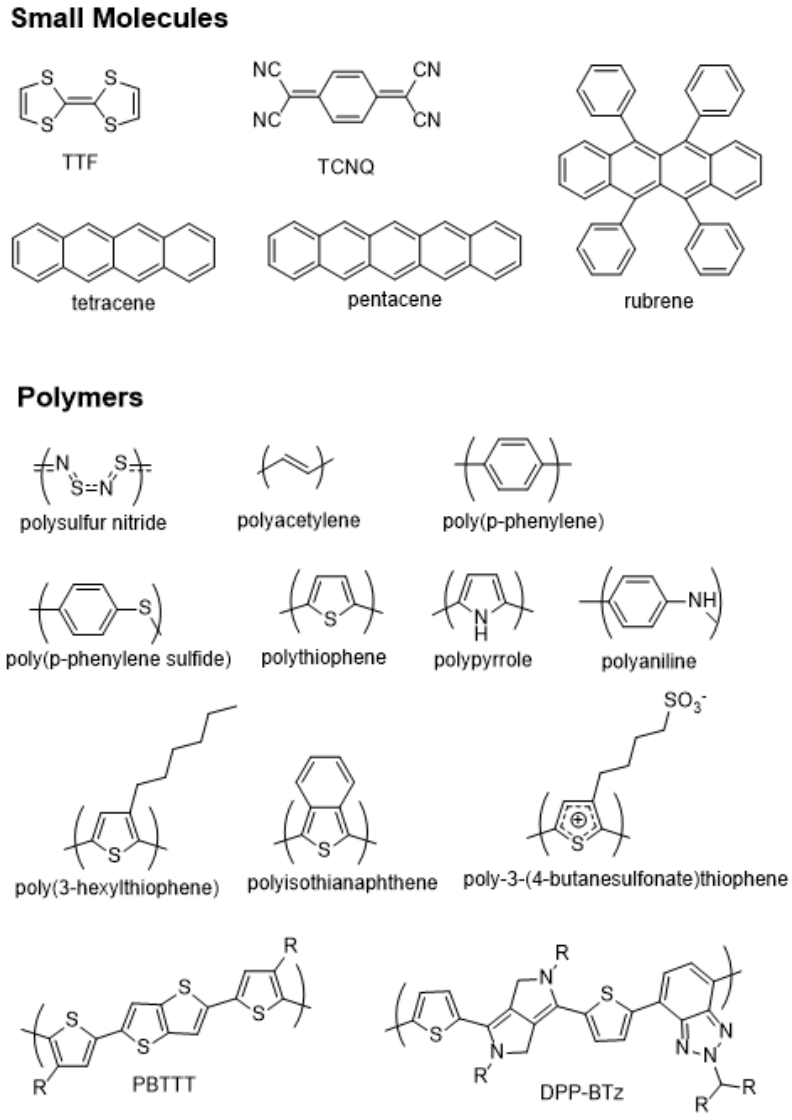

Figure 1.2. Small sample of organic semiconductors including small molecules and polymer chains.

1.1.1 Conductive Polymers

The first polymer credited to behave as a metal was polysulfur nitride or (SN)x, synthesized to have a room temperature conductivity of 10^3 S/cm in 1973,[15] and which was shown to be superconductive in 1975 at a critical temperature of 0.3 K.[16] When pure (SN)x is exposed to vapors of halogens, the room temperature conductivity goes up by an order of magnitude due to redox reactions. The synthesis of (SN)x, however, can lead to explosions. The first discovery of high electrical conductivity in a conjugated organic polymer was in 1977 when researchers, led by Hideki Shirakawa, Alan Heeger and Alan MacDiarmid showed that polyacetylene becomes highly conducting when electron donating or accepting molecules are added, facilitating redox reactions.[17] By exposing polyacetylene to the vapors of strong oxidants, conductivities increased by many orders of magnitude. This is due to removal of electrons that make the polymers polycations (with counterions remaining in the material). It was soon discovered that other conjugated polymers could be made highly conducting through doping including poly(p-phenylene),[18] poly(p-phenylene sulfide),[19] poly(pyrrole),[20] poly(thiophene)[21] and poly(aniline).[22] Between 1986 and 1987 a major development occurred when Sato et al. and Elsenbaumer et al. made polythiophenes soluble in common organic solvents by adding an alkyl side chain at least 4 carbons long on the 3 position, creating poly(3-alkylthiophenes).[23,24] With the side chain additions came more processing methods in solution due to solubility in organic solvents and processing from the melt due to lower melting points. The electrical properties of these semiconducting polymers could now be combined with the processability of more common plastics, opening the way for ink-jet printing, deposition on a variety of substrates at low temperatures, and mechanical flexibility.

1.1.2 Semiconducting Polymers

Eventually there was a shift in the focus of research from highly conducting polymers to semiconducting polymers. While field-effect transistors had been in use for decades, beginning with metal-oxide-semiconductors (MOSFET) in 1960,[25] in 1990 Garnier et al. developed the first all-organic field-effect transitor (OFET),[26] and the same year the group of Richard Friend used poly(*p*-phenylene vinylene) to develop the first polymer organic light-emitting diode (OLED).[4] C. W. Tang developed a two-layer organic solar cell in 1986 from copper phthalaocyanine and a perylene tetracarboxylic derivative.[2] After other developments in the field of organic photovoltaics (OPV), Heeger et al. and Yoshino et al. independently demonstrated electron transfer between a conjugated polymer and fullerene derivatives in the 1990s,[27,28] which accelerated the research into bulk-heterojunction solar cells for potentially cheap, flexible, lightweight, printable and tunable solar photovoltaic materials. The last few decades have seen much attention given to developing new semiconducting polymers for OPV, OLED, OFET and other applications in both academic and industrial pursuits. The most prominent example is OLEDs which have become established technologies in displays for smartphones, televisions and other widely available devices.[29]

In the year 2000, the Nobel prize in chemistry was awarded to Heeger, Shirawaka and MacDiarmid for their original work in the 1970s and beyond, for the "discovery and development of conducting polymers."[30] Conjugated polymers have since continued to attract much attention along with small molecule organic semiconductors. Further synthetic efforts[31] have yielded high mobility polymers incorporating polythiophenes, bridged and fused rings, diketopyrrolopyrrole (DPP), isoindigo and other moieties, often

incorporating electron donating and accepting moieties, giving reported mobilities of tens of $cm^2V^{-1}s^{-1}$.[32] However, morphological control achieved through processing and deposition methods that can fine-tune alignment and molecular packing (microstructure) have been just as crucial as synthetic developments in advancing high performance organic electronics.[33] This research on control and understanding of morphology of semiconducting polymer films is also important from the standpoint of reproducibility, as processing and deposition methods of semiconducting polymers (which significantly impact final film morphology) are translated from the laboratory setting to large scale fabrication techniques. Much work remains to realize the full potential of these promising materials, especially in improving charge carrier mobility, reproducibility and shelf life, environmental stability and scalability in both synthesis and printing techniques.[34] In particular, the morphology of the polymeric semiconductors plays a key role in the charge transport and the control and understanding of this morphology and its role in charge transport is the focus of this thesis.

1.2 Charge Transport in Organic Semiconductors

The ability to transport charge carriers efficiently through the organic π-conjugated material is paramount to achieving high performing organic electronic devices. In OFETS, the faster the charges can move through organic semiconducting channel, the faster the transistor can be switched. Therefore, charge carrier mobility is an important factor, defined as the speed that the charges move per applied field. In the quest for flexible electronics, the target mobility is to at least have charge carrier mobilities as high as amorphous silicon (which could compete with transistors based on amorphous silicon in displays) which has a mobility on the order of 1 $cm^2V^{-1}s^{-1}$. In the case of organic transistors

and light-emitting diodes, the charges are injected from an external source, while in the case of organic solar cells, charges are generated through the dissociation of excitons formed by the absorption of photons. The organic semiconducting material is composed of a π-conjugated molecule that is either 1) a small molecule or oligomer, usually processed by vacuum deposition or 2) a polymer which is usually processed from solution.[35] Small molecules can also be processed from solution and achieve highly crystalline morphologies with high charge carrier mobilities, but tend to be more brittle and not as robust for applications on flexible substrates compared with polymeric semiconductors.[3]

1.2.1 Conjugation and its Effects

It is useful to examine the chemical structure of conducting and semiconducting polymers in order to understand why these materials can conduct charges when the vast majority of commercial polymers in use behave as insulators. Figure 1.3, comparing the differences in bonding in saturated ethane vs. unsaturated ethene illustrates that in saturated organic polymers, all four valence electrons on each carbon are used up in the covalent bonds. In conjugated polymers, however, the alternating double and single bonds along the backbone lead to one unpaired π-electron per carbon atom. Furthermore, π-bonding occurs where the p orbitals in the sp^2p_z configuration overlap along successive carbon atoms down the backbone of the polymer. This overlapping of p_z orbitals provides for electron delocalization which turns the polymer backbone into a "highway" for charge mobility.[36,37] The electronic structure is determined by the number and kinds of atoms within the repeat units, resulting in semiconducting or possibly metallic properties.

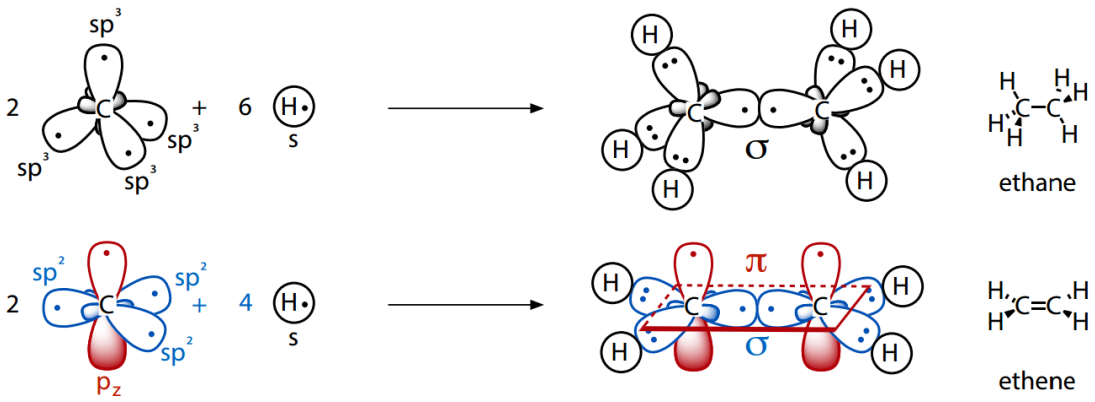

Figure 1.3 Difference between orbital arrangements and electron sharing in saturated ethane vs. unsaturated ethane molecule, demonstrating π-bonding as key factor in forming overlapping p orbitals resulting in path for electron delocalization along backbone. Source.[38]

As more carbons are added and the conjugation length increases, the energy gap between the highest occupied molecular orbital (HOMO) and the lowest unoccupied molecular orbital (LUMO) decreases.[39] To illustrate this point, the electronic structures of ethylene, butadiene and octatetraene are compared **(**Figure 1.4) where the energy levels of the π and π* molecular orbitals are depicted, and increasing numbers of nodes in the wave functions correspond to higher energies. In the case of ethylene, the first optical transition from the HOMO to LUMO requires approximately 6.7 eV of energy. In the case of butadiene (essentially an interaction between two ethylene subunits), the first optical transition occurs with about 5.8 eV of energy, because of the additional splitting of the π and π* levels, bringing the HOMO up and the LUMO down. For octatetraene, with 4 occupied π levels and 4 unoccupied π* levels, further splitting occurs such that the gap between the HOMO and LUMO is reduced to 3.1 eV. To a first approximation, the energy of this first π to π* transition continues to decrease as a function of 1/n where n = the number of carbon atoms. It is important to note that if all the bond lengths were of equal

length in polyacetylene, the π and π* would become degenerate, resulting in a metallic situation (no gap between the HOMO and LUMO). However, Peierls Theorem states that a quasi one-dimensional metal (as polyacetylene can be treated) is always unstable with respect to a geometry modification, also known as Peierls distortion.[40] The bond length alternation leads to symmetry lowering and removal of degeneracy of the HOMO and LUMO, and the appearance of a semiconducting state. It is also important to note that the energy difference between consecutive π levels [π* levels] also decreases such that for an infinite chain, this difference becomes infinitely small, leading to continuous zones for the π levels and the π* levels, or the formation of *energy bands*. The π-Band is referred to as the valence band and the π*-Band is referred to as the conduction band. The energy between the top of the valence band (ionization potential) and the bottom of the conduction band (electron affinity) is the energy gap for the first optical transition (~1.5 eV for polyacetylene). Electrons need to be excited into the conduction band in order to have conductivity. Chemical modification by incorporating electron rich or electron withdrawing groups on the backbone can alter this energy gap by making it easier or more difficult to oxidize a chain.

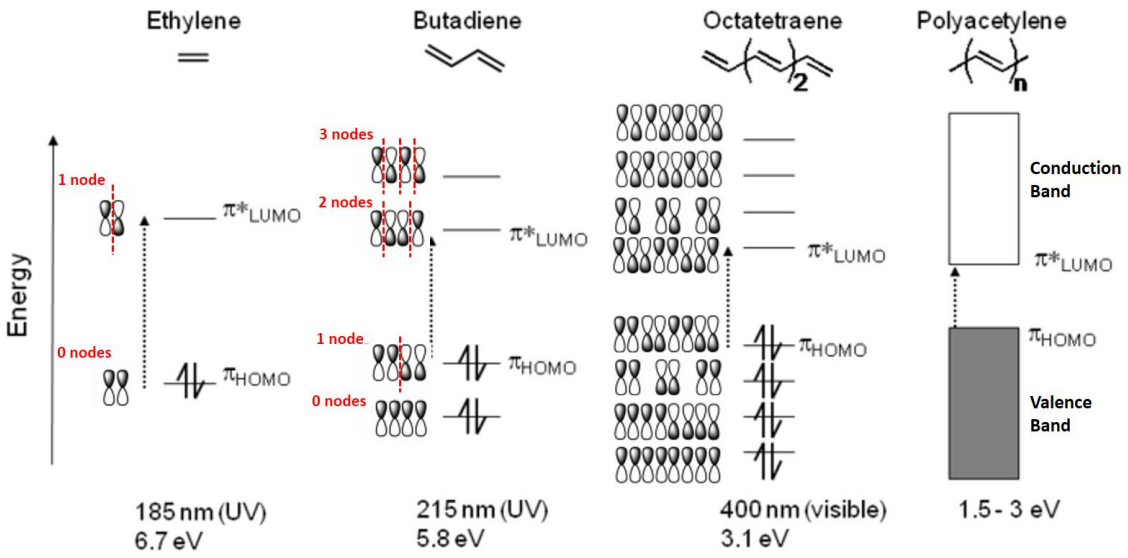

Figure 1.4 Wave functions of a conjugated segment showing energy level splittings for π molecular orbitals with the addition of conjugated subunits. With a large number of splittings, formation of valence band (bottom band) and conduction band (top band) occurs - adapted from references.[39,41]

1.2.2 Modes of Charge Transport in Organic Semiconductors

The two extremes of the spectrum for charge transport mechanisms in an organic material are the *band regime* and the *hopping regime*.[35,42,43] The band regime involves the charge carrier (wave function) being delocalized over the whole molecule or system, resulting in coherent transport. The hopping regime, on the other hand, involves a localized charge carrier on a single molecule which can be transferred to other molecules or chain segments by thermally activated "hopping." In the hopping regime, the mobility can be directionally dependent, as a function of the overall orientation of the molecules, which will prove to be a significant factor in Chapter 4. Whether charge is transported via the band regime or the hopping regime depends on the strength of the electronic coupling, *t*, (wavefunction overlap, dependent on intermolecular distance and positioning), and the strength of the electron-vibration coupling (dependent on the extent of the geometry

relaxations when the molecules goes from a neutral to ionized state). Electron-vibration coupling is a description of the connection between electronic structure and geometric structure. When a charge is injected into a molecule, bringing it to an ionized state, the optimal geometry of the ionized state is different from the optimal geometry of the neutral state because when the electronic state is modified, the π-bond densities change, which modifies the bond lengths.

The band and hopping regimes can be distinguished from the perspective of both the time domain and the energy domain. For the time domain, a charge resides on a molecule for a certain residence time, τ, which is proportional to the inverse of the bandwidth (W). The bandwidth is directly related to the electronic coupling between adjacent molecular units. With ħ (h/2π) in units of energy (eV) and the bandwidth in eV, the result is that the residence time, τ can be expressed in Equation 1.1 as:[43]

$$\tau \approx \frac{\hbar}{W} \rightarrow \tau \approx \left(\frac{2}{3}\right) \frac{10^{-15}}{W_{(eV)}} s \tag{1.1}$$

If the residence time is shorter than the fastest vibration in the system, there will not be enough time for the molecule to geometry relax, and therefore, band transport will be possible. This would occur in the case of a highly ordered material with strong coupling between molecules, giving sufficiently large bandwidths (for holes, the valence bandwidth, and for electrons, the conduction bandwidth). Considering the stretching frequency of C=C bonds, if the residence time is on the order of 10^{-14} s, then band transport is possible. If a simple tight-binding approximation is used, the bandwidth is about 4 times the electronic coupling between, t, between adjacent sites:[44]

$$W \approx 4t \tag{1.2}$$

The electronic coupling, *t*, is also referred to as the transfer integral or the tunneling matrix element. This relationship between bandwidth and electronic coupling is demonstrated in Figure 1.5 with the example of perfect stacks of pentacene molecules. To secure a band regime, not only is a well-ordered system required, but the electronic coupling must be large enough such that the bandwidths are at least a few tenths of an eV, and result in greater stabilization of a charge than if the charge were to reside on a single molecule for enough time to allow geometry relaxation to take place.[43] Thus, the distinction between band and hopping regimes can also be made from an energy perspective.

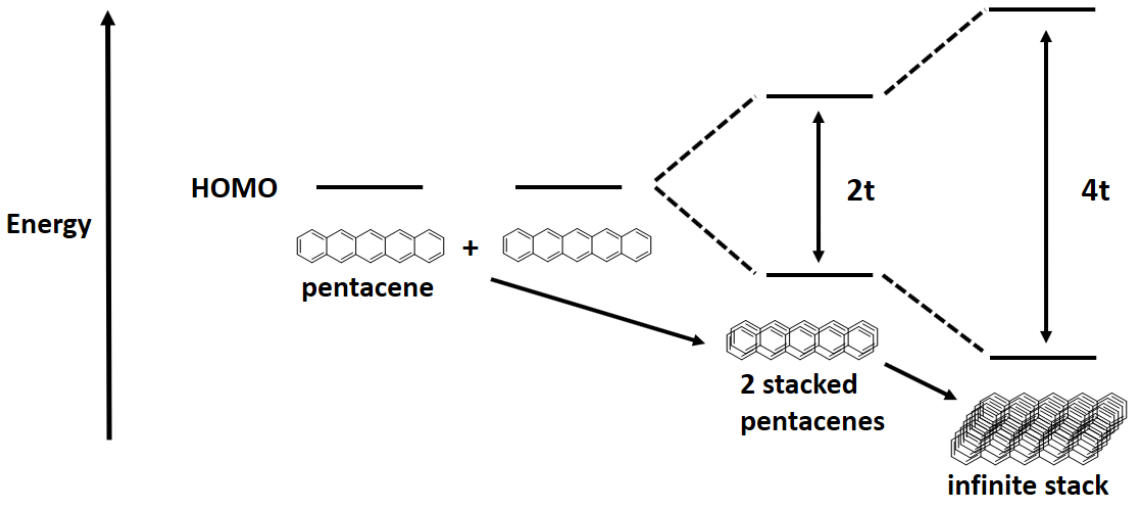

Figure 1.5 Energy level splittings as a result of electronic coupling between adjacent pentacene molecules.

Just as was demonstrated in Figure 1.4 with the example of bringing together ethylene subunits which were covalently bound, leading to splitting of the HOMO and LUMO, the same principle applies to the intermolecular interaction of individual organic

semiconducting molecules brought together to form a molecular crystal (Figure 1.5). As two molecules approach each other, their wavefunctions begin to overlap, and the electronic coupling results in splitting of the HOMO and LUMO (only the HOMO is shown in Figure 1.5) with a total energy splitting of 2*t*. As more molecules are added, such that an infinite one-dimentional stack of pentacene molecules is formed, a band is formed (pictured is the valence band) with width approximately equal to 4*t*. If molecules do not have any electronic coupling between them and an electron is injected into the system, the electron will reside in the LUMO of that molecule. When coupling occurs and a band has formed, the electron instead travels to the bottom of the band, resulting in an energy lowering (stabilization) of the system, which is directly related to the extent of electron delocalization (wavefunction overlap and electronic coupling) in the system. If this energy lowering through delocalization is greater than what would be achieved through geometry relaxation as a result of localization of the charge on a single molecule (polaron formation), then the band regime can occur.

For systems in which rotation along the polymer backbone is prevented, such as a ladder polyparaphenylene, the value of t along the chain can be approximately 2 eV, and as a result, instrinsic mobility along the chain has been shown to reach 600$cm^2V^{-1}s^{-1}$.[45] This can also be the case in polydiacetylene where macroscopic coherence of a single isolated polydiacetylene chain was observed over tens of microns.[46] Highly ordered covalently bound sp^2 hybridized carbon systems can give mobilities on the order of 10^5 $cm^2V^{-1}s^{-1}$ for carbon nanotubes[47] and epitaxial multilayer graphene,[48] and 10^4 $cm^2V^{-1}s^{-1}$ for bulk graphite.[49] In crystalline or well-ordered polymeric materials and nanotubes, the transfer integral *along* the chains can reach between 2.0 and 3.0 eV, but since in practical

applications the individual molecules do not span distance between the electrodes, charges have to hop from one molecule to another eventually in order to make it to the other electrode. Therefore, in molecular crystals, the *inter*chain coupling becomes important, which is typically at least an order of magnitude lower than the *intra*chain coupling. Due to the small intermolecular coupling, the localization energy can compete easily with the delocalization energy and hopping regime becomes more easy to sustain than the band regime, especially at increasing temperatures.

The bandwidths illustrated in Figure 1.5 assume a perfect equilibrium geometry at a sufficiently low temperature for a frozen lattice. As the temperature goes up, the molecules vibrate with greater amplitude, and the increased disorder effectively leads to a decreased bandwidth.[50] If band regime transport was previously occurring, the increased temperature will gradually lead to a transition to a hopping mechanism. Additionally, intermolecular coupling depends greatly on the distance between molecules. As shown in Figure 1.6, as two perfectly cofacial molecules are brought closer together, the splitting increases exponentially.[43] Even though perfectly cofacial alignment is rarely preferred in reality due to repulsion between the same regions of electron density on each molecule, this increase in the coupling corresponds to the increase in wavefunction overlap between the molecules as their molecular planes approach each other. This perfectly cofacial situation results in the largest wavefunction overlap, but molecules in reality will slide with respect to each other, leading to dramatic oscillation in coupling.[43]

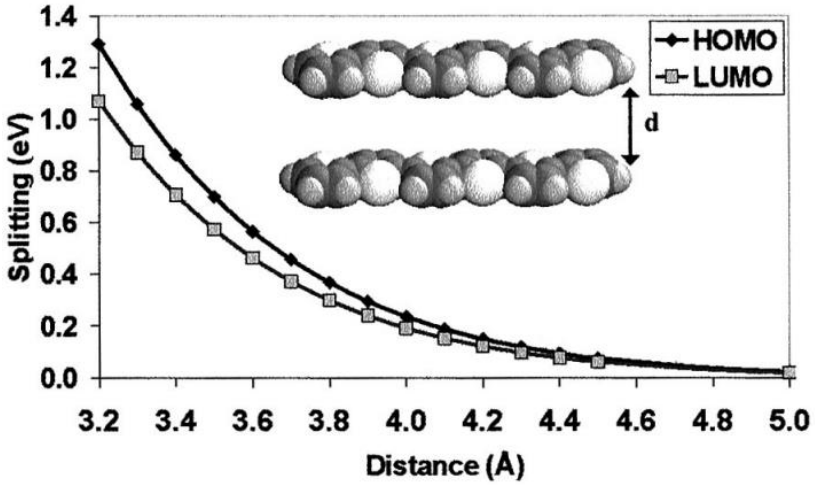

Figure 1.6 Example of splitting (2t) dependence on intermolecular distance (d) using perfectly co-facial pentacene molecules. Copyright (2002) National Academy of Sciences.[43]

In summary, for the band regime to exist, a highly ordered structure is required (a crystal) with large electronic coupling, at low temperatures so that the amplitudes of vibrations are small, and with as few impurities as possible. While the band regime would give the fastest possible charge carrier mobilities, it is in practice difficult to achieve for polymeric semiconductors due to highly crystalline nature required and the large number of defects and / or amorphous regions in a polymeric thin film that spans microns required for macro-electronic devices. Therefore, the hopping regime is most typically the dominant form of transport in polymer systems. In both the band regime and the hopping regime, mobility depends strongly on the electronic coupling. Therefore, maximizing coupling is desired for the fastest mobilities. Indeed, in the context of Marcus electron transport theory, described later in this section, the hopping rate depends on the square of the electronic coupling.[35,51]

When a charge localizes on a molecule or polymer segment due to the removal of an electron, a radical cation is formed referred to as a polaron (in this case a hole polaron) (Figure 1.7). A further removal of an electron results in the formation of a bipolaron (although the distance between charged species may be greater than depicted). These charges move along the backbone and can hop between chains resulting in charge transport described by Marcus Theory below.

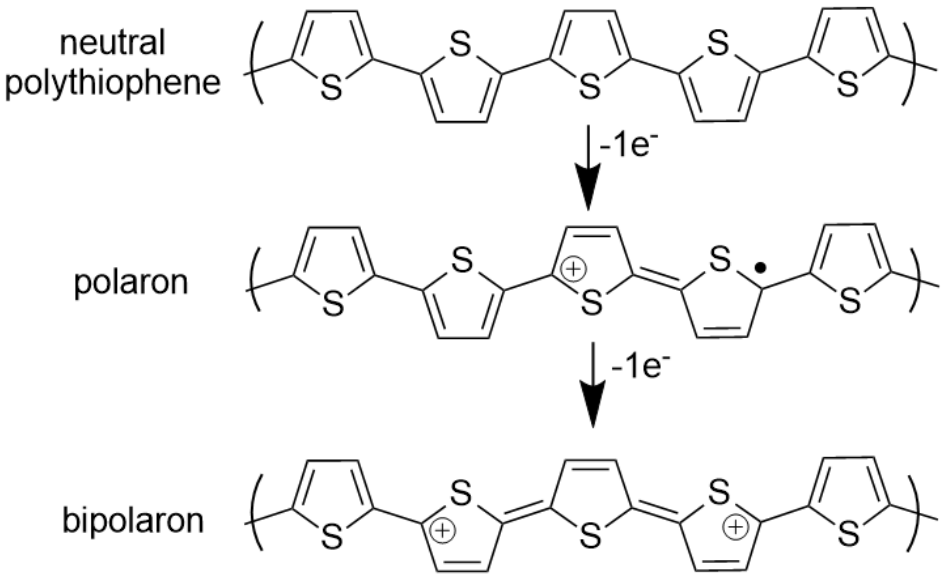

Figure 1.7 Polaron formation in polythiophene.

As illustrated by the simple electron transfer reaction in Figure 1.8, when an electron hops from one molecule to the other, the first molecule relaxes back to the geometry of the neutral state, and the second molecule gains an electron, going from the neutral to anionic state, and relaxes into the optimum geometry of the anionic state, undergoing "reorganization."

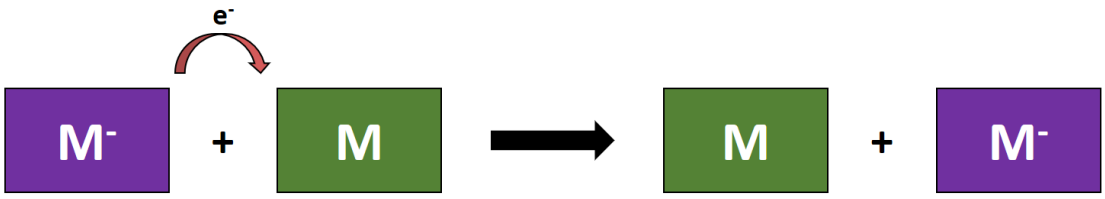

Figure 1.8 Self exchange reaction illustrating the electron transfer process between two molecules.

This electron transfer can be cast in the form of a chemical reaction, in which the reactants are (M^- + M) and products are (M + M^-), referred to as a self-exchange reaction. The Marcus model of electron transport, shown below, predicts how the electron transfer rate depends on coupling, temperature and reorganization energies.[35,51]

$$k_{ET} = t_{ab}^2 \sqrt{\frac{\pi}{h^2 k_B T \lambda}} \exp\left\{-\frac{(\Delta E + \lambda)^2}{4\lambda k_B T}\right\} \quad (1.3)$$

Where t_{ab} is the transfer integral (coupling), h is Planck's constant, k_B is Boltzmann's constant, T is temperature, λ is reorganization energy and ΔE is the driving force. As can be seen in equation 1.3, maximizing the coupling and minimizing the reorganization energy is desirable in order to improve the electron transfer rate. It is important to note that the rate of electron transfer, $k_{ET,}$ depends on the vibrational modes involved in both the intramolecular (λ_s) and intermolecular (λ_i) reorganization energies, which are further elaborated in the Marcus-Levich-Jortner Model.[52,53] Intramolecular reorganization energy refers to the shifting of electron densities within a molecule, while intermolecular reorganization involves the slight shifting of the positions of molecules relative to one

another as a result of the transfer of an electron from one molecule to the next (due to the new anion slightly repelling neighboring molecules).

1.2.3 Morphology and Impact on Charge Transport

Knowledge of the morphology of the semiconductor is highly important in understanding charge carrier mobility results. While difficult to achieve, single crystals have been generated and studied, giving rise to mobilities well over the 1 $cm^2V^{-1}s^{-1}$ amorphous silicon benchmark due to the near perfect packing of the molecules and high electronic coupling.[54–56] But over length scales large enough for most practical applications, polycrystalline morphologies are present, composed of multiple crystalline grains with grain boundaries in between that limit charge carrier mobility. Semicrystalline polymers have domains that are crystalline and domains that are amorphous. It is also possible for polymeric semiconductors to be very disordered (amorphous) and in some cases is desirable as in the case of LEDs in which disordered active layers are desired to prevent scattering. Impurities also affect mobility, such as the presence of oxygen and water which trap electrons.

The nature of the grain boundaries and the size of the crystallites will influence the mobility in OFETs. It is difficult to have a sample that is completely free of impurities (for instance, metal catalysts can be left over from polymerization). For polymers that have a tendency to form crystallites or well-ordered aggregates, such as polythiophenes,[57] the resulting films can be semicrystalline, with crystallites embedded in an amorphous matrix. In the case of P3HT, enhancing crystallite (nanofiber) formation has been a critical factor

in improving mobility compared to amorphous P3HT.[58–60] A nanofiber morphology of P3HT is shown schematically in Figure 1.9.

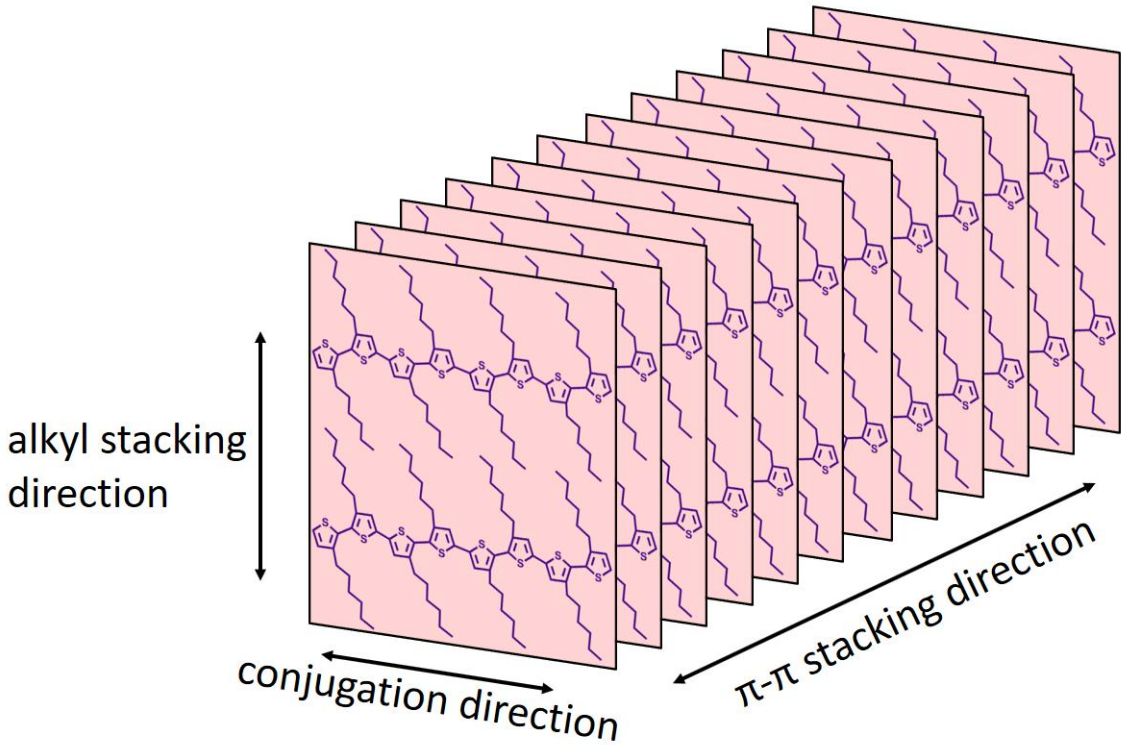

Figure 1.9 P3HT chains showing possible charge transport pathways 1) between lamellar stacks which is unlikely due to the presence of insulating side chains, 2) hopping between π-stacked chains (intermolecular charge transport) and 3) intramolecular charge transport along the conjugated backbone.

Charge carrier mobility is anisotropic, with the fastest mobility along the conjugation direction (Figure 1.9) on the polymer backbone.[35,42,61] The π-π stacking direction, meanwhile, allows interchain charge transfer as a result of enhanced electronic coupling due to overlap of π orbitals between neighboring chains. Charge transport along the alkyl stacking direction, however, is impeded due to the presence of insulating side chains.[62] A high molecular weight plays an important role in the formation of continuous pathways for macroscopic charge transport and facilitating connecting regions of higher

crystallinity to each other, i.e. providing a "softening" of grain boundaries between crystallites.[33] High regioregularity is also important in enhancing chain planarity, packing and mobility.[63,64]

Depending on the device configuration and positioning of electrodes, edge-on or face-on orientation of the P3HT chains could be desirable (Figure 1.10). In organic solar cells in which the active later is sandwiched between the two electrodes, vertical charge transport is desired between the electrodes, and thus maximizing the face-on configuration would be most desirable for improved mobility. In OFETs that have a planar geometry, with two electrodes in the same plane separated by a small conducting channel, the in plane charge carrier mobility should be maximized, and therefore an edge-on configuration with the thiophene rings perpendicular to the substrate surface is desired to facilitate charge hopping by π-stacking along the in-plane direction. Recently, a third configuration called "chain-on" has been recently reported to give record high mobilities above 3.1 $cm^2V^{-1}s^{-1}$ (calculated by the SCLC method) for P3HT. This configuration was achieved by vertical chain alignment in the out of plane direction using a mold to form pillared micropatterns, resulting in high mobilities in the out of plane direction, which is promising for devices with vertical geometries such as organic photovoltaics and organic light-emitting diodes.[65]

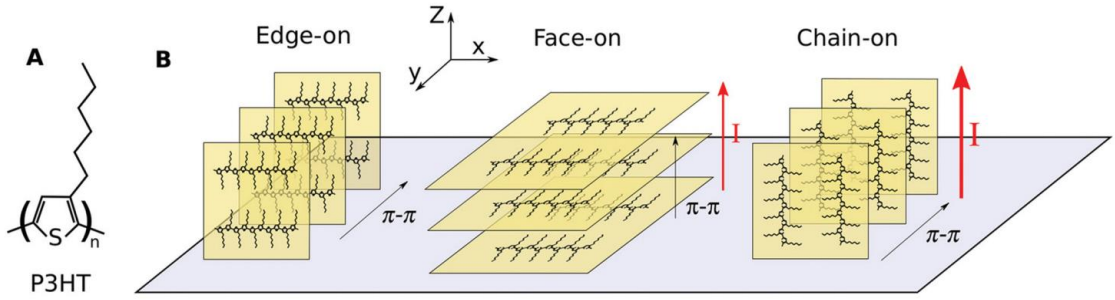

Figure 1.10 P3HT structure (A) as an individual polymer, (B) in 3 different configurations with respect to the substrate: Edge-on, face-on and chain-on. Reproduced from Skrypnychuk et al.[65]

1.3 Organic Field Effect Transistors

Charge carrier mobility can be measured via a number of experimental techniques including time-of-flight,[66,67] pulse-radiolysis time-resolved microwave conductivity (PR-TRMC) (which can measure local mobilities along a chain rather than over macroscopic distances),[68] diode configuration (utilizing space-charge limited current effects, SCLC),[69] and field effect transistors.[35]

Field effect transistors are commonplace in modern computer processors, with metal oxide semiconductor field effect transistors (MOSFET) being particularly popular. Organic field effect transistors (OFET) are the organic material equivalent of the MOSFET and represent not only a means of measuring charge carrier mobility, but can be used in applications such as in the active matrix circuitry of liquid crystal displays, employed as thin film transistors (TFTs).[70] OFETs will be the primary means of characterizing electrical

properties of organic thin films in this thesis and therefore, the operation of these devices will be explained more thoroughly below.

Various materials have been designed that preferentially transport holes or electrons, based on the ease of charge injection from the electrode material. Materials considered "hole transporting" or "p-type" have an ionization potential that closely matches the Fermi level of the electrode material, whereas "electron transporting" or "n-type" materials have an electron affinity closely matching the Fermi level of the electrode material.[35] There also exist organic semiconductors that facilitate ambipolar transport (able to transport both holes and electrons).[71]

Without any external potential, charge transport is diffusive, described by the following equation:[35]

$$\langle x^2 \rangle = nDt \tag{1.4}$$

Where $\langle x^2 \rangle$ is the mean-square displacement of the charges, D is the diffusion coefficient, *t* is time, and *n* is an integer equal to 2, 4, or 6 for one-, two-, and three-dimensional systems, respectively.[35] The charge carrier mobility, μ, is the key quantity that characterizes charge transport, and is related to the diffusion coefficient via the Einstein-Smoluchowski equation:

$$\mu = \frac{eD}{k_B T} \tag{1.5}$$

where k_B is the Boltzmann constant and e is the charge of an electron. Applying an external field induces a drift of the charge carriers which move at a certain velocity and therefore the mobility can be defined as:[35]

$$\mu = v/F \tag{1.6}$$

where v is the velocity of the charges and F is the amplitude of the applied electric field. With units of cm/s for velocity and V/cm for the electric field, the units of mobility are therefore commonly written as $cm^2V^{-1}s^{-1}$.

In order to maximize charge carrier mobility, after injection the charges must travel as efficiently as possible through the semiconducting film to be collected at the opposite electrode. As illustrated in Figure 1.11, an OFET is a three-terminal device, with a source and drain electrode along with a gate electrode that modulates the activity (usually a metal or a heavily doped silicon semiconductor).[72] The dielectric layer is an insulator that can polarize under the action of an electric field. The organic semiconductor transports the charge between the source and drain electrode while the source and drain electrodes have a voltage applied across them to move charges. Based on the needs of the device, different OFET geometries are possible, including bottom gate top contact, bottom gate bottom contact, and top gate bottom contact. Bottom gate bottom contact OFETs are used throughout the experiments in this thesis. The channel length, L, is the distance between electrodes, and is 50 microns in the experiments in this thesis.

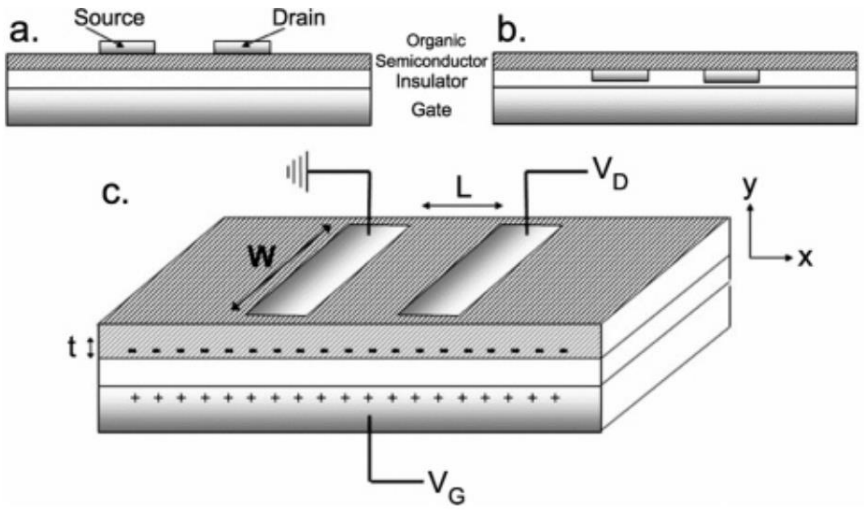

Figure 1.11 OFET geometries (a) bottom gate, top contact, (b) bottom gate, bottom contact. L is channel length and W is channel width. Reprinted with permission from reference.[72] Copyright 2004 American Chemical Society.

1.3.1 OFET Operation

If a positive voltage is applied to the gate, the electric field created will cause a slight displacement of the ions within the dielectric, leading to a microscopic polarization and negative pole on one side of the dielectric and a positive pole on the side touching the organic semiconductor (Figure 1.11c). A negative charge therefore accumulates in the organic semiconductor at the interface with the dielectric in a very thin region, amounting to just a few nanometers.[72] Therefore, the ease of charge transport in the organic semiconducting material directly at the interface with the dielectric is what will most influence the measured mobility, and not the transport that occurs through the bulk of the material. Thus, the morphology and packing of the organic semiconductor at the interface is a highly important determinant of mobility in OFETs.

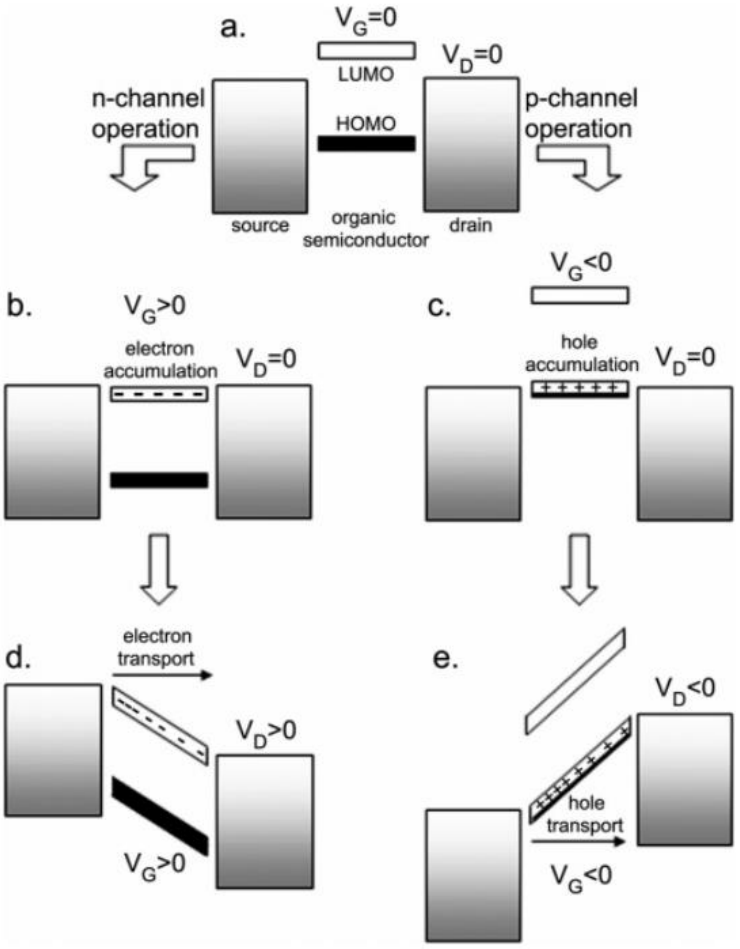

Figure 1.12 Operation of an OFET, in the case of both positive and negative gate voltages applied. Reprinted with permission from reference.[72] Copyright 2004 American Chemical Society.

Figure 1.12 is a schematic of OFETs operation for either p-type or n-type materials. The work function of the metal source and drain electrodes lies within the bandgap of the organic semiconductor.[72] Figure 1.12d shows the case of a positive gate voltage being applied. As the gate voltage is turned on, the organic semiconductor feels the positive pole of the electric field, which will stabilize the electronic levels of the organic semiconductor (shifting its HOMO and LUMO levels down). At some voltage the LUMO level matches the Fermi level of the source and drain and electrodes and electrons flow into the LUMO

levels of the organic molecules. Now that electrons have accumulated into the channel, when the voltage between source and drain is switched on, those charges move from the source to the drain electrode. This is n-type charge transport. On the other hand, if a negative voltage is applied to the gate, the organic semiconductors will feel the negative pole of the dielectric, destabilizing the electronic levels of the organic molecules; when the HOMO level matches the Fermi level of the source and drain, holes will accumulate in the channel. Upon applying the source-drain voltage, holes begin moving across the channel, resulting in p-type charge transport which is the scheme of operation of P3HT-based OFETs in this thesis.

Parameters cited in indicating performance of an OFET include more than just the charge carrier mobility. The on/off ratio is the ratio of the current when a voltage is applied to when the voltage is switched off. Also, the threshold voltage, V_T is a measure of how large of a gate voltage is required for the charges to begin to move in the channel (keeping V_T to a few volts is desired in order to minimize power consumption).

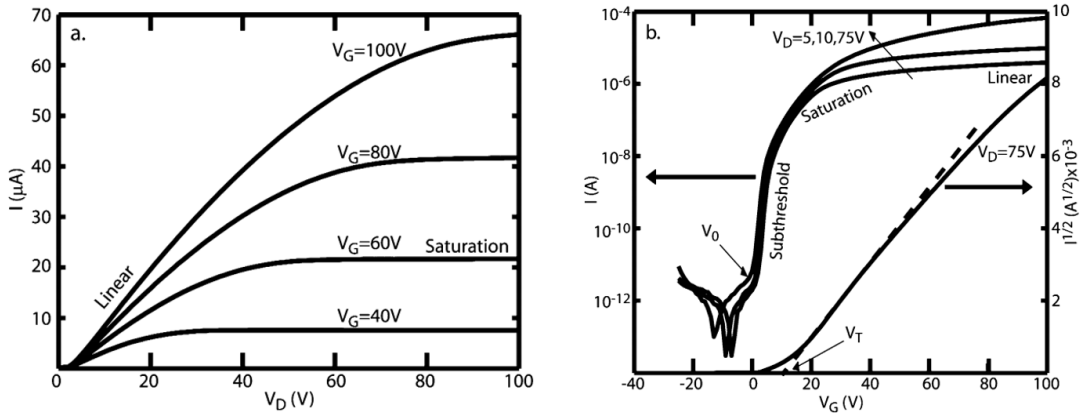

Figure 1.13 Typical OFET results reported in literature: (a) Output curves and (b) transfer curves. Reprinted with permission from reference.[72] Copyright 2004 American Chemical Society.

Two types of plots to show OFET results are typically shown in the literature. Figure 1.13a is the output curve and Figure 1.13b is the transfer curve.[72] In the output curve, as a function of the source-drain voltage, the current (I) that flows between source and drain is plotted on a linear scale. A saturation of this current occurs, which takes place at increasing source-drain voltages when the gate voltage (V_G) is increased. This can be explained by the following: With a fixed, small gate voltage, a small number of charge carriers accumulate in the channel, and as the drain voltage increases, at some point, any charge accumulating in the channel will be immediately extracted - increasing the drain voltage at this point does not lead to any increase in current. But as the gate voltage is increased, allowing more charges to accumulate in the channel, it requires a larger drain voltage to remove all of those charges before saturation in current occurs.

The transfer curves give the source-drain current as a function of V_G. One might expect the current to be zero at a V_G of zero, due to no accumulation of charges in the channel. But as seen in the curves, the current only drops to negligible values at a V_G that is non-zero. With a perfect organic semiconductor with no defects and an appropriate bandgap, a threshold voltage (V_T) of zero is possible. But if defects are present, a gate voltage must be applied to remove the charges that are present in the semiconductor originally. For instance, if a negative gate voltage is required get to zero drain current, holes are being infused into the channel to compensate for the excess electrons that were trapped in the film to begin with. The saturation of these transfer curves can also be explained as follows: At low gate voltages with respect to the source-drain voltage, few charges have accumulated in the channel. With increased gate voltages, the number of carriers in the channel increases, so the current will increase. But if there are so many carriers in the

channel that the drain voltage can no longer deplete them as fast as they accumulate, the current becomes saturated.

As seen on the right hand side of Figure 1.13b, the square root of the source-drain current vs the gate voltage is often plotted to extract the mobility and threshold voltage from the linear or the saturation regime. One can plot the square root of the drain current (ID) vs gate voltage (V_G) and obtain the slope to extract the mobility according to the following equation for the saturation regime, with the following parameters used in this thesis:[72]

$$I_D = \mu C_o \frac{W}{2L}(V_G - V_T)^2 \quad (1.7)$$

where W (2000 μm) and L (50 μm) are the transistor channel width and length, respectively, V_T is the threshold voltage, and C_o is the capacitance per unit are of the SiO_2 gate dielectric (1.15×10^{-8} F cm^{-2}).

1.4 P3HT

Because of its commercial availability, its relatively high mobility (being the first semiconducting polymer to show mobilities over 0.1 $cm^2V^{-1}s^{-1}$), its environmental stability, and ease of processing, P3HT has been studied more than any other material as a model polymeric semiconductor.[73,74] Regioregular P3HT is known to form long fibrillar structures composed of π-stacked P3HT chains, with the stacking direction along the long axis of the fiber (Figure 1.9). These fibers are well defined, with regular thicknesses generally between 10-30 nm.[75]

Intramolecular charge transport as a result of delocalization along a conjugated polymer backbone is generally much faster than the transport that occurs through hopping of charges between molecules (intermolecular charge transport).[35,42,61] Terahertz spectroscopy experiments have shown that very high mobilities (30-40 $cm^2V^{-1}s^{-1}$) in P3HT are possible along the chain backbone.[76] Theoretical predictions of the upper limits of P3HT mobility have been recently calculated to be 50-100 $cm^2V^{-1}s^{-1}$ at room temperature for a perfectly defect-free system.[61] However, in practice the mobility quickly drops over large distances for practical macro-electronics applications (electrodes separated by tens of microns) due to charges having to hop from one chain or crystalline domain to another, and the presence of structural disorder and poor interconnectivity.[33] Average experimental mobilities obtained from OFET devices in the in-plane direction range from 10^{-3} to about 0.2 $cm^2V^{-1}s^{-1}$ for P3HT.[59,77] This lower mobility in practice is due to the defects present in P3HT thin films. Careful control of semiconducting polymer morphology therefore presents a significant opportunity for enhancing electronic performance. P3HT morphology can be manipulated through a number of process methodologies including pre- and post-deposition approaches such as using combinations of good and poor solvents and varying boiling points,[58] ultrasonication,[59] aging,[60] and UV-irradiation[78] of solutions, use of alternate deposition methods such as dip coating,[79] using microfluidic channels,[80] thermal annealing of films,[81] and using P3HT of varying regioregularity.[82]

1.5 Motivation and Outline of Thesis

While efforts to synthesize novel polymers with high mobilities have yielded much fruit, the importance of morphological control on both the micro (nanometers through micrometers) and macro (millimeters) scale represents an important area of

investigation. Developing methods for fine-tuning desirable semiconducting polymer morphologies and understanding the structure-property relationships that govern charge transport are critical in the quest for high performance, reproducible organic electronic devices. Using P3HT as a model semiconducting polymer, this thesis explores, through careful consideration of both solution processing techniques and film deposition techniques, how desired nanostructures as well as macroscale alignment of P3HT can be achieved, and ultimately how these morphologies impact charge transport.

In Chapter 2, the conditions leading to lyotropic liquid crystalline P3HT solutions are explored, and the time-dependent self-assembly of P3HT into nanofibers proves to be essential in facilitating long range ordering in the fluid state. In Chapter 3, these conditions are elucidated further through additional solution processing techniques of ultrasonication and aging, giving insight into the relationship between nanofiber length and long range ordering in the fluid state, and how that ordering is preserved in the film state. Additionally, analysis of the films in Chapter 3 give insight into how various *micro*structures affect charge carrier mobility in OFETs. In Chapter 4, *macro*scale ordering in the film state is carefully controlled through a unidirectional blade coating deposition technique which allowed for understanding how P3HT nanofiber alignment on a *macro*-scale can have a dramatic, and somewhat surprising effect on electronic performance. Chapter 5 summarizes the main conclusions and provides recommendations for future studies.

CHAPTER 2. LONG RANGE ORDER IN P3HT SOLUTIONS: ROLE OF TIME-DEPENDENT SELF-ASSEMBLY

2.1 Introduction

As discussed in the thesis introduction, organic materials including conjugated polymers have attracted significant attention due to their potential use as solution-processable, cost-effective, large area, lightweight and flexible semiconductors for organic electronic devices, including organic photovoltaics (OPV), light-emitting diodes (OLED) and organic field-effect transistors (OFET).[2,3,83–85] Much progress has been made in the design and synthesis of semiconducting polymers that exhibit high charge carrier mobility.[86,87] For instance, mobilities of over 20 $cm^2/V^{-1}s^{-1}$ have been reported for high molecular weight, solution-processed donor-acceptor copolymers.[88] However, chemical structure is only one of the parameters that influence charge-carrier mobility. Intermolecular packing and long-range ordering is equally, if not more, significant.[89–91] Through studies using poly(3-hexylthiophene) (P3HT) as a model system, ordered thin-film morphologies were found advantageous for charge transport.[92,93]

A strategy that uses both molecular structure and process protocols to achieve long-range ordering relies on incorporation of liquid crystalline (LC) functionality.[89,94] Thermotropic (temperature dependent) LC systems with promising self-organizing properties have been employed in organic electronic devices including OPVs and OFETs.[95–97] Lyotropic LC (LLC) systems, which exist in the presence of solvent and

depend on both temperature and concentration, are also attractive because in such systems, long-range order can be preserved into the solid state under appropriate conditions.[98–102] Applied to a semiconducting π-conjugated polymer, solid-state ordering and charge-carrier mobility could be enhanced, and studies pertaining to LLC conjugated polymer systems have begun to appear.[100,101,103] In one study, it was demonstrated that a LLC phase forms at the edge of an evaporating P3HT/1,2,4-trichlorobenzene (TCB) droplet.[103] More recently, Kim, et al. reported that a complex thiophene-based polymer forms a LLC, which exhibits a three order of magnitude increase in mobility along the alignment direction compared to that for the perpendicular direction.[100] Additionally, poly(3-butylthiophene)/o-chlorobenzene solutions display anisotropic charge transport through aligned films formed by a capillary-based "direct-write" technique.[101] However, to realize the full potential of lyotropic liquid crystallinity for electronic materials based upon π-conjugated polymers, fundamental insight into semiconducting polymer solution phase behavior is required.

Here, using P3HT as a model, conditions leading to room-temperature lyotropic liquid crystalline polymer solutions are demonstrated, and a mechanism for the formation of the ordered fluid is postulated. Polarized optical microscopy (POM), UV-Vis absorption spectroscopy, micro-Raman spectroscopy, depolarized dynamic light scattering (DDLS) and cryogenic transmission electron microscopy (cryo-TEM) were used to characterize the time evolution of intermolecular ordering and orientation. The time-dependent propensity of P3HT to self-assemble and form liquid crystalline solutions was demonstrated. The results have implications related to ordering phenomena displayed by π-conjugated

polymers, solidified polymer thin-film charge-carrier mobilities and the design of robust semiconducting polymer materials and processes for device applications.

2.2 Results and Discussion

2.2.1 Polarized Optical Microscopy

The observation that P3HT forms a LLC phase during solvent evaporation[103] led to initial experiments focused on the impact of polymer solution concentration. To determine the range of concentrations that result in a LLC phase in P3HT in TCB, solutions with varying concentrations of P3HT (Rieke, 96% H-T, M_w = 71 kDa, PDI = 2.2) were prepared by heating the polymer/solvent mixture at 80°C for approximately 30 min. Rectangular capillaries (1mm x 0.1mm x 50mm) were filled with these viscous fluids 20 min after the solution had been cooled to room temperature and were then sealed with epoxy to inhibit solvent evaporation. As seen in Figure 2.1, at solution concentrations of 4.5 wt% (w/w), P3HT appeared dark (isotropic) when interrogated using POM while those at 6.6 wt% P3HT were birefringent. Above 8 wt% P3HT, the polymer did not fully dissolve. Capillaries filled with 80°C or room temperature bright orange solutions appeared isotropic (dark). The transmitted light intensity is highest when the 6.6 wt% sample is at 45° with respect to the crossed polarizers, while it is nearly fully extinguished at 90°. This behavior can be explained using equation 8:[104]

$$I = I_o[\frac{1}{2}(1 - \cos 4\phi)\, sin^2\left(\frac{\pi\delta}{\lambda}\right)] \quad (8)$$

where I is the transmitted intensity through the crossed polarizers, I_o is the incident intensity, ϕ is the angle that the optic axis of the anisotropic material makes with the polarizer, δ is the light path difference caused by the difference in refractive indices along two directions in the material and λ is the wavelength. While some defects are apparent, the almost uniform switching of bright to dark with sample rotation is indicative of near monodomain character, suggesting long-range order within the sample.

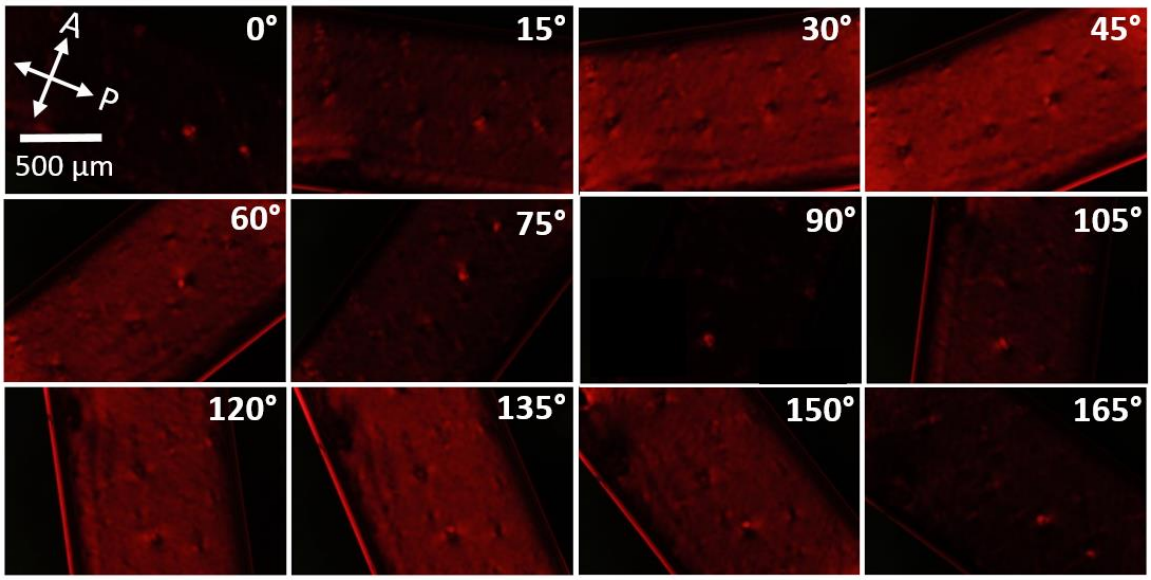

Figure 2.1 Capillary of 100 mg/mL P3HT (6.6wt%) in TCB, filled after aging 20 min. at room temperature, viewed between crossed polarizers. From left to right, sample is rotated counter-clockwise in increments of 15° with respect to the polarizer.

At a concentration of 100 mg/mL (6.6 wt%), P3HT/trichlorobenzene (TCB) solutions afforded birefringent fluids in capillaries filled only after the stock solution stood for at least 20 minutes at room temperature before filling. (Figure 2.1). The time-dependent phenomenon suggests that dynamic changes occur within conjugated polymer solutions that are otherwise maintained in a static environment. Since such changes will markedly

impact solution-based π-conjugated polymer device fabrication processes, the time-dependence of dilute P3HT solution behavior was investigated.

2.2.2 UV-Vis Results: Time-Dependent Self-Assembly Detected

P3HT solutions were prepared in TCB at a concentration typically used for organic field-effect transistor (OFET) device fabrication (5mg/mL P3HT/TCB). As shown in Figure 2.2, no distinct UV-vis spectral features were observed immediately after preparation (day 0). However, within one day, the solution began to darken and the 0-0 vibrational peak at 2.07 eV (599 nm), began to develop. Over the course of 60 days, the 2.07 eV band intensity increased and the solution became purple. The intensity increase suggests enhanced P3HT π-π interactions in solution, which most likely emanate from P3HT chain self-assembly into aggregated structures.[105] The percentage of polymer chains assembled into aggregates in solution as a function of time (Figure 2.2b**)** were estimated from Franck-Condon fits to the absorption spectra (Figure A - 2) using the approach reported by Pingel et al for weakly interacting H-aggregates of P3HT.[106,107] A Franck-Condon progression (Equation A1) is used to generate the theoretical vibrational peaks, which are subtracted from the experimental curve to give the amorphous fraction and aggregate fraction. The proportion of P3HT that had aggregated increased approximately linearly through day 24 of aging, after which the rate of aggregation began to level off. This evolution of aggregation is consistent with the model of homogenous nucleated growth of nanofibers driven by π-π stacking.[108,109]

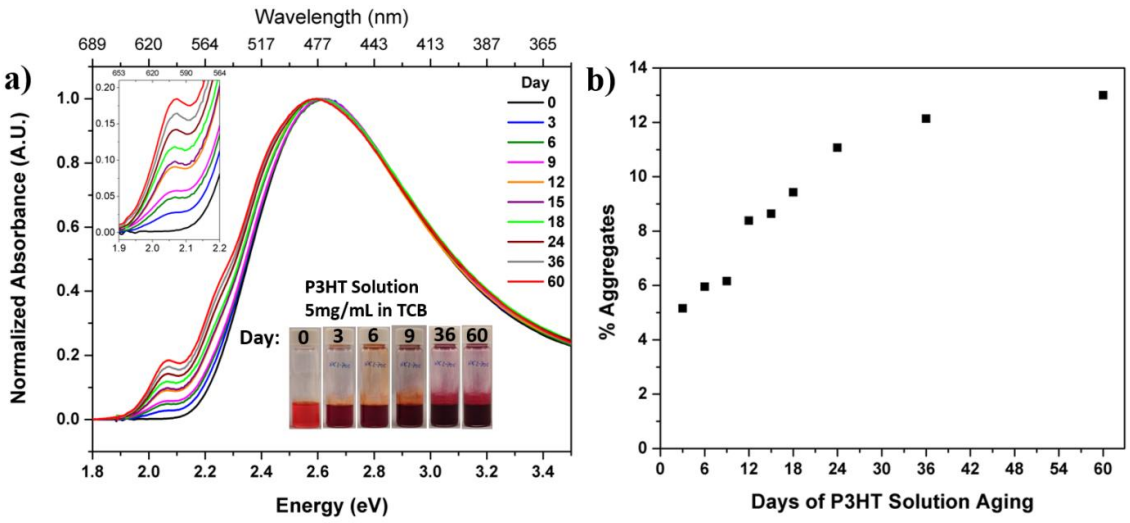

Figure 2.2 (a) Solution UV-Vis spectra of 5 mg/mL P3HT/TCB as a function of time. (b) Percent aggregates calculated from the UV-Vis spectra using Franck-Condon fits as described by Pingel et al.[106,107]

2.2.3 Long Range Order Observed Over Time with POM

As evidenced by POM (Figure 2.3a), a capillary filled with freshly prepared (day 0) P3HT/TCB solution appeared isotropic. However, capillaries filled with solutions that had remained in the vial for 2 or more days prior to filling appeared birefringent; when viewed through crossed polarizers on the same day they were filled, these capillaries appeared increasingly bright up to day 36 (Figure 2.3a). The almost complete extinction and re-emergence of brightness upon rotation of the capillary long axis from 0° to 45° with respect to the polarizer indicates a near monodomain, with requisite alignment. Figure 2.3b depicts the linear dichroism associated with capillaries filled with aged P3HT solutions; dichroism was not evident in as prepared, fresh samples. The observed dichroism is believed to emanate from P3HT that has π-stacked into elongated assemblies preferentially oriented parallel to the capillary long axis as depicted in Figure 2.3c**.** The π-stacking

direction depicted is supported by cryo-TEM analysis of P3HT/o-dichlorobenzene carried out by Wirix et al.[110]

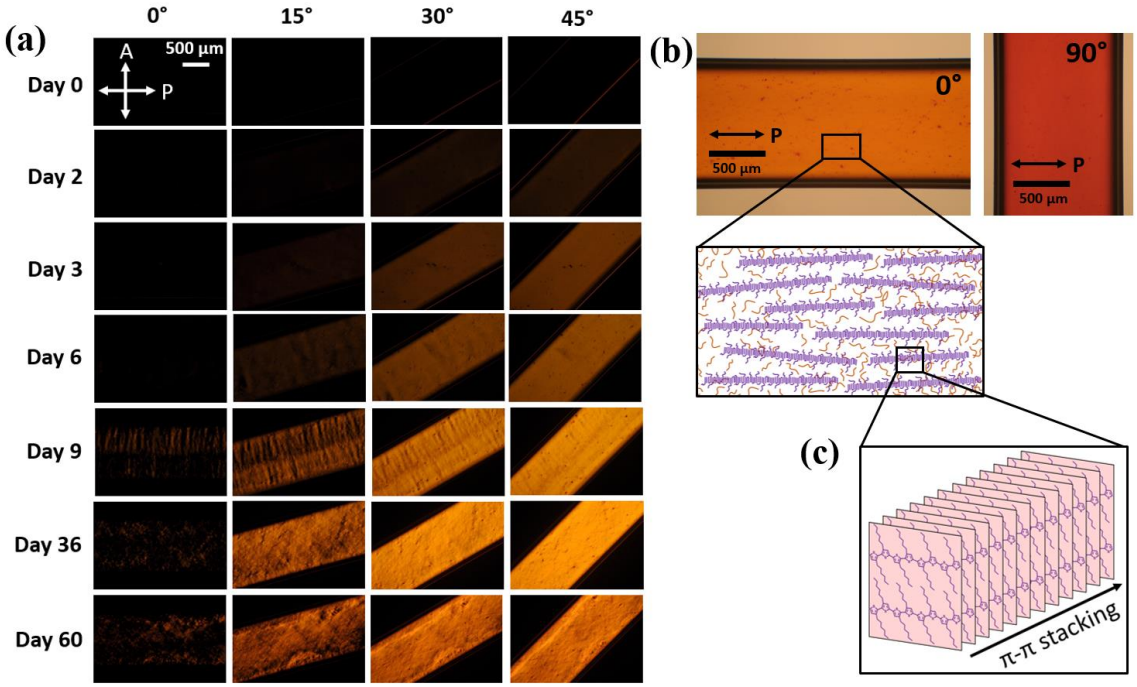

Figure 2.3 (a) POM micrographs of 5 mg/mL P3HT/TCB solutions filled into capillaries after varying aging times of the stock solution in the vial, rotated in increments of 15° between crossed polarizers. (b) Change in absorption as a function of capillary orientation with respect to polarizer; image shown is capillary filled on day 36, displaying linear dichroism. (c) Representation of P3HT nanofibers (purple) oriented within the capillary with expected π-π stacking direction along the long axis of the nanofiber (orange lines in upper cartoon represent individual P3HT chains). Note: Cartoons in figures 2b and 2c are not drawn to scale.

Birefringent capillary samples remained so even 18 days after filling (Figure A - 3), while capillaries filled with fresh (day 0) solution appeared isotropic both upon filling and 18 days later. When heated to 80°C followed by controlled cooling at 10°C per 30 min to room temperature, the birefringent samples underwent a color change from purple to orange, became isotropic, and remained so for at least 21 days at room temperature. The

origin of the observed differences in P3HT self-assembly between solutions kept in vials vs. capillaries were not investigated as part of this study.

2.2.4 Polarized Micro-Raman Spectroscopy – Quantifying Orientational Ordering

Polarized micro-Raman spectroscopy was used to further characterize the degree of orientation of the P3HT solutions as a function of aging time. The Raman spectra as a function of angle θ between the long-axis of the capillary and the polarization of incident light are shown in Figure 2.4. The bands at approximately 1450 cm^{-1} and 1380 cm^{-1} are attributed to P3HT thiophene ring C=C and C-C stretching vibrations, respectively.[111] The Raman intensity and fluorescence background of isotropic solutions do not change with rotation of the sample (Figure 2.4a). However, as seen in Figure 2.4b, the Raman signal intensity associated with birefringent P3HT/TCB 36-day aged solutions exhibited angular dependence, indicating anisotropic P3HT chain ordering. The strongest signal was detected when the capillary long axis was at 90° with respect to incident laser polarization; conversely, the weakest signal was apparent when the capillary long axis was held parallel. This angular dependence suggests the P3HT chains are oriented perpendicular to the capillary long axis (suggesting P3HT fibers are oriented along capillary long axis), supporting the conclusions drawn from the dichroism results (Figure 2.3b,c).

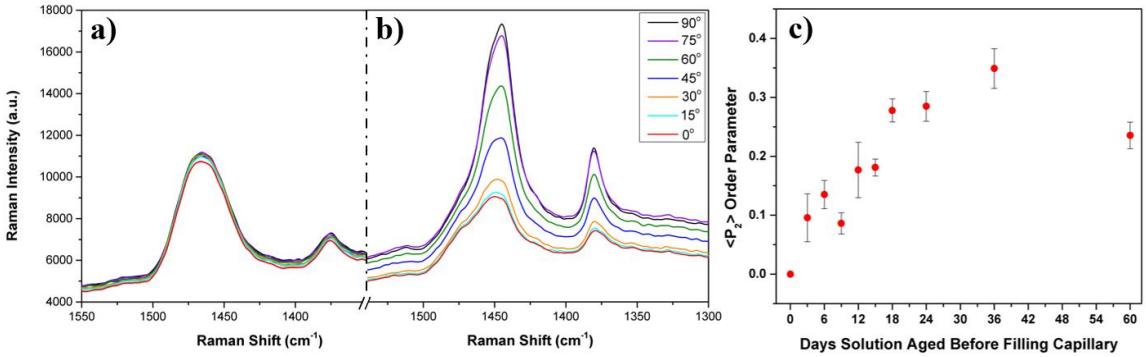

Figure 2.4 Polarized Raman spectra of capillaries filled with P3HT/TCB solutions (5 mg/mL) aged in a vial for (a) ~30 min and (b) 36 days after the solution was made before filling the capillary. Energy range displayed focuses on peaks arising from the C=C and C-C stretch in the thiophene ring of P3HT. Angle refers to rotation of the sample with respect to the plane of polarization. All spectra were taken with parallel polarizers. (c) $<P_2>$ orientational order parameter as a function of solution aging time before filling capillary.

Upon aging, the P3HT C=C stretching mode vibrational frequency decreased from 1467 cm^{-1} to ~1452cm^{-1} for freshly prepared and aged solutions, respectively (Figure 2.4a and Figure 2.4b). The peak position remained relatively constant for samples aged from 3 to 60 days. The frequency shift strongly suggests the extension of conjugation over time. A similar decrease in C=C stretching frequencies was observed in evaporating droplets of P3HT in TCB, corresponding with anisotropy in the polarization intensities of Raman scattering at high concentrations.[103] An increased level of intermolecular interactions between π-conjugated units is expected to lead to increased π-π overlap.[112] As neighboring chains begin to order into closely packed structures, the strong interactions cause a damping effect that reduces oscillations, causing the shift.[113,114]

In addition to qualitative insight, micro-Raman analysis provides quantitative information regarding the degree of P3HT orientation. The orientational order parameters, $<P_2>$ and $<P_4>$, were obtained for P3HT/TCB fluids as a function of aging time (Figure

2.4c). A completely isotropic material will have a $<P_2>$ orientational order parameter of 0, while a value of 1 is expected for a perfectly ordered crystal. With the second rank, $<P_2>$, and fourth rank, $<P_4>$, parameters, the orientational distribution function can be estimated.[115] The Raman C=C stretching peak height (using Lorentzian function fitting from 1510 cm^{-1} to 1400 cm^{-1}) was obtained at angles from 0 to 360° in increments of 10° in both parallel and crossed polarizer geometries. The ratio of the peak heights arising from perpendicular vs. parallel polarizers (depolarization ratio, $R(\theta)$) as a function of the rotation angle θ, was fit to the following function containing the two order parameters assuming a uniaxial nematic (Eq. 9);[116]

$$R(\theta) = \frac{I_{\perp}(\theta)}{I_{\parallel}(\theta)} = \frac{(-1+r)^2[56 + 40\langle P_2\rangle + (9 - 105cos4\theta)\langle P_4\rangle]}{[56(8r^2+4r+3) - 40(4r^2 - r - 3)(1 + 3cos2\theta)\langle P_2\rangle + 3(r-1)^2(9 + 20cos2\theta + 35cos4\theta)\langle P_4\rangle]} \quad (9)$$

where r is the ratio of differential polarizabilities. An example of a fit is shown in Figure A - 5. This quantification of the order parameter as a statistical average of molecular orientation further clarifies the development of a liquid crystalline P3HT solution upon aging. On day 0, both $<P_2>$ and $<P_4>$ had values of 0, which increased to 0.35 and 0.27, respectively, on day 36. Error bars in Figure 2.4c arise from the R^2 values obtained using the depolarization ratio fitting function to obtain the order parameters (Figure A - 5b). The time dependent order parameter increase suggests enhanced alignment as P3HT self-assembles.[117] Typically, $<P_2>$ ranges from 0.35 – 0.7 for the nematic phase of conventional low molecular weight thermotropic LC systems.[118–120] Due to the time-dependent aggregation behavior of the P3HT/TCB solution, it is difficult to compare the values of order parameters obtained here with those of more well-known systems. However, the

increase in order parameter with time is clear, which may give insight into optimal π-conjugated polymer solution preparation conditions for organic electronic device applications. By day 60, the $\langle P_2 \rangle$ and $\langle P_4 \rangle$ order parameters dropped to 0.24 and 0.12, respectively. The significance of this decrease is unclear, and investigation of its origin is beyond the scope of the present study.

2.2.5 Depolarized Dynamic Light Scattering – Anisotropic Entities Detected

P3HT self-assembly in solution was further investigated by DDLS, which measures the depolarization of incident light scattered by anisotropic entities suspended in a liquid.[121] The time dependence of the light scattering intensity was recorded using two geometries: Vv (detector vertical, incident light vertical) and Hv (detector horizontal, incident light vertical). Figure 2.5a displays the depolarization ratio, ρ_v, (Eq. 10) recorded over days 0-3 of aging.

$$\rho_v = \frac{I_{Hv}}{I_{Vv}} \tag{10}$$

In this expression, the subscript v refers to incident light polarized in the vertical direction, I_{Hv} and I_{Vv} are the intensities of the horizontal and vertical polarizations of scattered light, respectively. For DDLS details, see Appendix.

The ρ_v ratio is related to excess Rayleigh scattering,[122,123] which is due to optical anisotropy of entities.[123] For an isotropic scattering object, ρ_v should be zero.[124] When well dispersed in solution, polymer molecules, either random coils or rods, usually depolarize only weakly. However, the signal is expected to increase when the chains become

semiflexible or rigid. Changes in chain conformation, aggregation and the formation of ordered states are known to increase the overall optical anisotropy and thus depolarization of incident light.[125–128]

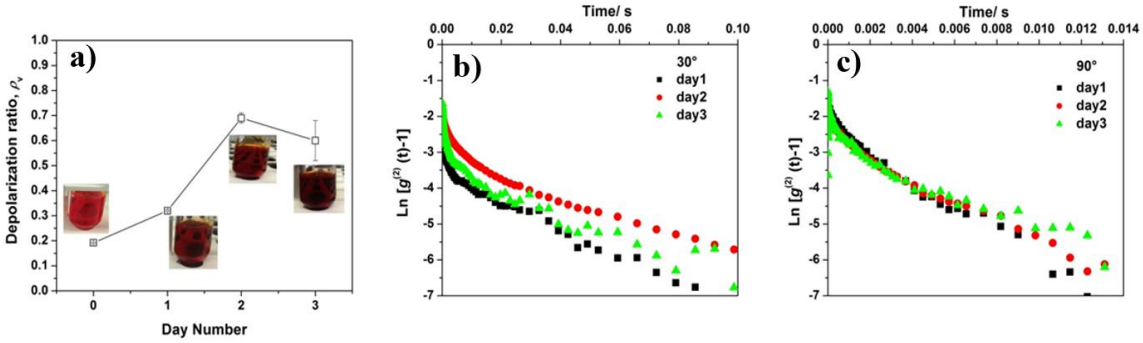

Figure 2.5 (a) Depolarization ratio ρ_v as a function of aging time. Each data point is an extrapolation to the scattering vector magnitude q = 0 over three scattering angles (30°, 45° and 90°). The depolarization ratio at each angle is an average of five measurements; pictures showing the appearance of the P3HT/TCB solution at the time of the measurement appear near the corresponding data points. Typical intensity autocorrelation function (V_v) in semilogarithmic form recorded from day 1 to day 3 at θ = 30° (b) and 90° (c).

Freshly prepared (day 0) P3HT/TCB showed a weak depolarization signal. After 2 days, ρ_v increased to a net value of 0.65, which was essentially maintained into day 3. This value is significantly higher than that reported by Yamamoto et al. for bipyridil-based conjugates (0.33)[129] and exceeds the theoretical limiting value of 1/3. This theoretical limit was evaluated for a rodlike molecule with a high polarizability along the rod axis when compared to the polarizability along other directions.[130–132] The large degree of depolarization was related to the ability of bipyridil complexes to form rod-like rigid structures in which the polymer chains stack due to π-π conjugation. Within the self-assembled supramolecular construct, electrons are highly mobile along the polymer chain.

The ρ_v value obtained for P3HT/TCB suggests that P3HT chains self-assembled into rigid elongated structures. The high depolarization signals recorded for the system are consistent with the observations of Yue, Berry and McCullough[133] for poly(3-dodecylthiophene) in chloroform. For the dodecyl polymer, the strong depolarized scattering was attributed to supramolecular self-assembled needlelike structures and also to disk-like aggregates. However, caution is required when interpreting the results because absorption, fluorescence and multiple scattering events all influence the measurements, as they do in some metallic systems.[134–136] A more detailed investigation is required to elucidate the time-dependent dynamic processes P3HT undergoes in solution.

While a P3HT/TCB solution with a low concentration (5 mg/mL) was used, the self-assembled structures have a higher local concentration than the surrounding medium. This concentration profile could be sufficient to induce a phase transition to an ordered phase.[133,137] The formation of ordered states is supported by POM data (Figure 2.3**)** demonstrating the emergence of birefringence over time. Past day 3, sample turbidity increased and reliable depolarization measurements (see inset pictures in Figure 2.5a) were prohibited.

Figure 2.5b and Figure 2.5c display the intensity autocorrelation function, as a function of time, of bulk P3HT/TCB solutions at two angles. At a 30° scattering angle, where the contribution of large objects to the scattering signal is higher, all correlograms exhibited multiexponential behavior. This behavior is expected in the presence of elongated rigid structures that nucleate and grow in the bulk solution at different rates. The increase in the decay rate of the slow mode from day 1 to day 3, coupled with an enhanced DDLS response, indicates an increase in sample anisotropy due to the formation of rigid

structures with extended ordered phases. The 90° angle results enable a closer look inside the landscape of the small structures. The correlograms revealed that, regardless of aging time, small structures of similar dimensions are present in the solution at all times, and because the correlation function traces overlap, exhibit similar behavior (Figure 2.5c). This aspect can be assigned to the entity rotation which has a significant contribution at the 90 degree scattering angle. At some point, the scattering objects evolve slightly differently, which may coincide with initial P3HT aggregate formation and the transition to ordered domains through π-π conjugation.

2.2.6 Cryo-TEM

Cryo-TEM provides additional insight into P3HT solution-state structure.[110,138] Figure 2.6 shows cryo-TEM images of freshly prepared and aged P3HT solution samples. Whereas the freshly prepared solution appears amorphous, nanofibrillar structures are observed in the aged solution, supporting the POM, micro-Raman spectroscopy, and light scattering results.

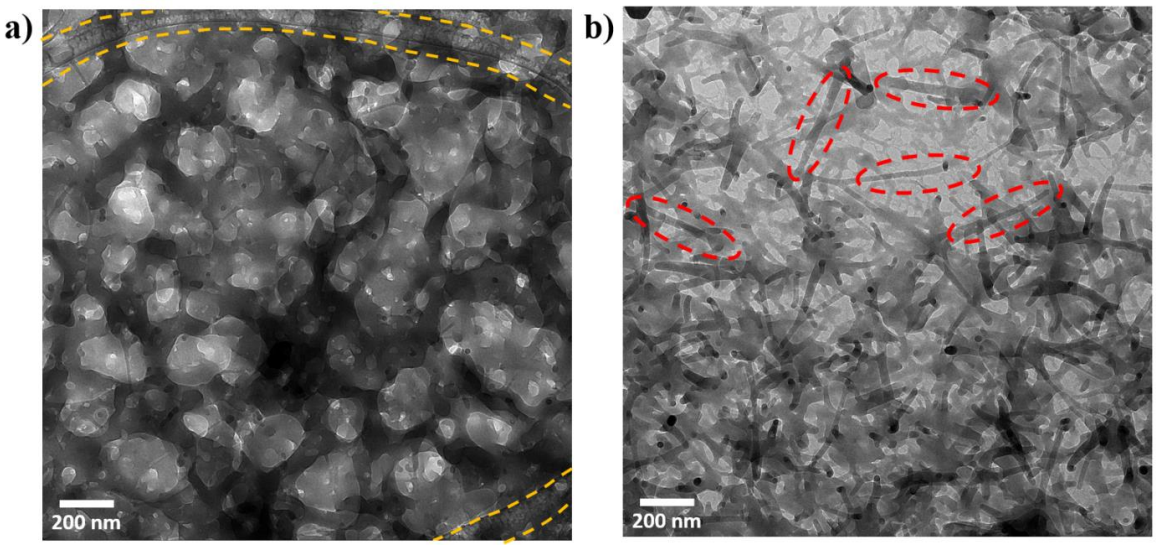

Figure 2.6 Cryo-TEM images of P3HT solutions in TCB (5mg/mL) aged for (a) 0 days and (b) 31 days. White regions are voids. Pale grey represents less dense material. Yellow borders highlight regions where the lacey sample grid can be obseved. Examples of nanofibrils present in (b) are identified by red ovals.

2.2.7 Drawing of Films – Maintaining Orientational Ordering In Solid State

The propensity of conjugated polymers to assemble into ordered structures in the solution state may profoundly impact the application of such materials as active layers for electronic devices. The prospect of retaining solution state ordering during solvent evaporation has particularly attractive possible consequences. When 10 µL micropipette tips were used to "draw" 36-day aged solutions of P3HT onto clean glass substrates, and TCB was allowed to evaporate for approximately 12 hours, the samples appeared birefringent under POM (Figure 2.7b); films drawn from freshly prepared solutions were isotropic (Figure 2.7a). Thus, solution phase, time-dependent conjugated polymer self-assembly facilitates alignment that may be preserved into the solid state through judicious choice of deposition method. Maintenance of ordering in the solid state has promising implications for improving charge transport in devices such as OFETs.

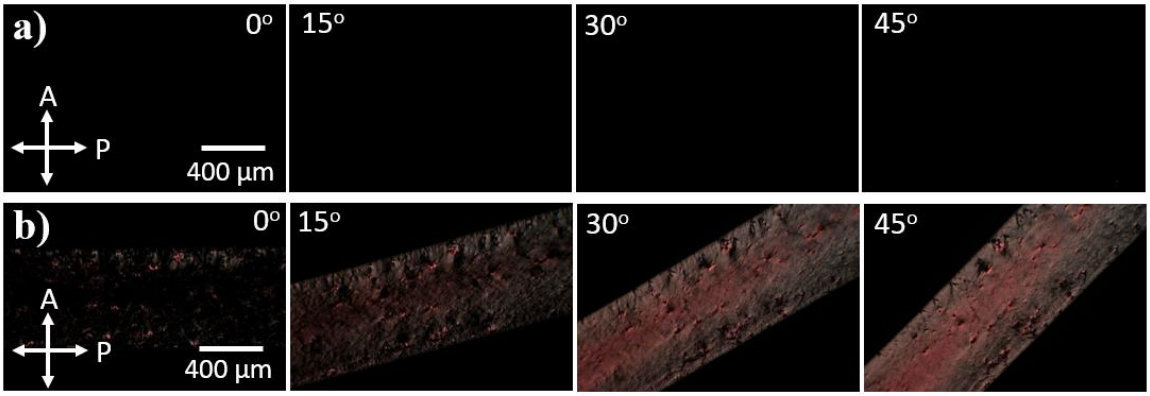

Figure 2.7 Polarized optical microscopy images under crossed polarizers of a film; (a) drawn from freshly prepared 5mg/mL P3HT/TCB solution showing isotropic state, and (b) drawn from 36-day aged 5 mg/mL P3HT/TCB solution showing birefringence and alignment in the solid state. The films were drawn on glass substrates using a 10 µL micropipette tip.

2.3 Conclusions

In TCB solutions, physical P3HT structure was shown to actively and continually change over time. The time-dependent self-assembly process was characterized through a range of spectroscopic and microscopic techniques. The low energy UV-Vis absorption band developed in a progressive manner, indicating an increased percentage of aggregated polymer in solution. Over a 36 day period, the orientational order parameters, $\langle P_2 \rangle$ and $\langle P_4 \rangle$, increased to a maximum of 0.35 and 0.27, respectively. As supported by cryo-TEM analysis, DDLS studies indicate that P3HT forms rigid, anisotropic structures. POM images of solidified, aged P3HT solutions suggest that solution-state ordering can be retained into the solid state upon solvent-evaporation. A visual summary of the main results in Chapter 2 are shown in figure.

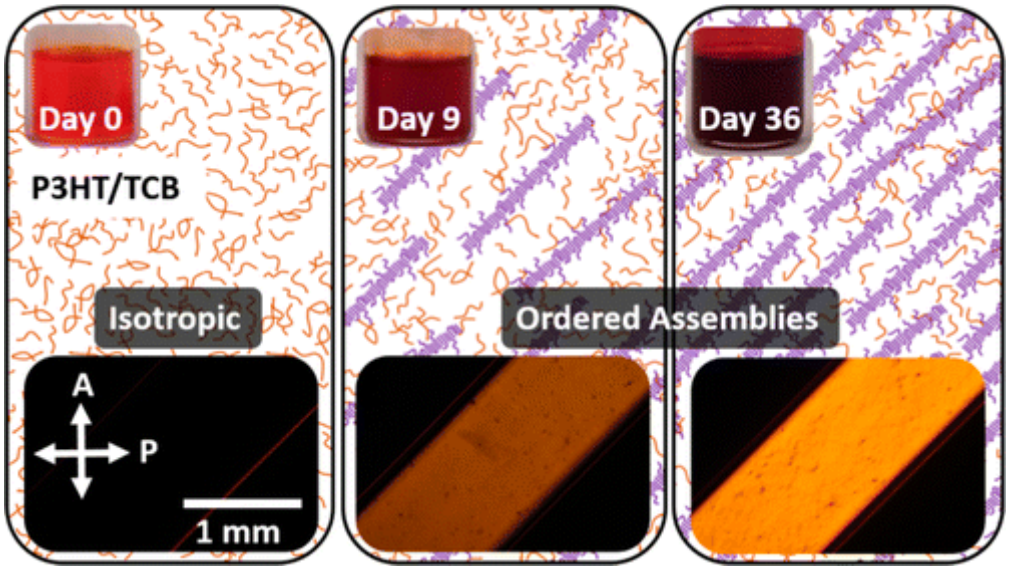

Figure 2.8 Visual summary of some of the main results in Chapter 2.[139]

The results of these investigations impact the design and development of π-conjugated polymer materials and processes for electronic applications. In a process that is unlikely to be unique, dilute P3HT solutions were shown to undergo substantial changes over the course of days to months. Over time, the polymer self-assembles and aggregates into ordered structures. Ordered and oriented conjugated polymer assemblies have many desirable attributes for high performance device applications, where the ability to control nano- through macro-scale molecular ordering is highly sought after. However, the time dependent nature of the phenomenon has potential negative consequences, particularly as pertains to the development of robust materials with requisite shelf-life for large-scale device fabrication. Further fundamental studies related to π-conjugated polymer solution phase behavior are required.

2.4 Experimental Section

Materials: Regioregular P3HT was purchased from Rieke Metals Inc. (Catalog Number RMI-001EE, Regioregularity = 96% HT, M_w = 71 kDa, PDI = 2.2) and used without further purification. 1,2,4-Trichlorobenzene (anhydrous, ≥ 99% purity) was purchased from Sigma Aldrich (Catalog Number 296104-1L) and used without further purification. Borosilicate glass capillaries of 0.1 mm x 1 mm x 50 mm dimensions were purchased from Vitrocom Inc. and used without any further surface treatment.

Preparation and Aging of P3HT Solutions: P3HT was dissolved in TCB at 80 °C with stirring for 30 min or until completely dissolved and then cooled to room temperature at a rate of approximately 20 ºC per hour. Solutions were then filtered using teflon syringe filters of 0.2 µm pore size with a needle on the end, and stored in capped vials in the dark at room temperature as they aged, being removed only for characterization on select days. Capillaries were filled by submerging one end in the solution and allowing the solution to flow up the capillary. After filling capillaries with P3HT solution for POM and Raman characterization, they were immediately sealed with epoxy to inhibit solvent evaporation. While fluctuations in room temperature by day may cause changes in the rate of aggregation, similar trends in data were observed for experiments repeated with multiple solutions on different days.

UV-Vis Spectroscopy: Solution UV-Vis spectra were obtained using an Agilent 8510 UV-Vis spectrometer with a cuvette path length of 0.05 mm.

Polarized Optical Microscopy (POM): POM images were obtained using a Leica DMRX optical microscope equipped with a rotatable polarizer and analyzer and a Nikon D300 digital SLR camera

Raman Micropectroscopy: Raman spectra were obtained using a 50× objective and a 785 nm laser light source (Kaiser Optic System) which has 4 cm^{-1} resolution in the backscattering geometry. For all order parameter measurements of samples except day 3, the laser power was 20 mW and spectra were acquired using exposure times of 6 seconds with 6 accumulations. The day 3 sample required a higher laser power of 40 mW and an exposure time of 8 seconds with 8 accumulations in order to obtain high enough signal-to-noise ratios for accurate peak fitting. The spectra displayed in figure 4a and 4b were obtained using 40 mW laser power and 8 second exposures with 8 accumulations. The polarized component was obtained by setting the analyzer parallel to the polarization direction of the incident beam, while the depolarized geometry was obtained by setting the analyzer perpendicular to the polarizer. The order parameters of P3HT solutions were calculated by recording a series of polarized Raman spectra as a function of angle, θ, between the polarization vectors of incident light and the long axis of the capillary tube. The sample stage was rotated in increments of 10° from 0 to 350° and spectra were obtained for both polarized and depolarized geometries. For each spectrum, the peak corresponding to C=C stretching was fit to a Lorentzian function using Holograms™ software to obtain peak heights and positions. Ratios of peak heights obtained in the depolarized geometry to peak heights obtained in polarized geometry were plotted vs. rotation angle in radians and a depolarized ratio fitting function was used to obtain $\langle P_2 \rangle$ and $\langle P_4 \rangle$ order parameters according to the procedures of Park et al.[46] The power of the incident laser was measured

in both polarized and depolarized geometries in order to avoid overestimation of the depolarization ratio and order parameter due to reduced incident laser power in the depolarized geometry: a correction factor based on this ratio of incident laser powers was applied to peak heights prior to the depolarization ratio and order parameter calculations.

Light Scattering. Multi-angle dynamic light scattering measurements were acquired using a custom-built apparatus equipped with an ALV-5000 autocorrelator and associated software. The instrument has a classical design, two pinholes and lenses for homodyne detection. The small sample volume was illuminated by a focused laser beam (632.8 nm). Measurements were made at six different angles (30° - 120°). The temperature of the toluene bath surrounding the sample cell to suppress reflected light was maintained at 25 °C using a circulating bath. Two Glan-Thomson crystals (Karl Lambrecht) with a mutual extinction of ~10^{-6} were used to ensure the polarization of the laser beam. The incident radiation was always vertical (i.e., perpendicular to the horizontal scattering plane defined by incident and scattered light). The light scattered by the sample was detected in two ways: vertically polarized (Vv) and horizontally polarized (Hv). The sample was prepared as follows: a volume of 2 mL of solvent (1,2,4-trichlorobenzene, TCB) was filtered (Whatman PTFE filter, 0.1 μm pore size) in a dust-free DLS vial (Pyrex, 13 × 100 mm from Fisher) containing a weighed amount of P3HT (Rieke Metal Inc., M = 71 kDa, PDI = 2.2, RR = 96 %) to ensure a 5 mg/mL (w/w) concentration. The vial was tightly capped and heated up to 80 °C using a hot plate. While still hot, the solution was transferred into a Teflon syringe fitted with a 0.45 μm filter (Whatman, PTFE) and filtered (1 mL) into a clean dust-free DLS vial. Then the vial was capped and allowed to cool down at ambient temperature. This sample was measured the same day at 25°C and also on the three following days.

Cryo-TEM. An FEI Mark IV Vitrobot was used to prepare cryo-TEM samples. A drop of 4 microliters of the liquid sample was placed on 200 mesh lacey carbon grid held by tweezers. The grid was lifted into a 100 % humidity chamber and blotted by filter paper from both sides at force level 2 lasting 1.5 seconds and plunged into liquid ethane (-140 °C) to freeze and vitrify followed by storage in a grid box immersed in liquid nitrogen. The grid was transferred in liquid nitrogen to a Gatan cryo-TEM holder through a Gatan cryo-transfer station. The samples were observed with an FEI G2 F30 Tecnai TEM at 200 kV at -170 °C.

For example of Frank-Condon fittings to obtain percent aggregates from UV-Vis absorption spectra, POM of solutions confined to capillaries over time, a description of the DDLS theory employed, and detailed Raman data including a full spectrum, peak heights, and order parameter fittings, see Appendix A.

CHAPTER 3. ORDERING OF P3HT IN SOLUTIONS AND FILMS: EFFECTS OF FIBER LENGTH AND GRAIN BOUNDARIES ON ANISOTROPY AND MOBILITY

3.1 Introduction

In Chapter 2 it was demonstrated that P3HT in TCB undergoes time-dependent self-assembly (aggregation) to afford birefringent fluids with long range order in capillary tubes.[139] The percent of aggregated polymer, as calculated from UV-vis spectroscopic measurements, rose with time, as did the orientational order parameter as determined by polarized micro-Raman spectroscopy. The results suggested a need for a minimum degree of aggregation for the emergence of liquid crystallinity.

Alternatively, P3HT can also be induced to aggregate by a variety of other techniques, including ultrasonication.[59,140,141] Curiously, ultrasonication of solutions alone did not lead to the formation of birefringent fluids, despite high levels of aggregation. In this chapter, the effects of aggregation technique on long range order in solution and the resulting P3HT thin film charge transport characteristics are evaluated for sonicated and aged P3HT/chloroform solutions. UV-vis spectroscopy, polarized optical microscopy (POM), polarized Raman spectroscopy and atomic force microscopy (AFM) analysis indicate that long range ordering in solution and resultant films depends on average self-assembled P3HT fiber length. Compared to long fibrillar structures obtained through aging, ultrasonication induced formation of relatively short fibers. Solutions and films prepared via the two approaches were anisotropic or isotropic, respectively. Significantly, aging of the sonicated solution afforded thin films having superior charge transport characteristics

(0.15 $cm^2V^{-1}s^{-1}$). Grazing incidence wide angle X-ray scattering (GIWAXS), mobility, UV-vis and anisotropy results suggest that in addition to fiber length, grain boundary morphology is an essential factor that determines macroscale charge transport performance.

3.2 Results and Discussion

3.2.1 UV-Vis and Polarized Optical Microscopy

Figure 3.1 presents a schematic representation of the P3HT solution processing techniques used here. P3HT/chloroform solutions (5mg/mL) were prepared at 70 °C, after which the orange solutions were allowed to cool to room temperature. Upon reaching room temperature, solutions were injected into vials. For pure aging (Figure 3.1a), the capped vial was simply left to stand at room temperature in the dark for the desired duration; a change in color from orange to dark brown/purple indicated the self-assembly of P3HT.[139] As shown in Figure 3.1b, a portion of the as prepared solution was first sonicated for two minutes, causing an almost immediate color change to dark brown/purple. The sample was then characterized, and allowed to stand in a capped vial for the desired interval. Figure 3.1c depicts a solution that was first aged for 96 hours, and then sonicated for 2 min. All characterization data for both solutions and films refer to the indicated duration of aging and/or sonication of the *solution* before active layer thin-film deposition by spin coating.

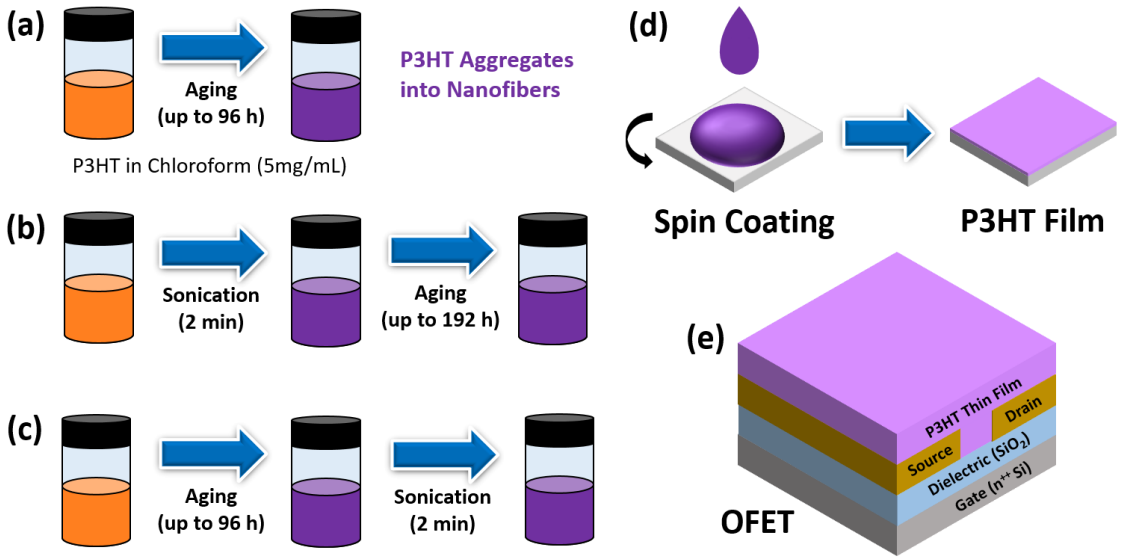

Figure 3.1 Experimental diagram of P3HT solution processing by (a) aging, (b) sonication, and sonication then aging, and (c) aging then sonication. (d) Spin coating to form thin films. (e) Bottom-contact OFET geometry employed for testing electrical properties.

Figure 3.2a presents changes in the UV-vis absorption spectra as a function of solution processing conditions. As the solution aged, an increase in the 0-0 and 0-1 vibrational peaks at 2.0 and 2.2 eV, (620 nm and 564 nm) respectively, was observed, indicating increased P3HT chain interactions through π-π stacking induced aggregation.[105] Figure 3.2b shows the evolution of aggregation calculated from aggregate and amorphous fractions generated by Franck-Condon fits to the spectra using equation A1.[106,142] Aging led to a sharp initial increase in the percent aggregation followed by apparent saturation at 22% aggregates after 96 hours. While sonication for 2 minutes induced some aggregate formation (8%), the highest level of aggregation was achieved for solutions that were both sonicated and aged (all greater than 24%). The highest level of solution aggregation (32%) was achieved by sonication followed by 96 h aging. Considering aggregate formation under a nucleation and growth model, the enhanced level of aggregation observed for the

combined process most likely arises from accelerated growth due to the larger number of nucleation sites, or "seeds" provided by initial sonication.[141] Disentanglement of polymer chains induced by sonication could also enable faster diffusion of free polymer species to aggregate growth fronts.[107]

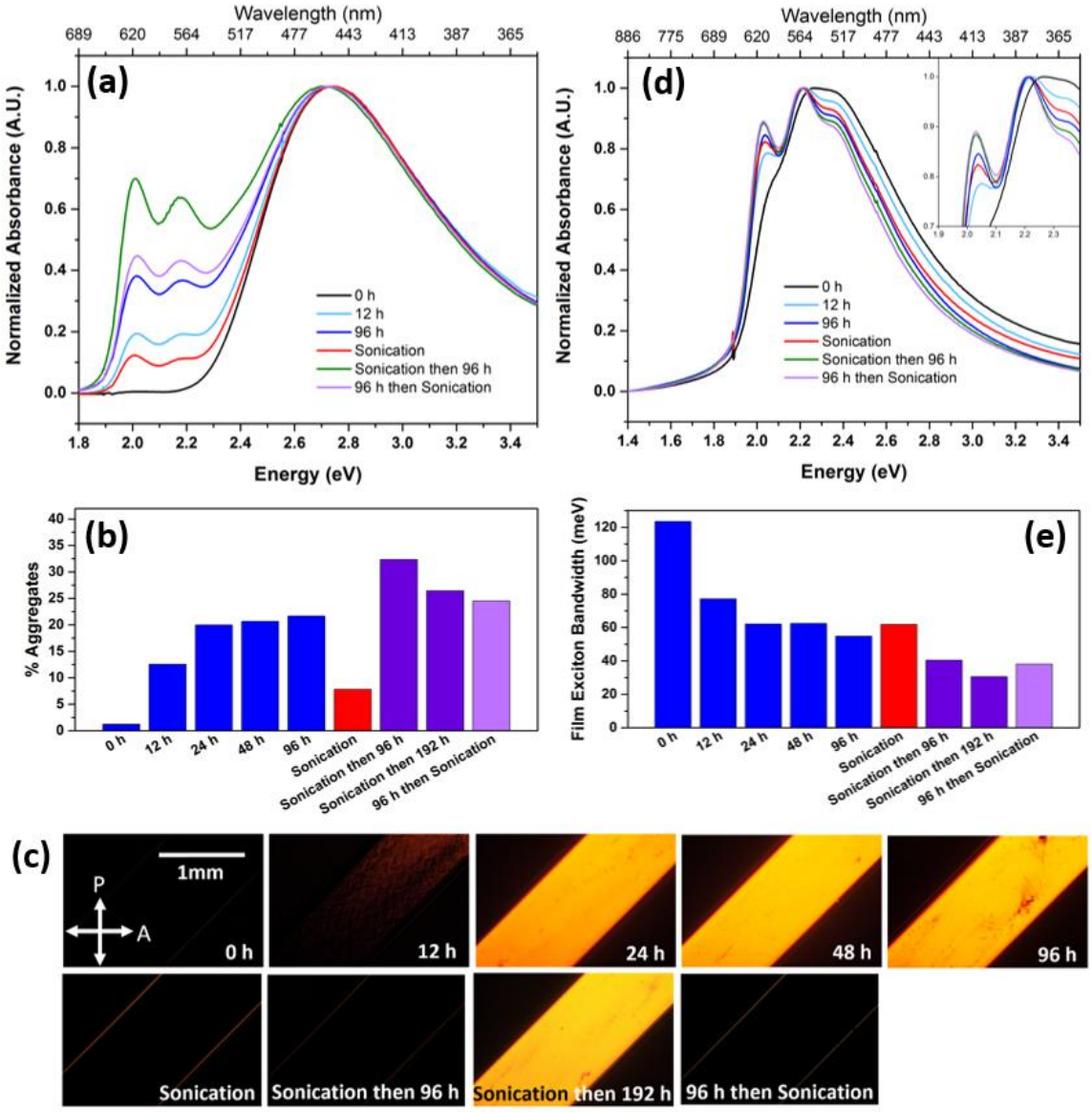

Figure 3.2 (a) Sample UV-vis spectra of P3HT *solutions* processed by aging and sonication techniques. (b) Percent aggregates calculated from the solution UV-vis spectra. (c) Polarized optical microscopy images of solutions processed as indicated before filling 1mm ID capillaries (45° to polarizer). (d) Sample UV-vis spectra of *films*

spin-coated from aged and/or sonicated solutions. (e) Free exciton bandwidth calculated from the film spectra using the Spano model.

In order to probe P3HT solution state orientational ordering, the solutions were loaded into capillaries and viewed through crossed polarizers, as shown in the POM images (Figure 3.2c). With time and increased aggregation levels, the solutions became birefringent and exhibited increased long range ordering (see Figure A - 7 for images showing modulation in transmitted intensity as capillaries are rotated, and for linear dichroism images). Birefringence and long range ordering, however, do not depend merely on the percent of aggregates. Note, the sonicated then aged 96 h solution, as well as the 96 h aged then sonicated solution both appear isotropic (dark) with no apparent long range order within the capillary, despite some of the highest observed levels of aggregation. Thus, other factors must contribute significantly to the formation of birefringent fluids; one key parameter may be the average length of the P3HT nanofibers that form in solution, as discussed below.

Figure 3.2d shows that both aging and sonication increase the intensity of the low energy (0-0) absorption bands in the respective thin-films obtained from the solution-processed conjugated polymer. Thus, the nanofibers formed in solution survive the spincoating process.[59] Further, according to Spano's model, these vibronic bands are related to the free exciton bandwidth (W), which correlates with intrachain ordering along an individual polymer chain.[143] A decrease in W in this context indicates both increased intramolecular ordering and increased average conjugation length.[144–147] Note this exciton bandwidth is different from the electronic bandwidth discussed in the introduction where larger bandwidths correspond to increasingly ordered systems. This relationship between exciton bandwidth and conjugation length in semiconducting polymers is non-intuitive and

comes from numerous studies on cofacial oligomer dimers which showed that once chain length L approximately exceeds the intermolecular separation, the interchain Coulombic coupling decreases with L.[145,147–150] Exciton bandwidth W was calculated using the Spano model from the intensities of the (0-0) and (0-1) vibrational transitions in Equation 11 for P3HT:[151]

$$\frac{I_{0-0}}{I_{0-1}} = \left\{\frac{1 - 0.24W/E_p}{1 + 0.073W/E_p}\right\}^2 \quad (11)$$

where $I_{0\text{-}0}$ and $I_{0\text{-}1}$ are the intensities of the (0-0) and (0-1) transitions, respectively (calculated from fittings of the experimental UV-Vis spectra as demonstrated in Figure A - 9 using modified Franck-Condon progressions fit using equation A1[106]) and E_p is the vibrational energy of the symmetric vinyl stretch (taken as 0.18 eV).[143] Figure 3.2e shows the calculated free exciton bandwidths for the films. Compared to the fresh (pristine) P3HT case (0 h) with a W of 123 meV, decreases in W were observed with longer aging times (down to 55 meV for 96 h aging), as a result of sonication (62 meV), and especially as a result of combinations of aging and sonication (all below 40 meV). These significant reductions in exciton bandwidth point to increased conjugation along the polymer backbone within films cast from solutions processed by sonication and aging.

3.2.2 Atomic Force Microscopy, Polarized Optical Microscopy and Polarized Raman Spectroscopy of Solidified Thin Films

Figure 3.3a displays atomic force microscopy (AFM) phase images of films obtained from the respective processed solutions deposited onto OFET devices. The insets

are images of films on glass as viewed through crossed polarizers (inset images are of points approximately two thirds of the way between center and edge of the sample, with the sample held at the angle producing the brightest image; see Figure A - 8 for multiple angles). While the pristine solution afforded an isotropic (dark) film with no visible fibrillar morphology, aged solutions resulted in films containing long nanofibers; some films appeared birefringent. Comparing Figure 3.2c and Figure 3.3a, all birefringent solutions afforded birefringent films, suggesting that solution state ordering can be transferred to the solid state even through a spin coating process.

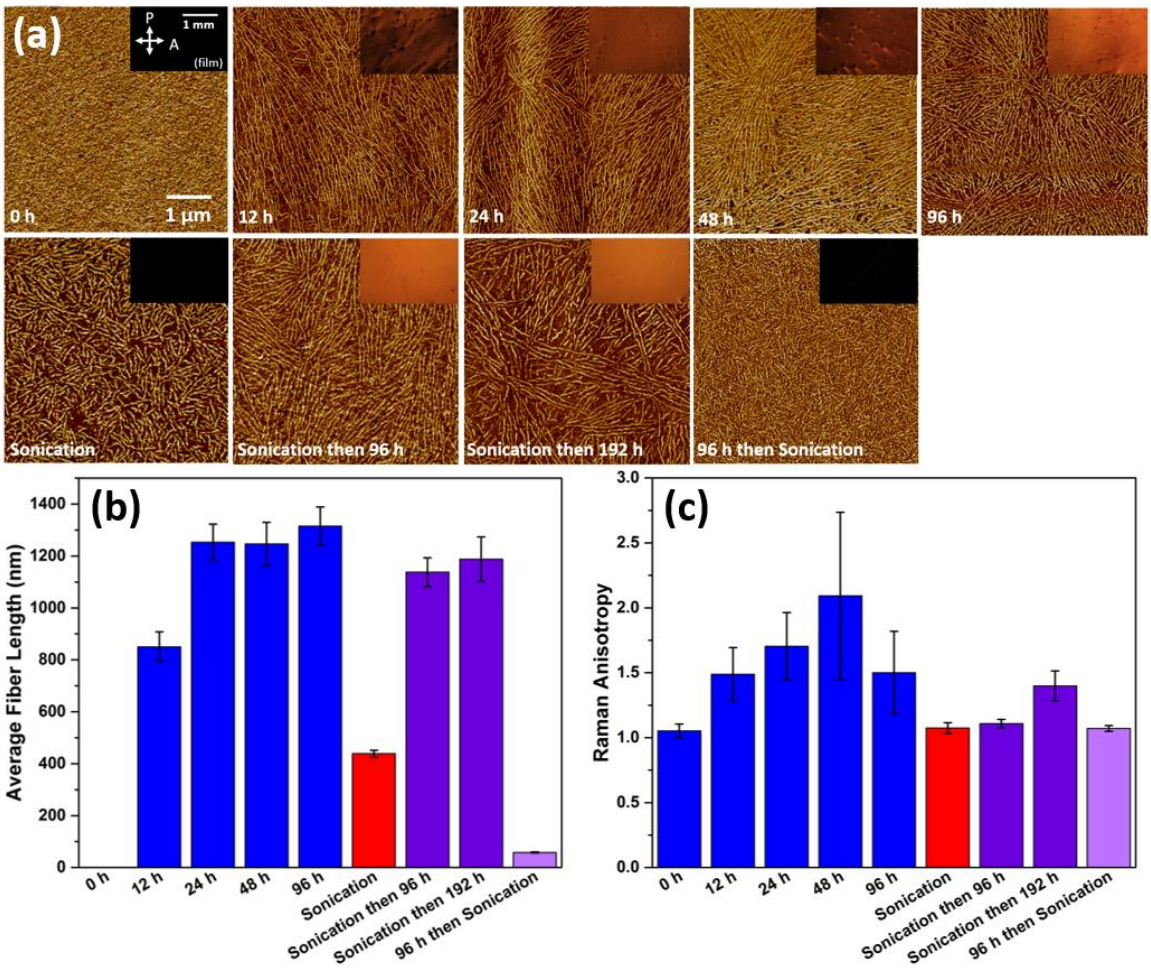

Figure 3.3 (a) AFM phase images of spincoated films (insets are optical images of films as viewed between crossed polarizers), (b) average fiber lengths calculated from the AFM images using FiberApp software[152] with standard error from 70 fibers and (c) Raman anisotropy values calculated from polarized Raman spectra on films as the ratio of the highest intensity to the intensity obtained when the sample was rotated by a further 90°. Raman measurements were taken from 3 locations on the sample to obtain the average anisotropy (error bars are standard deviation from the mean).

As shown in Figure 3.3b, the average fiber lengths within the respective films were quantified by AFM image analysis using the FiberApp software.[152] Fibers were chosen for analysis so that their apparent start and end points fell within the boundaries of the image; 70 fibers were sampled per image. All 3 films that appear isotropic by POM (0 h, sonication, and 96 h followed by sonication) had the 3 shortest average fiber lengths. Thus,

fiber length appears to be closely related to solution and solid-state anisotropy. This could be explained on the grounds that longer rod-like objects more easily align themselves in a dispersion,[153] and that alignment is more likely to be preserved in the solid state. But an additional degree of ordering appears to be present in solid-state AFM images: longer fibers appear in bundles of parallel orientation. This phenomenon was previously observed by Wang et al. in films cast from solutions of P3HT subjected to microfluidic pre-processing.[80] Oriented fiber aggregates could be attributed to physical bridges between neighboring fibers formed by the incorporation of long P3HT chains between fibers, or to thermodynamic effects favoring the formation of ordered fibrillar domains at the liquid-air interface during processing.[154]

All solutions that were isotropic formed isotropic films, with the exception of the sample that was sonicated before 96 hours of aging – this sample was isotropic in its solution state, but birefringent as a thin-film. It is conceivable that the sonicated then 96 h aged sample became birefringent in the solidified film because the film drying process may facilitate additional ordering of the long fibers beyond that which could be achieved in the fluid state. Note that nanofiber growth is expected to continue as solvent evaporates and the film solidifies, as per the nucleation and growth model.[141,155] The differences between "sonication followed by aging" and "aging followed by sonication" are also evident in the AFM images of Figure 3.3a. The short fibers present in the 96 h aged then sonicated sample indicate that long fibers present before sonication (as seen in the 96 h case) broke into smaller fragments upon sonication, resulting in many shorter fibers with isotropic orientation.

As shown in Figure 3.3c, in order to obtain a more quantitative comparison of the solid-state alignment, Raman anisotropy measurements, an effective probe of chain orientation in conjugated polymer thin films, were performed.[156] Raman spectra were measured with parallel polarizers as the films on silicon substrates were rotated on a stage in order to observe the change in P3HT C=C stretching peak Raman intensity calculated using Lorentzian spectral fits. The Raman anisotropy values were calculated as the average ratio of the highest intensity to the intensity obtained when the sample was rotated by a further 90°. Comparison of Figure 3.3b and Figure 3.3c reveals that longer average fiber lengths tend to result in Raman anisotropy values significantly greater than 1, with the exception of the sonicated then 96 h aged sample.

Comparing the Raman anisotropy and POM results, samples that appear isotropic by POM (dark) also appear isotropic by Raman (anisotropy value near 1), again with the exception of the sonicated then 96 h aged sample which showed birefringence and alignment by POM, but which had only a 1.1 Raman anisotropy value. This is likely due to the fact that the micro-Raman spectroscopy employed involves a laser spot size of approximately 1.7 μm (based on a numerical aperture of 0.55 and a laser wavelength of 785 nm), which is probing a region 3 orders of magnitude smaller than in the millimeter scale POM images. Therefore, for this sample, the surprisingly low Raman anisotropy value may indicate that many shorter fibers generated by sonication may have been relatively randomly oriented on the smaller scale of micro-Raman, despite the longer fibers (several microns) generating longer range ordering observable by POM. Overall, the anisotropy results confirm that fiber length, solution-state ordering, and resultant solid-state ordering are closely related. It is unclear whether fiber length drives orientational

order or *vice versa*, or whether both of these structural features are simply the result of the underlying crystallization process and its thermodynamic driving forces.[157]

3.2.3 Film Crystallinity

To further probe thin-film structural properties, films fabricated from solutions processed with the aging and sonication techniques were investigated by grazing incidence wide-angle X-ray scattering (GIWAXS) (Figure 3.4). Diffraction patterns of five representative samples are shown in Figure 3.4a (see all GIWAXS results in Figure A - 10a). Diffraction peaks associated with molecular layering (100, 200, 300) along the q_z direction and corresponding to the inter-lamellar spacing of P3HT (~16.1 Å) normal to the substrate were apparent in all films.[158] Longer aging times resulted in higher intensity peaks, indicating enhanced crystallinity. While the pristine P3HT film exhibited relatively isotropic patterns in the (010) arcs along the in-plane (q_{xy}) axis, films from aged solutions (especially 48 h and onwards) and films from combined sonication and aging gave stronger (010) arcs, likely due to improved P3HT π-π stacking, with crystallites that are well organized, preferentially in an edge-on orientation.[159]

The full width at half-maximum (FWHM) of the (100) diffraction peaks was used to calculate the crystalline domain sizes via Scherrer's equation in reciprocal space (see Figure A - 10b for sample fitting and equation).[160] The grain size (domain size) tended to increase with aging time in the case of pure aging, but decreased with aging time when the solution was sonicated before aging. The d_{010}-spacing, or the π-π stacking distances, were calculated using Bragg's law and the positions of (010) diffraction peaks. The π-π stacking distance did not change significantly from sample to sample (approximately 3.65 Å). The

d_{100}-spacing, or the lamellar stacking distance, varied slightly, ranging from 16.57 Å (24 h aged) to 16.02 Å.

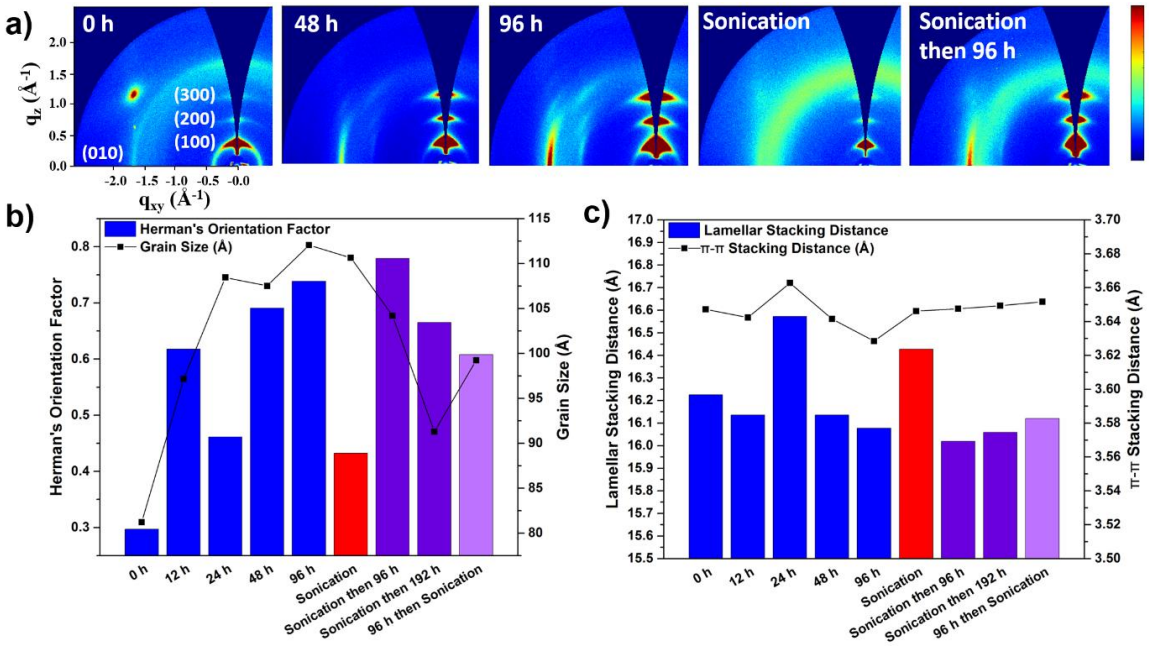

Figure 3.4 (a) 2-D GIWAXS diffraction patterns of 5 representative samples, (b) calculations of Herman's Orientation Factor and grain size and (c) calculations of lamellar stacking distance and π-π stacking distance for all samples.

Since semiconducting polymer electrical properties are closely tied to the crystal orientation, the Herman's Orientation Factor, f_H, was calculated for all samples from the first order alkyl stacking (100) peaks (Figure 3.4b**)**. Values of f_H range can range from -0.5 (indicating a lattice plane oriented perfectly parallel to the substrate, or face-on) to 1 (which denotes crystal planes oriented perfectly perpendicular to the substrate, or edge-on); an f_H of 0 indicates randomly oriented structures.[161] The sample sonicated followed by 96 h aging gave rise to the highest f_H of 0.79, suggesting a highly oriented microstructure of primarily edge-on character, which is expected to facilitate efficient charge transport in the plane of the substate.[159] Comparison of Figure 3.2b and Figure 3.4b reveal a similarity in the trends of Herman's Orientation Factor and % aggregates in solution, which can be

rationalized as follows: a higher number of π-stacked fibers lying flat on the substrate would indeed yield a higher proportion of edge-on thiophene units.

3.2.4 Charge Carrier Mobility

Figure 3.5a presents charge carrier mobilities obtained from films spincoated onto bottom-contact OFET devices, calculated from I-V transfer curves shown in Figure 3.5b. All samples prepared from simply aged solutions exhibited approximately 6-8 fold improved mobility compared with the pristine sample (e.g. 0.013 ± 0.006 $cm^2V^{-1}s^{-1}$ to 0.102 ± 0.015 $cm^2V^{-1}s^{-1}$ for 0 and 96 h aging, respectively), due to the formation of π-stacked aggregates. The sonicated solution had a hole mobility that was similar to that of the 96 h aged solution (average of 0.112 ± 0.003 $cm^2V^{-1}s^{-1}$). The sonicated and then aged 96 h sample afforded the highest mobility (0.149 ± 0.006 $cm^2V^{-1}s^{-1}$), representing a 46% increase over the 96 hour aged sample, a 34% increase over the sonicated material and an 11-fold improvement over pristine P3HT devices. In contrast, a solution aged for 96 hours and then sonicated afforded a low mobility value of 0.022 ± 0.001 $cm^2V^{-1}s^{-1}$, likely due to an increase in grain boundaries that are not well connected, created when the P3HT fibers formed during aging are broken during the sonication process (note the short fiber lengths observed in Figure 3.3).

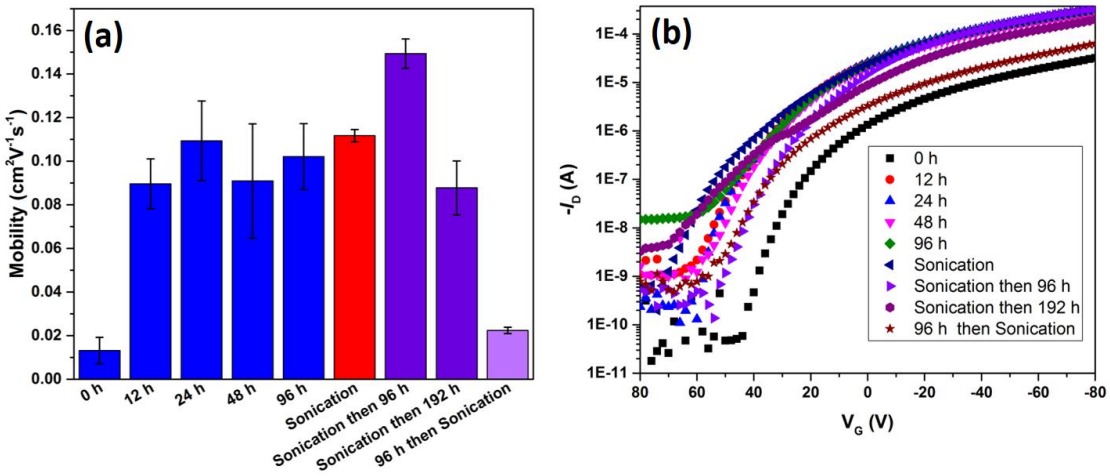

Figure 3.5 (a) Average field-effect mobilities of P3HT films spincoated on bottom-contact OFET devices, calculated at a V_D = -80 V. Four devices were characterized for each set of conditions. Error bars show standard deviations from the mean. (b) Transfer characteristics of the P3HT films.

It would be mechanistically informative to identify the structural features that best explain the trends in mobility. It is tempting to cite Herman's Orientation Factor (Figure 3.4b) and the percent aggregates in solution (Figure 3.2b) as the principal structural features driving electrical performance, because both display plateau-like behavior for aged devices and reach a maximum (32% and 0.78, respectively) for the highest performing device. An edge-on grain orientation relative to the dielectric substrate, indicated by the high value of Herman's Orientation Factor, has long been known to facilitate charge transport by placing the lattice vectors with the highest degree of electronic delocalization in the plane of active charge transport.[159] From UV-vis, a high fraction of aggregates in solution should correspond with the formation of more π-π stacking interactions, which are also beneficial to charge transport.[33,105] Plots of mobility as a function of eight measured structural parameters are provided in Figure A - 12 of the appendix.

However, the sonicated device and the 96 h aged then sonicated device seem to contradict this analysis. The former has the second highest mobility, yet the second lowest Herman's Orientation Factor, and second lowest percent aggregates in solution. In fact, every quantifiable structural feature of the sonicated device other than (100) grain size and film exciton bandwidth suggest it should be one of the two worst devices of the set. On the other hand, the 96 h aged then sonicated device displays the second lowest mobility, while it still demonstrates the third highest percent aggregates in solution and average characteristics from GIWAXS.

Perhaps this can be rationalized by considering the impact of grain boundaries. Sonication clearly breaks pre-formed P3HT nanofibers into smaller segments, as evidenced by the difference in fiber length between the 96 h aged sample and the 96 h aged then sonicated sample (Figure 3.3b). Despite extensive fiber break-up, the percent aggregates in solution remains high (Figure 3.2b); it stands to reason that five 200 *nm* P3HT nanofibers would absorb nearly as much incident radiation as a single 1000 *nm* nanofiber. The breakup of fibers in solution, however, would create many additional grain boundaries along the interface through which charge must flow.

Salleo et al. suggest that the "softness" of grain boundaries is a significant factor in determining the mobility of a given material sample.[57] It is conceivable that the small fibers in the 96 h aged then sonicated device are poorly connected and plagued by grain boundaries with deep electronic traps or even vacancies, whereas the grain boundaries between the small fibers in the just sonicated device are filled favorably by the freestanding polymers in that solution. The high percentage of aggregates in solution for the 96 h aged then sonicated device suggests that fewer freestanding polymer chains are available to

favorably fill in the amorphous grain boundaries in the resulting film. Additionally, aging likely favors the folding of long, dangling polymer chains into the crystalline lattice of the nanofibers, preventing these polymers from becoming effective "tie chains" after sonication breaks the fibers into smaller pieces.[162]

The above discussion is indicative of the shift toward the characterization of grain boundary morphology in the study of polymeric transistors. The electrical performance of crystalline silicon, after all, is defect-driven.[163] While semi-crystalline polymeric transistors will never approach crystalline inorganics on the spectrum of defect density, it is nonetheless worthwhile to consider the structure-property relationship from this standpoint. Recent modeling efforts have begun to focus more on the effect of inter-grain connections, and it is acknowledged that inherent paracrystalline disorder places a limit on overall device performance as well.[33,164] It is likely that the structure of grain boundaries and polymer crystal defects will play a more important role in research as both characterization tools and our understanding of these materials improve.

3.3 Conclusions

As summarized in Figure 3.6, the results presented in Chapter 3 show that P3HT fiber length plays an important role in the formation of birefringent fluids of P3HT solution with long-range order, as well as in the formation of anisotropic thin films. Whereas sonication alone produces shorter fibers that have isotropic orientation both in the solution and thin film states, aging for sufficient duration can lead to longer fibers that provide for orientational order both in solutions and thin films. When inducing aggregation by both sonication and aging, the sequence of techniques plays an important role. Sonication of aged solutions composed of longer fibers effects breakup of the fibers into smaller segments, with concomitant increase in void-filled grain boundaries and lower charge carrier mobility. On the other hand, sonication prior to aging affords the highest levels of aggregation due to accelerated nucleation and growth. The combined sonication/aging technique gives rise to samples that exhibit the highest charge carrier mobility (approximately 0.15 $cm^2V^{-1}s^{-1}$) among the alternatives explored here. This value represents an 11-fold increase over pristine P3HT, and is significantly higher than the mobility achieved by sonication or aging alone. The sonication process resulted in a delay in the onset of birefringence. Presumably, the presence of smaller particles interferes with fiber alignment in the fluid state. Also, films fabricated from sonicated solutions did not show a high degree of anisotropy.

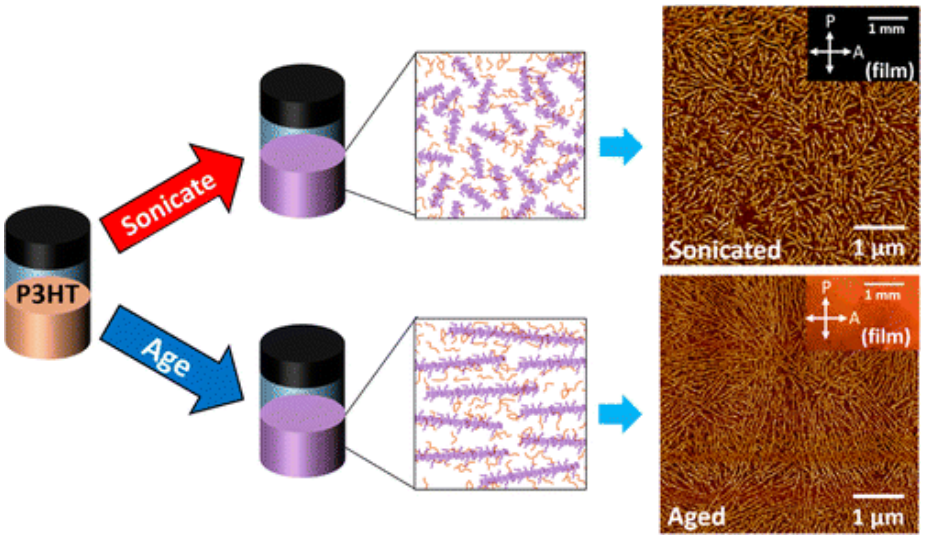

Figure 3.6 Visual summary of some of the main results of Chapter 3.[165]

Importantly, semiconducting thin-film anisotropy was not the most important determinant of mobility. Analysis of all the mobility results point to the significance of grain boundaries in addition to fiber length. Films composed of fibers induced by sonication alone may still have a sufficient number of free chains to effectively connect grains, whereas short fibers generated from sonicating an aged solution are plagued with grain boundaries that are likely poorly connected and plagued with vacancies. The results indicate the need for careful consideration of grain boundary morphology in polymeric semiconducting films. Given that solution phase P3HT fiber length and solid-state ordering play significant roles in electronic performance, further alignment methods such as blade coating and substrate rubbing could be employed with appropriate solution phase semiconducting polymer aggregation techniques to take full advantage of lyotropic liquid crystalline characteristics. This study provides significant insight into the role of long range ordering in conjugated polymer fluids and thin films along with subtleties that impact ordering and conjugation length within solidified films. The mechanistic analysis will

create new research opportunities that will enable future high performance organic electronic devices.

3.4 Experimental

Materials. Regioregular P3HT was purchased from Rieke Metals Inc. (catalog no. RMI-001EE, Regioregularity = 96% HT, Mw = 71 kDa, PDI = 2.2) and used without further purification. Chloroform (anhydrous) was purchased from Sigma-Aldrich and used without further purification. For POM studies, borosilicate glass capillaries of dimensions 0.1 × 1 × 50 mm were purchased from Vitrocom Inc. and used without any further surface treatment. Silicon wafers (n-doped) were purchased from Rogue Valley Microdevices Inc. with a thermally grown 300 nm thick SiO2 dielectric for OFET fabrication.

Solution Processing of P3HT. A chloroform-P3HT solution (5 mg/mL) was prepared in a 20 mL borosilicate glass vial by heating to 70 °C for approximately 30 min until fully dissolved. The solution was then left to cool to room temperature. At room temperature (but still orange), a syringe was used to take up the solution and inject it back through an 18 guage needle before aging or sonication took place. Vials were wrapped in parafilm and stored in a dark cabinet for aging. For sonicated solutions, the sealed vial was ultrasonicated for 2 min using a tabletop bath-type ultrasonicator (Bransonic 2510, 40 kHz, 130 W) filled with tap water. All solution processing was done in air.

Organic Field-Effect Transistor (OFET) Fabrication and Characterization. OFET devices with bottom-gate, bottom-contact geometry were fabricated to test the electrical properties of the P3HT films. Highly n-doped silicon wafers with a 300 nm SiO_2 dielectric layer were used as the substrate. The doped silicon was used as the gate electrode with the

SiO_2 dielectric on top. Source and drain contacts were fabricated using a standard photolithography based lift-off process in a cleanroom, followed by E-beam evaporation of the Cr (3 nm) adhesion layer and the Au (50 nm) contacts. Prior to spincoating the processed P3HT solutions, the OFET substrates were cleaned by sonication in acetone for 10 minutes followed by rinsing with acetone, methanol and isopropanol, followed by cleaning in a UV-Ozone chamber (Novascan PSD-UV) for 15 min to remove organic contaminants. P3HT solutions were spincoated on the cleaned devices at 800 RPM for 30 s in air (WS-650MZ-23NPP, Laurell). Devices were patterned by removing excess P3HT from areas surrounding the channel, then left in a vacuum oven overnight at 50 °C to remove any residual solvent. The devices were tested in a nitrogen environment using an Agilent 4155C semiconductor parameter analyzer. The field-effect hole mobility was calculated under transistor operation (V_{DS} = -80 V; V_G = 80 to -80V) by plotting the square root of the drain current (ID) vs gate voltage (V_G) and obtaining the slope to extract the mobility according to the following equation:[72]

$$I_D = \mu C_o \frac{W}{2L}(V_G - V_T)^2 \quad (12)$$

where W (2000 µm) and L (50 µm) are the transistor channel width and length, respectively, V_T is the threshold voltage, and C_o is the capacitance per unit are of the SiO2 gate dielectric (1.15×10^{-8} F cm^{-2}). For each solution condition, 4 devices were measured to obtain average mobility values.

UV-Vis Spectroscopy. An Agilent 8510 UV-vis spectrometer was used to measure absorption spectra on films (spincoated on pre-cleaned glass slides at 800 RPM for 30 s), and solutions (placing droplet between glass slide and cover slip and securing with clips.

Atomic Force Microscopy. AFM measurements were performed on the same devices used for OFET measurements, using a ICON Dimension scanning probe microscope (Bruker) in tapping mode with a silicon tip (NSC-14, MikroMasch).

Polarized Optical Microscopy. POM images were obtained using a Leica DMRX optical microscope equipped with a rotatable polarizer and analyzer and a rotatable stage. Images were captured using a Nikon D300 digital SLR camera.

Raman Micropectroscopy. Raman spectra were obtained using a 50× objective and a 785 nm laser light source (Kaiser OpticSystem) that has 4 cm^{-1} resolution in the backscattering geometry. Spectra were acquired at a laser power of 20 mW with 6 s exposure time and 6 accumulations each. For each spectrum, the peak corresponding to C=C stretching was fit to a Lorentzian function using Holograms software to obtain peak heights.

Synchrotron Radiation Characterization. GIWAXS measurements were carried out on beamline 11–3 at the Stanford Synchrotron Radiation Light Source (SSRL). The beam was kept at an energy of 13 keV and the critical angle of measurement was 0.12°. A LaB6 standard sample was used for calibration. Using the calibration, wavelength and sample-detector distance (400mm), the 2-D images were corrected from intensity vs pixel position to intensity vs. q-spacing using WxDiff software. 2-D images were reduced to 1-D plots via integration of cake segments and analyzed using Origin Pro software for peak fitting.

Films: Effects of Fiber Length and Grain Boundaries on Anisotropy and Mobility. *Chem. Mater.* **2016**, *28* (11), 3905–3913.

CHAPTER 4. BLADE COATING TECHNIQUE FOR CONTROLLED ALIGNMENT OF P3HT NANOFIBERS AND EFFECTS ON CHARGE TRANSPORT

4.1 Introduction

As demonstrated in the preceding chapters, the material properties and performance of organic thin films for electronics can be significantly impacted by the solution processing method.[166] In terms of deposition methods to form thin films from these solutions, the previous chapter focused on spin coating as a common laboratory scale technique. This chapter, however, presents a facile single-step blade coating approach which is not only less wasteful of solvent and more amenable to large scale roll-to-roll fabrication,[167] but which we also observed to facilitate enhanced alignment of P3HT nanofibers as indicated by both optical dichroism, and the anisotropic charge transport achieved. Alignment of organic semiconductors is desirable as charge transport may be fastest along a particular crystallographic direction and if this direction could be oriented along the channel length of an organic field-effect transistor, charge mobility could be increased.

In Chapter 2 it was demonstrated that P3HT forms self-assembled nanofibers that can be aligned in capillaries.[139] Further investigations described in Chapter 3 showed that such alignment of P3HT nanofibers in solution depends on the fiber length which can be controlled using combinations of sonication and aging techniques to induce self-assembly.[165] Additional experiments revealed that ordering in solution can lead to thin-

films that have long range order through spin-coating. However, these studies did not show a clear relationship between nanofiber alignment in the film and resulting charge transport. Here we report a study in which the alignment of P3HT in the film is controlled through a blade coating process, a technique that not only reduces the amount of solvent that is used and is amenable to roll-to-roll solution printing on flexible substrates for low-cost, large scale manufacturing, but also provides a means of tuning the charge transport based on the desired alignment of the nanofibers.

Aligning semiconducting polymers from solution has typically required multi-step deposition techniques which may include pre-treatment of the substrate or post-treatment of the film after deposition. These methods include, for example, templating by a substrate (by friction transfer or mechanical alignment via abrasion) via an aligned, well-ordered polymer followed by casting a semiconducting polymer on top with or without additional heating to induce a liquid crystal phase transition.[168–170] While effective, this kind of alignment requires multistep processing. Friction transfer approaches have been applied directly to conjugated polymers, but the overall process requires additional steps for alignment such as thermal treatment.[171] A recent study by Bao at al showed blade coating of a poly(diketopyrrolopyrrole-terthiophene) solution in which dichroic ratios up to ~7 were observed in the thin films, but for which no charge transport anisotropy was observed.[172] Another study using DPP-BTz (Figure 1.2) showed high anisotropy and faster mobility in the direction of alignment.[173] Herein we report the alignment of P3HT nanofibers (formed simply by aging of a 5mg/mL P3HT/$CHCl_3$ solution) by blade coating that results in both optical anisotropy (dichroic ratios ~3) and charge transport anisotropy (twice as fast in the vertical direction vs nanofibers parallel to OFET channel length). In

this case, the fastest mobility is in the direction perpendicular to the blading direction. This study presented in this chapter enhances both our ability to control P3HT nanofiber alignment and our understanding of how this alignment affects charge transport in OFET devices.

4.2 Results and Discussion

4.2.1 Optical Dichroism

In order to quantify the alignment obtained from films obtained by blade coating and spin coating of aged P3HT solutions, polarized UV-Vis absorption was performed. Figure 4.1a shows the change in absorption of the film as the sample is rotated either 0° or 90° with respect to the incident polarization. Because the transition dipole moment of these conjugated polymers expected to be along the backbone, the absorption of the polarized light will be stronger when more of the chains are aligned in the direction of the polarization.[172] We define a dichroic ratio, *R*, to be the absorption of the 0-0 vibrational peak with the blade coating direction perpendicular to the incident polarization divided by the absorption in the parallel position ($R = A_{\perp}/A_{\parallel}$). An isotropic sample would be expected to have the same absorption regardless of its orientation with respect to the incident polarization and would therefore have a dichroic ratio equal to approximately equal to 1, which can be seen in Figure 4.1b, c. For blade coated samples, however, the absorption was approximately 3 times higher on average when the direction of blading was oriented perpendicular to the incident polarization compared with the parallel case. This dichroic ratio for blade coated samples indicates that the P3HT chain backbones are aligned parallel to the incident polarization when the blade coating direction is perpendicular to the

polarization. This orientation is to be expected if the blade coating aligns P3HT nanofibers in the direction of the blade, while the π-stacked P3HT chains are oriented perpendicular to the fiber long axis, as demonstrated in previous chapters.[139] The UV-Vis results confirm that significant alignment has been achieved by blade coating compared with no large scale alignment observed for spin coating. As discussed in section 4.2.2, the AFM phase images confirm the alignment of P3HT nanofibers in the direction of blading, and random orientation in the case of spin coating.

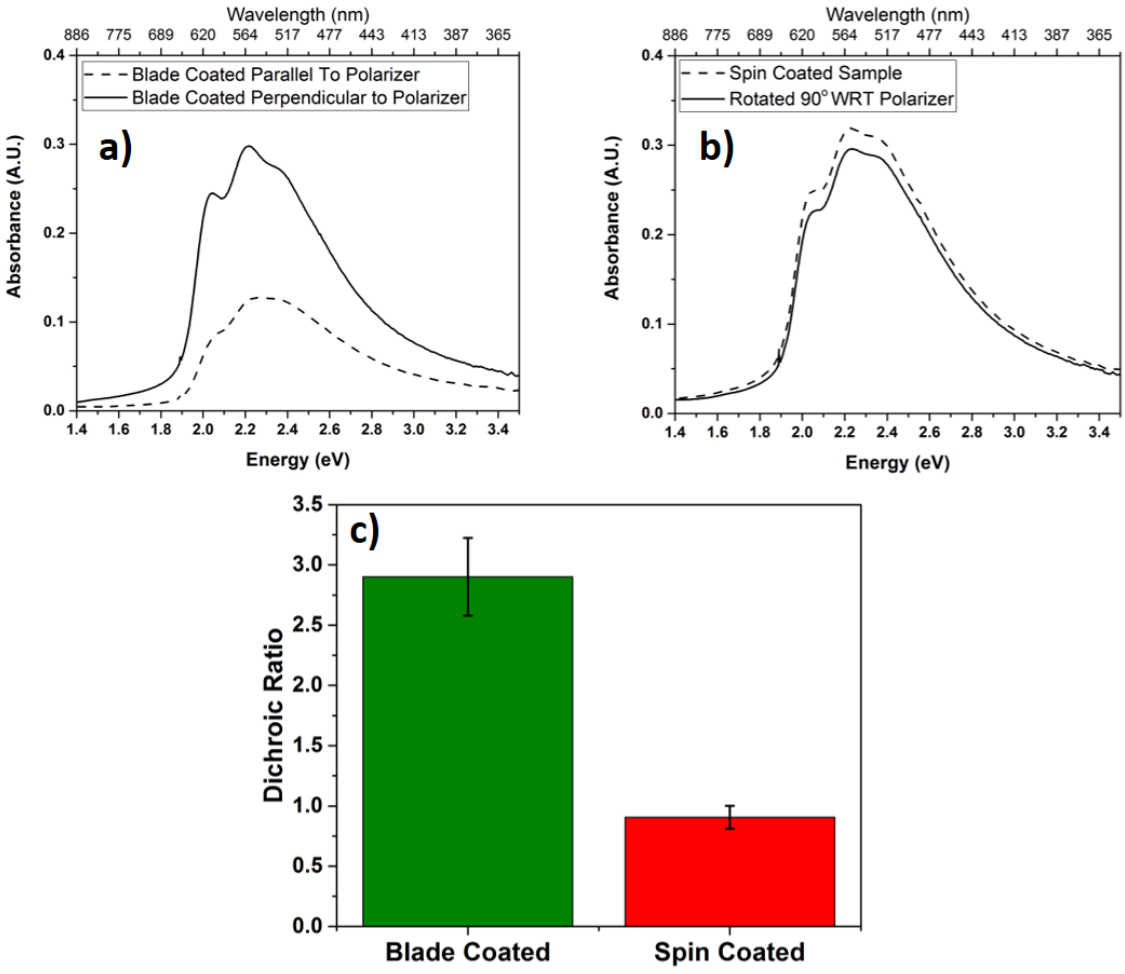

Figure 4.1 Polarized UV-Vis absorption spectra of (a) blade coated P3HT film with the blading direction oriented parallel and perpendicular to the incident polarization; b) Spin coated P3HT film. (c) Dichroic ratio (*R*) calculated from the intensity of 0-0 vibrational peak at perpendicular orientation divided by that at parallel orientation.

4.2.2 Atomic Force Microscopy

Figure 4.2 shows representative atomic force microscopy phase images of both blade coated and spin coated samples. All samples indicate a morphology of densely packed nanofibers which is to be expected after 4 days of nanofiber self-assembly in the aged P3HT solution. The overall alignment of the fibers consistently matches the blade coating direction, indicated by the arrow, while the fibers in the spin coated samples have very little long range orientational order despite some local bundling of fibers. These results suggest a high degree of control over nanofiber orientation simply by changing the direction of blade coating. While these images are of the top surface of the film, the same overall alignment is expected on the bottom of the films (where the semiconducting polymer layer meets the dielectric and where charge accumulation and transport takes place) due to recent AFM experiments on the bottom of the films by Choi et al,[174] and other recent results obtained by the Reichmanis group. In order to provide a more robust quantitative analysis of the information available in the AFM data, an image analysis tool was employed to measure orientational order from each image obtained. The S_{2D} order parameter is one outcome of this analysis, as displayed below each AFM image in Figure 4.2.

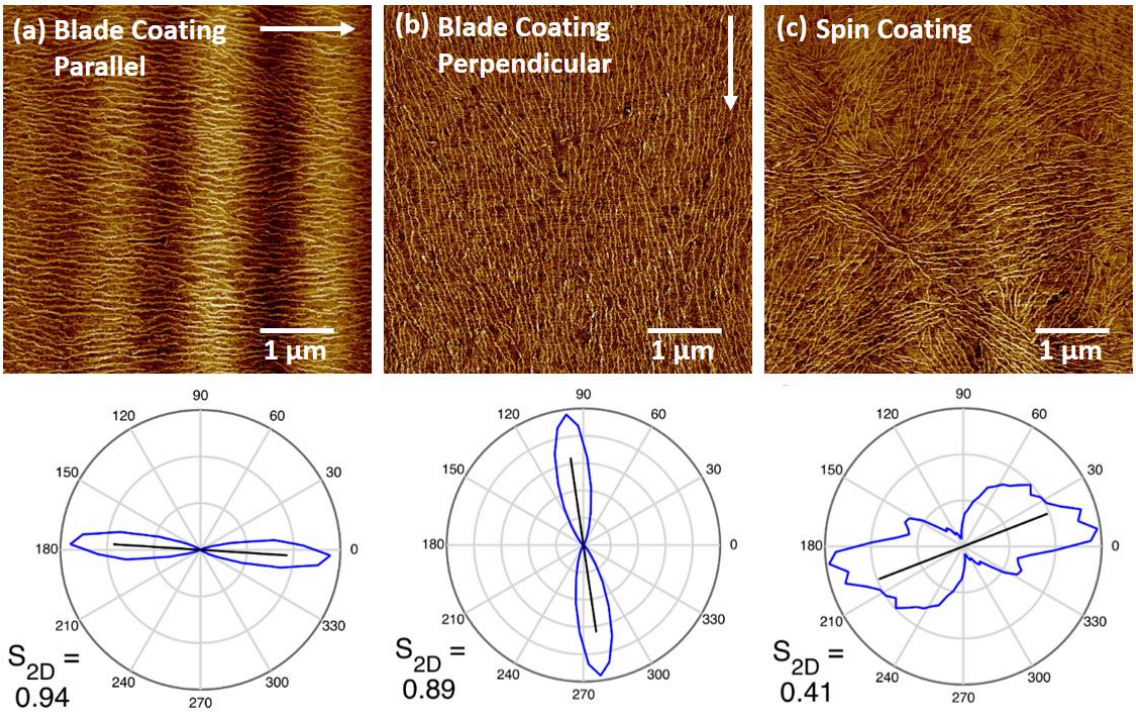

Figure 4.2 AFM phase images of thin films from 4-day aged P3HT / Chloroform solution deposited by (a) blade coating parallel to OFET channel length, (b) blade coating perpendicular, and (c) spin coating. Below each image is the corresponding orientational order map indicating the overall alignment direction and the distribution of fiber angles for each pixel.

In Figure 4.3, the various results obtained from the image analysis are introduced. Figure 3A is a 5×5 µm AFM phase channel micrograph of a P3HT thin film deposited from a solution of P3HT in chloroform (5 mg/mL) *via* blade coating in the perpendicular direction to the OFET channel. This image is used as an example as each image processing step is described. The Orientation Map, Figure 4.3b, is the final result of the processing workflow developed by Persson et al.:[175] an image in which each fiber is represented by a backbone of single pixel width, and each of those pixels is labeled with an orientation from 0 to 180°, as indicated by the attached color wheel. Two other principle results can be obtained: an orientation distribution (Figure 3C) and the decay of orientational order as a function of frame size (Figure 3D).

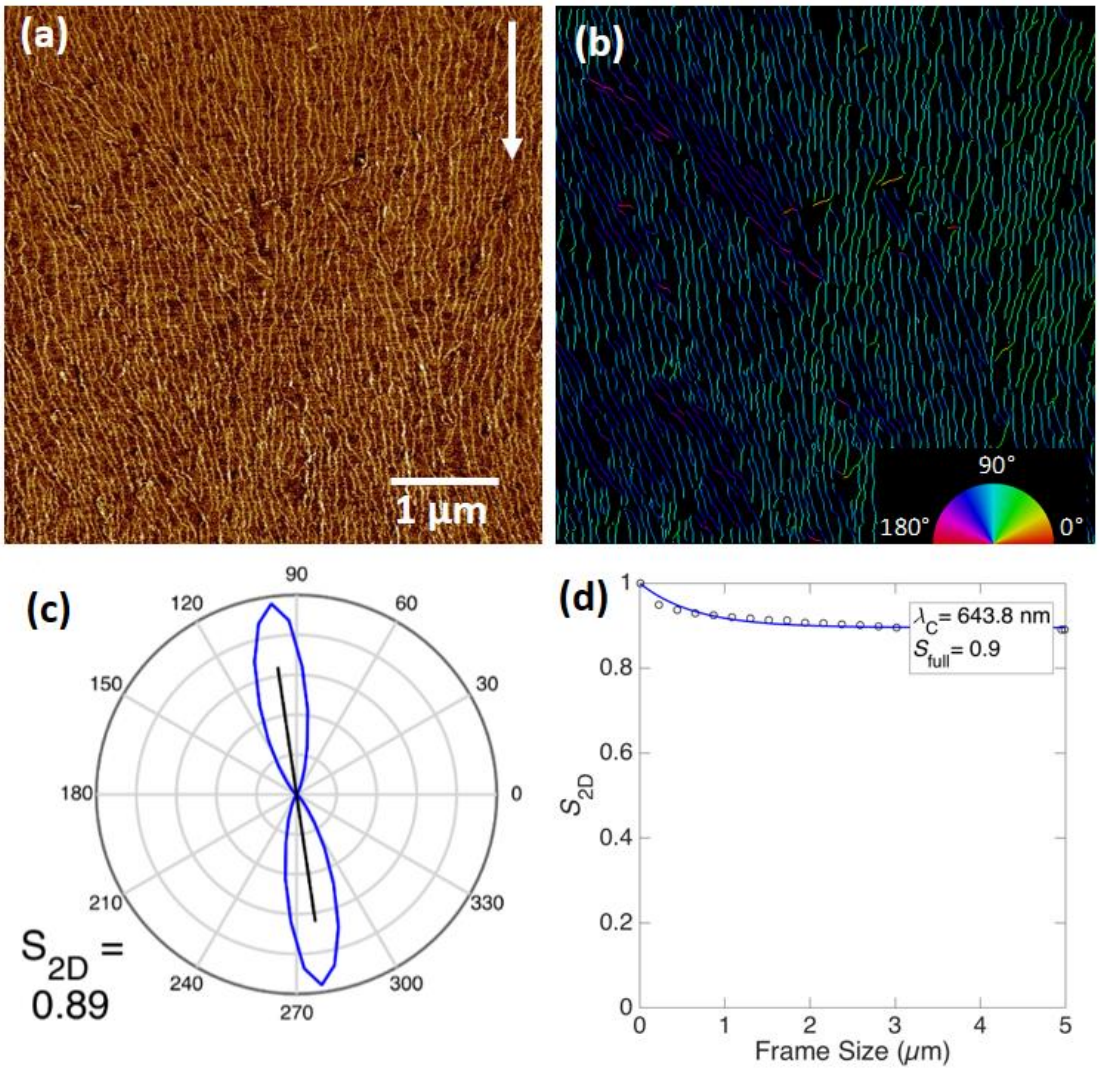

Figure 4.3 Components of the AFM image analysis. (A) Phase channel of a tapping mode AFM image. (B) False color Orientation Map extracted from the original image. Each pixel's orientation corresponds to an orientation on the attached color wheel. (C) Orientation Distribution extracted from the Orientation Map. The radial axis indicates the count of pixels of a given orientation. A diametrical black line segment indicates the average orientation, and the full-frame value of S_{2D} is indicated at bottom left. (D) Decay of the orientational order parameter, S_{2D}, as a function of frame size. Fitted model parameters are indicated at upper right.

The orientation distribution in Figure 4.3C indicates that the nanofibers have an average orientation of ~95° off of the horizontal, and that the distribution is rather narrow. The radial axis of the orientation distribution counts pixels whose orientations fall into each

of 36 bins of 5° widths. The variance of the orientation distribution is captured by the orientational order parameter $S_{2D,}$[154,176] defined mathematically as:,

$$S_{2D} = 2\,\langle cos^2\theta_n\rangle - 1 \tag{13}$$

where θ_n is the angle between an individual fiber pixel and the image's overall director, $\vec{n}$, which is the average orientation of the fibers plotted as a black line segment in Figure 4.3c. Therefore, S_{2D} varies between 0 (isotropic) and 1 (perfectly ordered).

4.2.3 Polarized Optical Microscopy

Figure 4.4 shows the polarized optical microscopy images which further demonstrate the long range ordering that is achieved by blade coating. While the AFM results confirmed the presence of alignment of P3HT nanofibers on the scale of the image (5 µm × 5µm), the UV-Vis results and the POM results with the accompanying scale bar indicate that there is significant alignment over a much larger range (millimeters) achieved by blade coating (Figure 4.4b). Figure Figure 4.4a and Figure 4.4d shows that the aged solution itself displays long range ordering when filled into a capillary tube, consistent with the results in previous chapters.

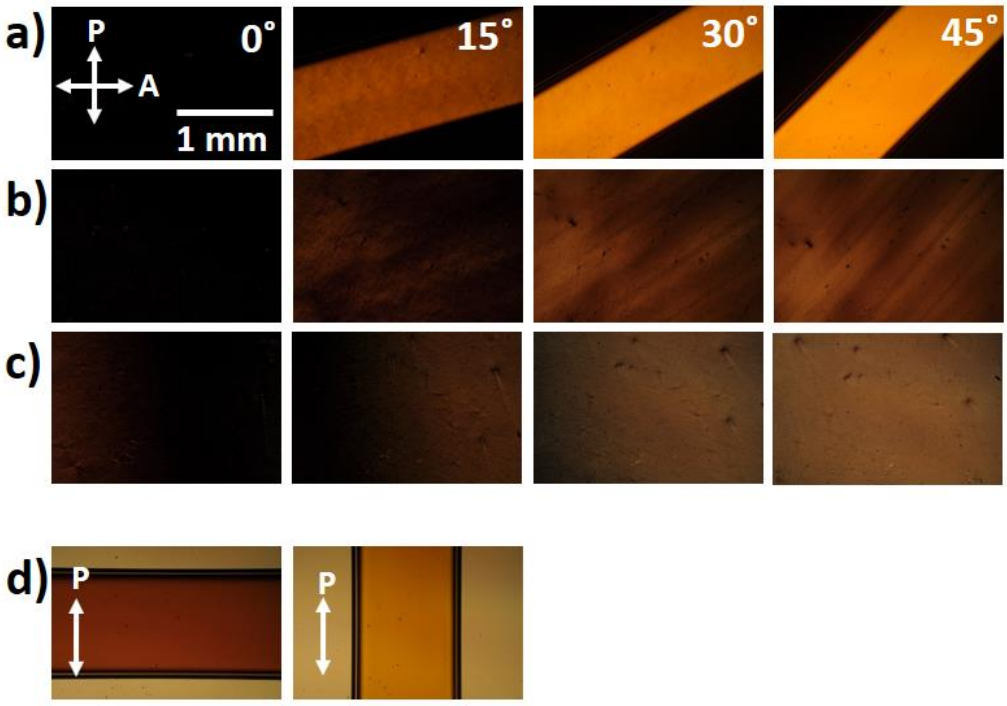

Figure 4.4 Polarized Optical Microscopy images taken of (a) 4-day aged P3HT solution which was then filled into a 1mm ID rectangular capillary (rotated in increments of 15° with respect to the analyzer) (b) blade coated thin film, (c) spin coated thin film and (d) Polarizer only, showing linear dichroism as sample is rotated. All samples were prepared from 4-day aged P3HT solution.

POM results also demonstrate that blade coating alone is not sufficient to form aligned thin films. As shown in **Figure 4.5**, a film blade coated from solution that has not aged sufficiently (1 day) appears isotropic while a film blade coated from a solution aged 2 days appears birefringent with long range ordering. Thus, the assembly of P3HT into fibers is first required in order for the blade coating process to align the P3HT in the desired direction.

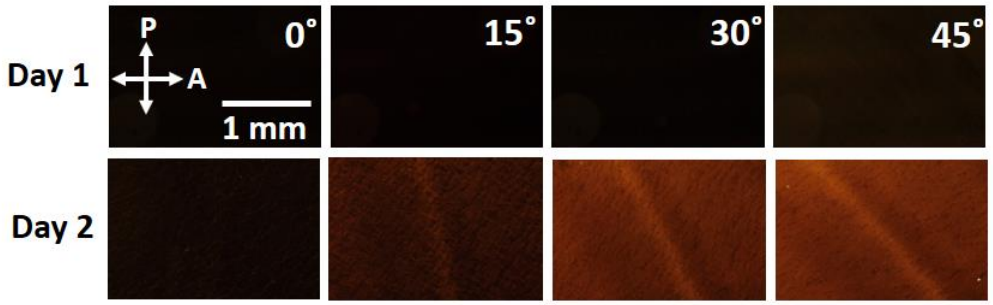

Figure 4.5 Blade coated film from a 1-day old solution vs blade coated film from a 2-day old solution. Blade coating a solution that is insufficiently aged results in isotropic films. Nanofiber formation is first required in order for the alignment to take place.

4.2.4 Organic Field-Effect Transistor Results

Figure 4.6 shows the average hole mobility for the three deposition techniques of aged P3HT solution onto bottom-gate, bottom-contact OFET devices. The direction of blade coating makes a significant impact on the mobility. Blade coating perpendicularly (vertical) to the channel length results in an average mobility of 0.124 $cm^2V^{-1}s^{-1}$, which is exactly twice as fast as the mobility achieved when the blading direction is parallel to the channel length. Meanwhile, spin coating, which does not allow for control of the alignment of the fibers results in a mobility in between that of parallel and vertical coating.

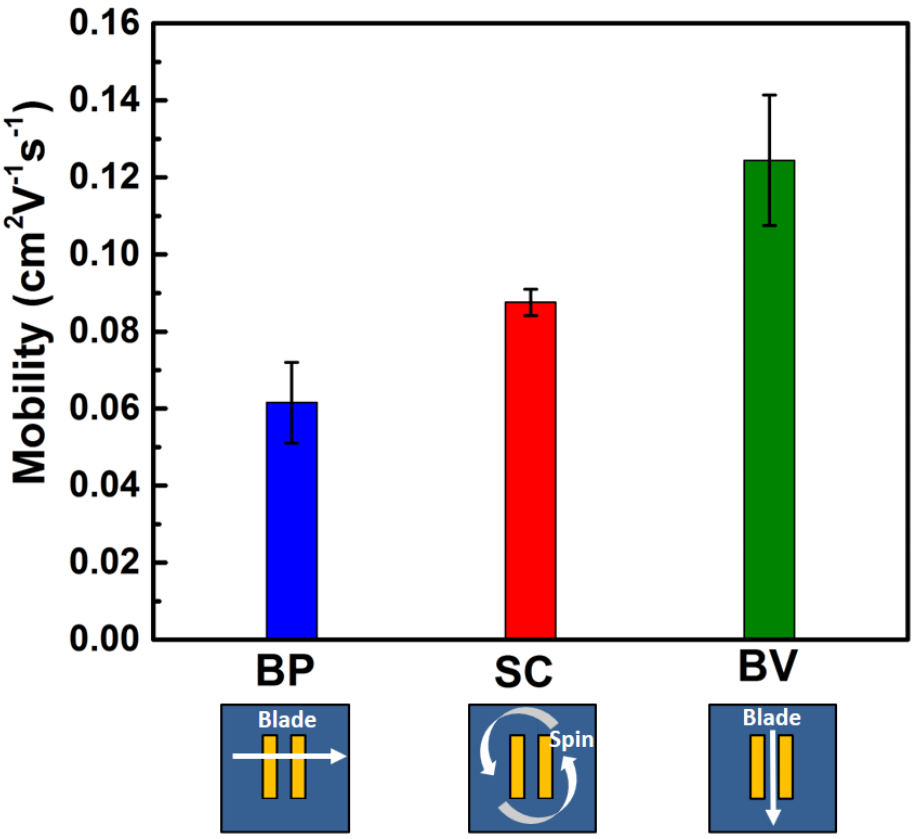

Figure 4.6 Charge carrier mobility calculated from the saturation regime of OFET operation for (a) blade coated parallel to channel length (BP), (b) spin coated (SC), and (c) blade coated perpendicularly, vertical with respect to channel length (BV).

These results indicate that the greater the number of vertically aligned P3HT fibers across the length of the OFET channel, the faster the hole mobility. As indicated in Figure 1.9, the P3HT backbones are stacked on top of each other to form nanofibers through π-π interactions. Therefore, a greater number of nanofibers aligned perpendicularly to the channel length means that a greater number of P3HT backbones are aligned parallel to the channel length. While one might expect charge hopping (inter-chain charge transport), facilitated by π-π stacking to be the most important mechanism of charge transport over the 50μm channel length, the mobility results indicate that the faster intra-chain transport contributes significantly to enhancing the mobility across the length of the channel. As

discussed in the introduction, hole transport across an individual P3HT chain backbone can occur much faster than in the case of charge hopping from chain to chain.

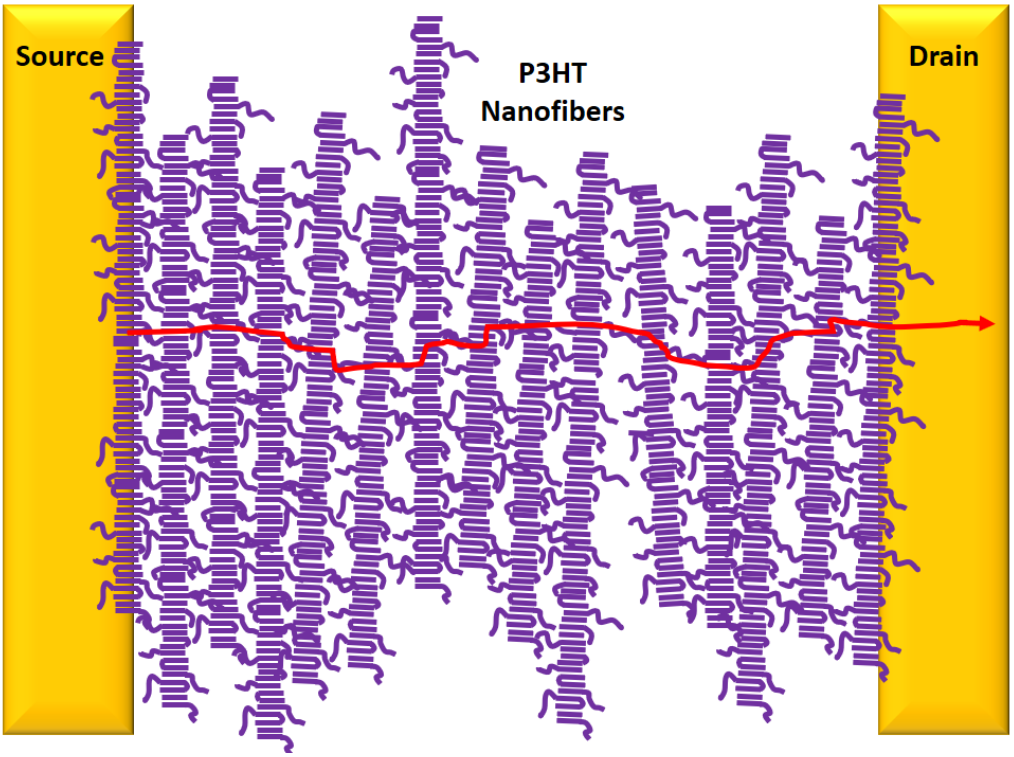

Figure 4.7 Proposed explanation for faster charge transport when P3HT nanofibers are oriented perpendicular to channel length, taking advantage of faster intrachain trasport in desired direction, and the presence of tie chains bridging nanofibers to minimize the impact of the grain boundaries. Red arrow indicates path of a hole moving across channel from source to drain electrode in an OFET.

Figure 4.7 is an illustration of the proposed charge transport mechanism leading to faster mobility in the case of nanofibers aligned perpendicularly to the OFET channel length. The greater proportion of horizontal P3HT backbones allows a more direct route along the intra-molecular pathway (in which transport occurs faster than in hopping between chains). Charges move efficiently across P3HT backbones until the end of a fiber is reached, and the charge then moves through π-π stacking of tie chains into the next ajoining fiber which is closeley aligned, minimizing disruption due to grain boundaries.

Using the weight average of P3HT used in this study, 90 kDa, and the monomer molecular weight, 168.30 Da, the weight average degree of polymerization is 535. Using Chemdraw® to calculate the end-to-end distance of a planarized 4 thiophene unit oligomer and dividing by 4, the contribution from one monomer is 3.47 Å, meaning a weight-average chain would be 3.47 * 535 or 1,856 Å, or about 186 nm long in end-to-end distance. Using the number average instead, this would be about 81 nm of contour length for a single chain. AFM images indicate that there are 45 parallel fibers in a 5 micron width image, meaning ~110 nm between the centers of adjacent fibers. With tie chains extending out of both sides of a fiber that are approximately 80 nm (number average) or 180 nm (weight average) in contour length, there is more than enough length to possibly connect adjacent fibers when these chains are extended.

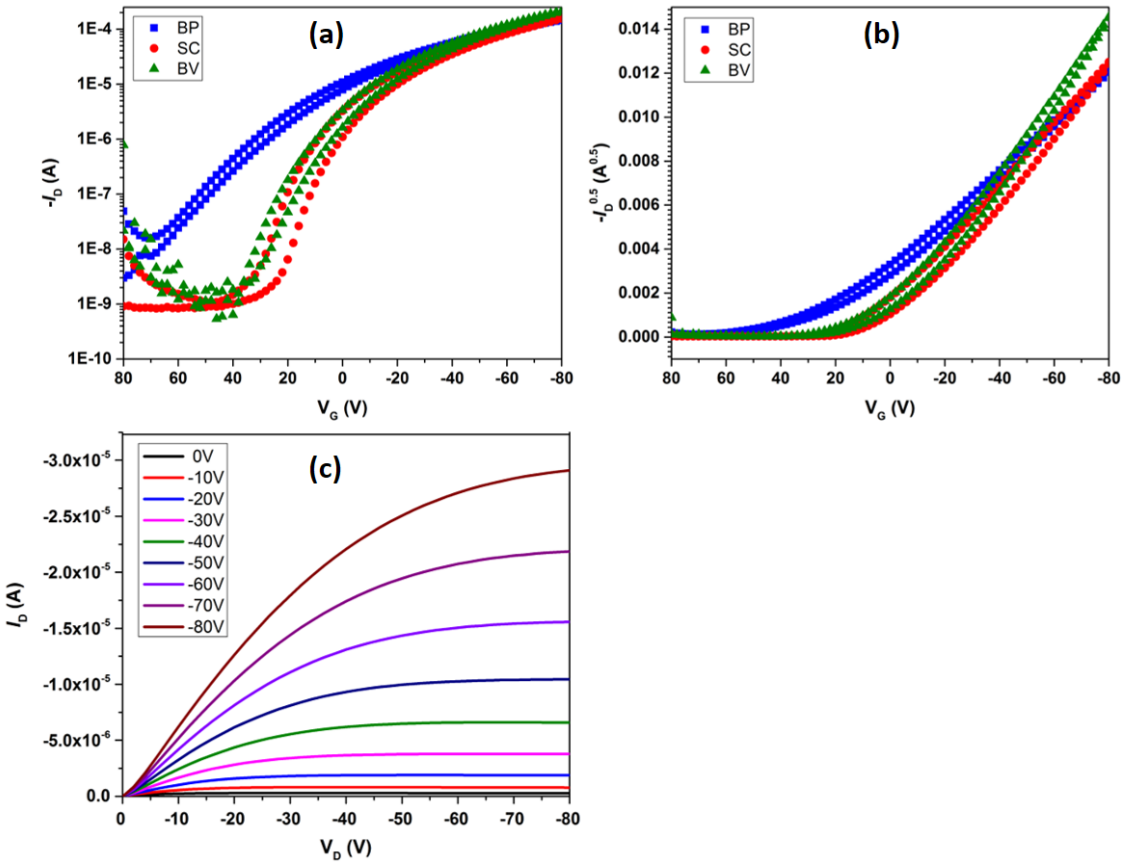

Figure 4.8 Representative I-V curves from OFET testing showing (a) drain current as a function of gate voltage, (b) the square root of drain current used to calculate slope for mobility, and (c) output curve at varying gate voltages for a representative vertically blade coated (BV) sample.

Figure 4.8 shows representative I-V curves obtained through OFET testing, while Table 4.1 displays average mobilities, on/off ratios and threshold voltages for OFETs tested.

Table 4.1 Average Mobility, On/Off Ratios and Threshold Voltages

Sample	Mobility ($cm^2V^{-1}s^{-1}$)	V_{th} (V)	On/Off Ratio
BP	0.062 ± 0.011	24.5 ± 6.7	$1.79 \times 10^4 \pm 1.08 \times 10^4$
SC	0.088 ± 0.003	17.8 ± 2.6	$1.09 \times 10^5 \pm 1.11 \times 10^4$
BV	0.124 ± 0.017	6.5 ± 3.4	$1.16 \times 10^5 \pm 5.63 \times 10^4$

Table 4.1 shows that with greater numbers of vertical P3HT nanofibers, not only does the mobility increase, but also the threshold voltage (V_{th}) decreases. The average threshold voltages decrease from 24.5 V (blade coated parallel) to 6.5 V (blade coated vertical), indicating an additional advantage of lower voltage required when the fibers are oriented in a specific direction using the blade coating technique.

4.3 Conclusions

These results show that P3HT can be aligned in a desired direction using a simple blade coating technique, provided the P3HT has been self-assembled into nanofibers by aging in solution beforehand. Dichroic ratios of 3 were obtained as measured by polarized UV-Vis absorption spectroscopy. Atomic Force Microscopy and Polarized Optical Microscopy confirm the desired orientation of P3HT fibers on both the scale of microns and millimeters.

The second conclusion is that while one might expect fibers oriented parallel to the OFET channel length to achieve the greatest mobility due to the prevalance of π stacking in the direction of the path from source to drain, these results show that the opposite is true, and are consistent with results recently obtained by Chu et al.[177] Maximizing the prevalence of the faster intrachain charge transport mechanism in the direction of the channel length

(with closely packed adjacent fibers providing for smooth transitions across fibers) provided for the highest charge carrier mobilities in this study. A 100% increase was observed compared to the case when most P3HT chains were oriented perpendicular (fibers oriented parallel) to the channel length.

This study sheds light on important principles at play when using alignment techniques to tune the charge transport in π-conjugated polymers that have the propensity to self-assemble into nanostructures. When unidirectionally aligning these nanostructures, the importance of intramolecular as well as intermolecular charge transport directions must be taken into account. In addition, the facile and less wasteful blade coating procedure shows an improvement in mobility and threshold voltage vs. spin coating (provided the blade coating is done in the appropriate direction), a promising development in the efforts towards roll-to-roll, large scale fabrication of high performance polymeric electronics for a range of applications.

4.4 Experimental Methods

Materials. Regioregular P3HT was purchased from Rieke Metals Inc. (catalog no. RMI-001EE, Regioregularity = 96% HT, Mw = 90 kDa, PDI = 2.3) and used without further purification. Chloroform (anhydrous) was purchased from Sigma-Aldrich and used without further purification. For POM studies, borosilicate glass capillaries of dimensions 0.1 × 1 × 50 mm were purchased from Vitrocom Inc. and used without any further surface treatment. Silicon wafers (n-doped) were purchased from Rogue Valley Microdevices Inc. with a thermally grown 300 nm thick SiO_2 dielectric for OFET fabrication.

Solution Processing of P3HT. A chloroform-P3HT solution (5 mg/mL) was prepared in a 20 mL borosilicate glass vial by heating to 70 °C for approximately 30 min until fully dissolved. The solution was then left to cool to room temperature. At room temperature (but still orange), a syringe was used to take up the solution and inject it back through an 18 guage needle before aging or sonication took place. Vials were capped and wrapped in parafilm and stored in a dark cabinet for aging. All solution processing was done in air.

Organic Field-Effect Transistor (OFET) Fabrication and Characterization. OFET devices with bottom-gate, bottom-contact geometry were fabricated to test the electrical properties of the P3HT films. Highly n-doped silicon wafers with a 300 nm SiO_2 dielectric layer were used as the substrate. The doped silicon was used as the gate electrode with the SiO_2 dielectric on top. Source and drain contacts were fabricated using a standard photolithography based lift-off process in a cleanroom, followed by E-beam evaporation of the Cr (3 nm) adhesion layer and the Au (50 nm) contacts. Prior to spincoating the processed P3HT solutions, the OFET substrates were cleaned by sonication in acetone for 10 minutes followed by rinsing with acetone, methanol and isopropanol, followed by cleaning in a UV-Ozone chamber (Novascan PSD-UV) for 15 min to remove organic contaminants. P3HT solutions were spincoated on the cleaned devices at 800 RPM for 30 s in air (WS-650MZ-23NPP, Laurell) or were blade coated according to parameters below in the "blade coating" section. Devices were patterned by removing excess P3HT from areas surrounding the channel, then left in a vacuum oven overnight at 50 °C to remove any residual solvent. The devices were tested in a nitrogen environment using an Agilent 4155C semiconductor parameter analyzer. The field-effect hole mobility was calculated under transistor operation (V_{DS} = -80 V; V_G = 80 to -80V) by plotting the square root of

the drain current (ID) vs gate voltage (V_G) and obtaining the slope to extract the mobility according to the following equation:[72]

$$I_D = \mu C_o \frac{W}{2L}(V_G - V_T)^2 \quad (13)$$

where W (2000 μm) and L (50 μm) are the transistor channel width and length, respectively, V_T is the threshold voltage, and C_o is the capacitance per unit are of the SiO2 gate dielectric (1.15×10^{-8} F cm^{-2}). For each solution condition, 4 devices were measured to obtain average mobility values.

UV-Vis Spectroscopy. An Agilent 8510 UV-vis spectrometer was used to measure absorption spectra on films (spincoated on pre-cleaned glass slides at 800 RPM for 30 s), and solutions (placing droplet between glass slide and cover slip and securing with clips.

Atomic Force Microscopy. AFM measurements were performed on the same devices used for OFET measurements, using a ICON Dimension scanning probe microscope (Bruker) in tapping mode with a silicon tip (NSC-14, MikroMasch).

Polarized Optical Microscopy. POM images were obtained using a Leica DMRX optical microscope equipped with a rotatable polarizer and analyzer and a rotatable stage. Images were captured using a Nikon D300 digital SLR camera.

Blade Coating. Glass or OFET substrates were cleaned in a UV-Ozone chamber prior to use. Using the aged P3HT solution, films were blade coated with a vertical razor blade attached to a motorized controlled stage at 10 mm/s using a 50 μm gap between the substrate and the blade, and a 5 microliter drop of solution at room temperature.

CHAPTER 5. CONCLUSIONS AND FUTURE WORK

5.1 Conclusions

In the quest for cost-effective, solution processable and high performing organic electronic devices such as solar cells, light-emitting diodes and transistors, the careful control and understanding of polymer semiconductor morphology and the impacts on charge transport are highly significant. Facilitating intra- and intermolecular ordering are important in enable high performing macro-electronics such as in large area displays. In this thesis, ordering in P3HT is investigated at both the micro-structural level and at the level of orientational ordering on macro scale, in both a fluid state and in the film state.

This work elucidates a mechanism for liquid crystalline behavior in P3HT solutions, showing that time-dependent self-assembly of P3HT into long nanofibers in solution allows for macroscopic alignment of these rod-like particles. Through a deeper exploration of the aggregation techniques available to induce nanofiber self-assembly, it was discovered that the length of the fibers is critical to being able to align them in fluid state and then retain that alignment in the film state. Specifically, ultrasonication, while inducing similar or greater levels of aggregation, does not produce long enough fibers to facilitate fiber alignment compared with aging. The combination of sonication followed by aging, however can yield high performance OFETs due to enhanced aggregation facilitated by larger number of nucleation sites for nanofiber growth.

In order to better understand the impact of long-range ordering of P3HT on OFET performance, it was necessary to use a film deposition method other than spin coating.

Blade coating, a facile, less wasteful and more appropriate technique to simulate roll-to-roll fabrication on a commercial scale. While flexible substrates such as PET should be used to further simulate the desired end-product and coating method, this was out of the scope of the current work – what this technique allowed was successful control of the alignment of P3HT nanofibers over large areas in the film state. This enabled the surprising observation that fibers oriented parallel to the OFET channel length did not produce the fastest mobility, despite this being the direction of π-π stacking within the fibers. Rather, the greater the number of fibers aligned perpendicular with respect to the channel length, the higher the resulting mobility. The proposed reasoning is that in this configuration, intramolecular charge transport, being much faster than intermolecular hopping, is facilitated to a greater extent in the path between electrodes, and that the high degree of inter-fiber alignment facilitates a significant number of tie-chains and more efficient hopping between fibers. The insights gained here highlight the role of both short and long range ordering in fine-tuning charge transport in polymeric semiconductors, especially those systems in which self-assembly into nanostructures occurs. These principles can be used on the road to the further development of reproducible, cost-effective, high-performance organic electronics applications.

5.2 Future Work

Recommendations for future work include translating these insights into work on devices with different geometries such as solar cells, molecular weight studies to investigate how chain length may affect the ability to form tie chains and facilitate charge transport anisotropy, and temperature-dependence experiments on OFETs to determine the relative contributions of the modes of charge transport in aligned P3HT films.

Perovskite solar cells have seen an unprecedented, rapid rise in efficiencies in recent times.[178] While P3HT has been investigated as a hole transport layer in perovskite solar cells,[179] the impact of tuning P3HT morphology on vertical hole mobility and overall solar cell performance has been relatively unexplored. Applying the insights gained in this thesis towads depositing P3HT nanofibrillar films with long range ordering as hole transport layers could yield broader insights into their applications towards other types of organic electronic devices. In theory, the enhanced intrachain charge transport could be facilitated in the out-of plane direction as a result of well ordered, connected P3HT nanofibers. The expected result would be enhanced hole mobility in the out-of-plane direction compared with the case of pristine P3HT (Figure 5.1).

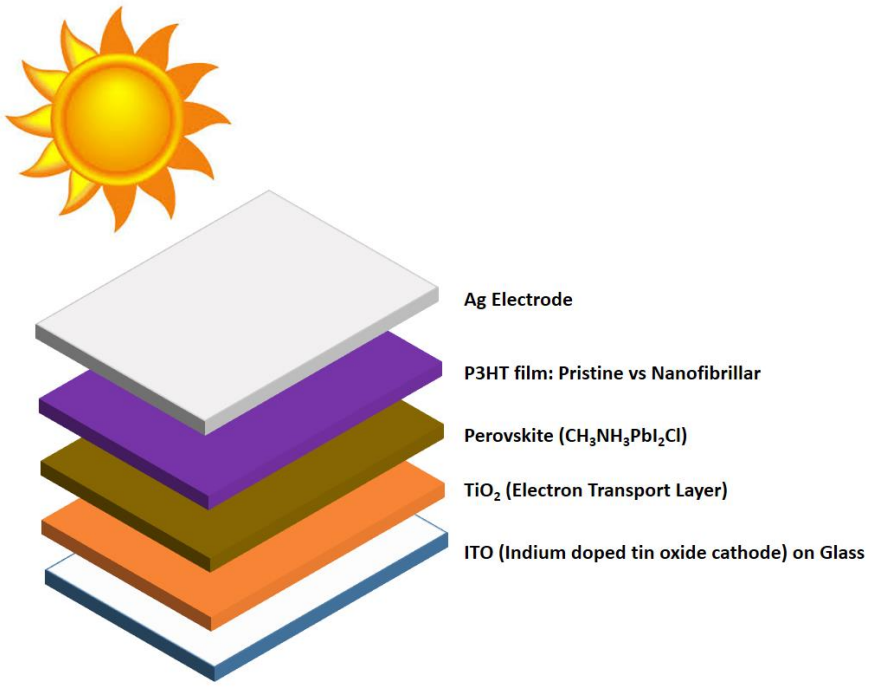

Figure 5.1 Proposed P3HT hole transport layer in perovskite solar cells

A second area of future work could involve utilizing P3HT of varying molecular weights to conduct a study on the effect of molecular weight on charge transport anisotropy. The mechanism we proposed for the faster hole mobility when the fibers were oriented perpendicular to the OFET channel length depends on the idea that these fibers are well-connected with tie-chains, making the numerous grain boundaries between fibers less of a barrier than they normally would have been. Relatively high molecular weight P3HT was used for this study (M_w = 90 kDa, PDI = 2.3). To test this hypothesis, P3HT with lower molecular weight could be used which would allow for shorter possible tie-chains extending out of fibers and prevent the fibers from being well connected. Perhaps in this case, there would be no charge transport anisotropy, or perhaps the charge transport in the opposite direction would be fastest, where at least the π-π stacking directions within fibers are oriented parallel to the channel length. It is also conceivable that the use of very

higher molecular weights would yield even greater charge transport anisotropy than we observed. One would have to be judicious in choice of molecular weights to ensure that self-assembly into long fibers is still possible and can facilitate the long range ordering of those fibers when blade coated.

Thirdly, a temperature dependence study could be performed in order to further probe the intramolecular and intermolecular contributions to the anisotropic transport that occurs in well-ordered P3HT nanofiber films. As discussed in 1.2.2, with increasing temperatures, the thermally activated hopping rate increase would result in higher mobilities. In the case of the band regime, the mobility would decrease with increasing temperature, but the band regime is not expected for such a system in which hopping still plays such a significant role due to the inherent disorder. However, in the perpendicular nanofiber orientation in which we hypothesized that intramolecular charge transport in P3HT plays a more significant role, the increase in mobility with temperature may be smaller due to the increased amplitude of molecular vibrations. By plotting the mobility as a function of (1/T), the activation energy could be calculated from the slope, based on the Arrhenius relationship:[180]

$$\mu \propto \exp\left(-\frac{E_a}{k_B T}\right) \tag{14}$$

where μ the mobility, E_a is the eactivation energy, k_b is Boltzmann's constant, and T is temperature. In the case of fibers oriented parallel to OFET channel length (π-π stacking direction within a fiber pointing from source to drain electrode), the mobility should

increase significantly with increasing temperature (up to a point where melting begins to occur). If the mechanism we proposed for the apparent charge transport anisotropy is correct, then in the opposite case where fibers are perpendicular to the OFET channel length and intramolecular charge transport plays a greater role, the activation energy may be lower due to the reduced temperature dependence.

APPENDIX A. SUPPORTING INFORMATION

A.1 Chapter 2 Supporting Information

POM Intensity vs. Capillary Angle for 3-day Aged 5mg/mL P3HT/TCB Solution

ImageJ analysis software[181] was used to quantify the intensity of transmitted light as a function of rotation angle **(**Figure A - 1**)**. The plot of capillary rotation angle vs. intensity resembles the (1-cos(4ϕ)) dependence of intensity on the rotation angle (ϕ) of the optic axis with respect to the polarizer direction as predicted by equation 8[104] for an ordered material.

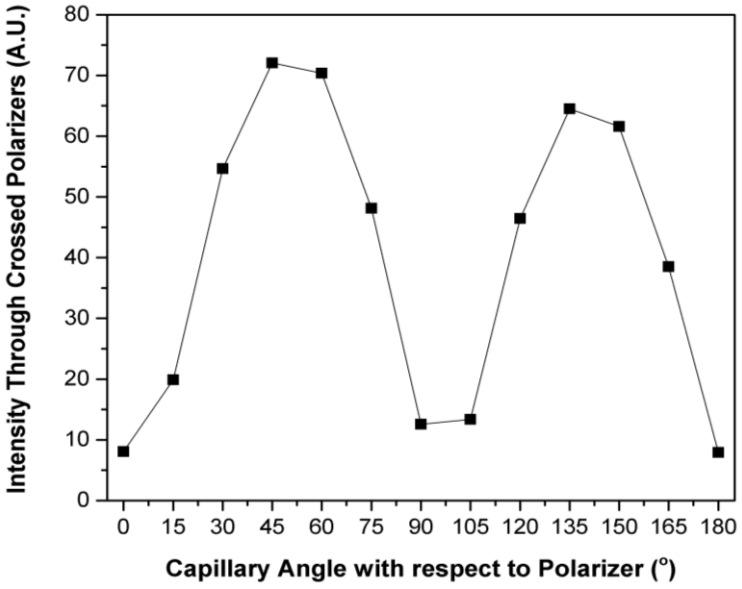

Figure A - 1 Intensity of light transmitted through crossed polarizers as a function of angle of capillary with respect to polarizer for a 5mg/mL P3HT solution aged for 3 days before filling into capillary (intensity obtained using ImageJ software).[181]

Calculations of Percent Aggregates using UV-Vis Spectra

	Area	Fraction (%)
Amorphous	0.72475	94.84
Aggregate	0.05481	5.16

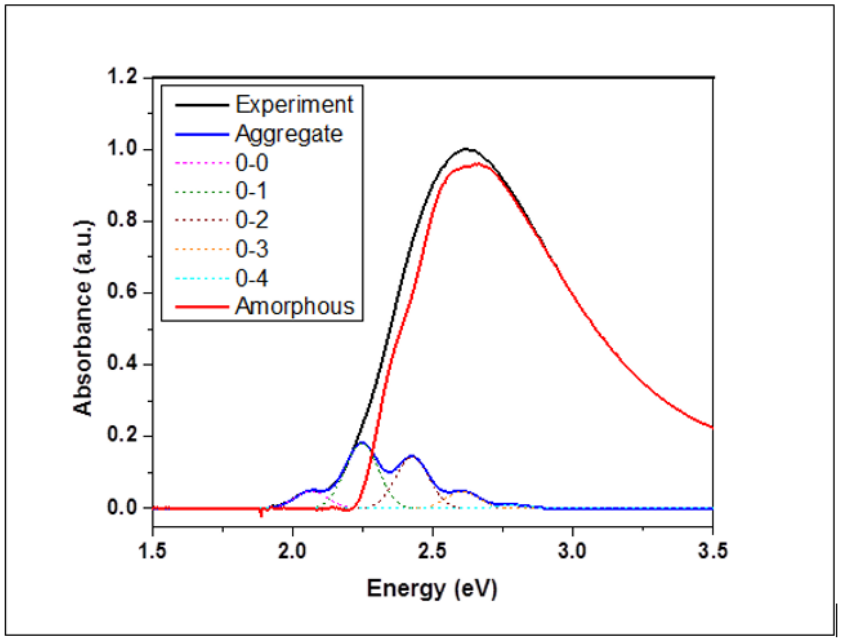

Figure A - 2 Example of Franck-Condon fitting of UV-Vis absorption spectra using (equation A1) for obtaining aggregate and amorphous fraction in P3HT / TCB solution, using methods described in literature.[106,107]

$$A(E) \propto \sum_{m=0} \left(\frac{S^m}{m!}\right)\left(1 - \frac{We^{-S}}{2E_p}\sum_{n\neq m}\frac{S^n}{n!\,n-m}\right)^2 \exp\left(\frac{\left(E - E_{0-0} - mE_p - \frac{1}{2}WS^m e^{-S}\right)^2}{2\sigma^2}\right) \quad \text{(A1)}$$

In this modified Franck-Condon fitting equation, A is the absorbance as a function of the photon energy (E), W is the free exciton bandwidth of the aggregates, S is the Huang-Rhys factor and fixed at a value of 1.0 taken from a Franck-Condon fit, m and n are differing vibrational levels, $E_{0\text{-}0}$ is the 0–0 transition energy, E_p is the intermolecular vibrational energy and taken as 0.18 eV, and σ is the Gaussian linewidth. The fit generates the blue

line which represents the aggregates. Subtracting the blue (aggregate) curve from the black experimental curve gives the amorphous fraction (red curve). These fractions are used to calculate the percent aggregates.

Paremeters:

M=5
N=10
S=1
E_p=0.18

Birefringence in solutions confined to capillaries over time

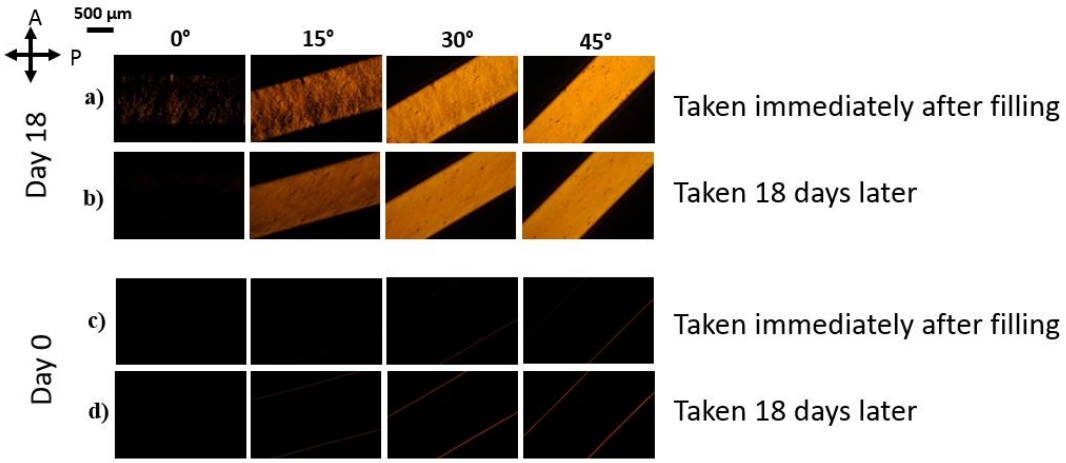

Figure A - 3 POM of capillary filled on day 18 of stock solution aging, as observed (a) immediately after filling capillary, and (b) 18 days after filling the capillary, and POM of capillary filled on day 0, as observed (c) immediately after filling and (d) 18 days after filling.

Expanded P3HT/TCB Raman Spectrum and Order Parameter Data

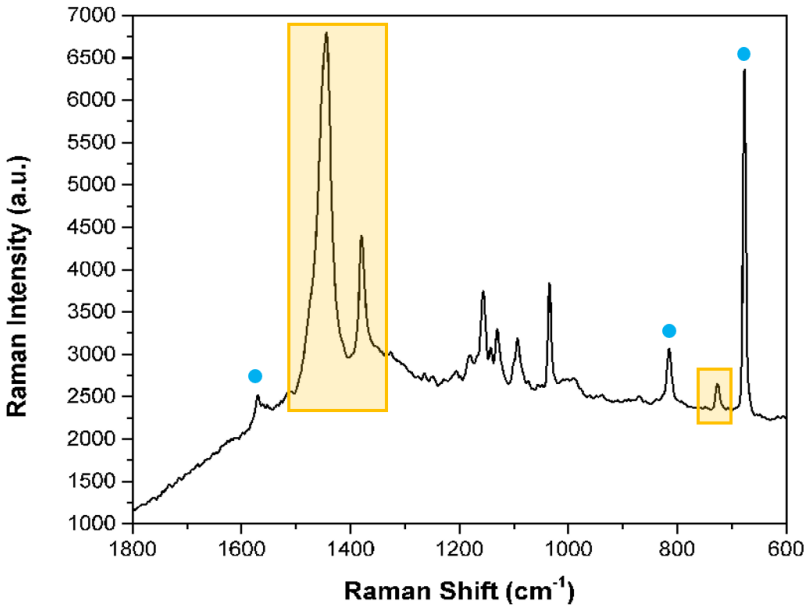

Figure A - 4 Raman spectrum of P3HT / TCB solution in capillary tube with long axis at an angle 0° with respect to incident polarization (parallel), taken with parallel polarizers. Peaks highlighted in orange are attributed to pure P3HT while peaks with a blue dot are attributed to TCB.[103]

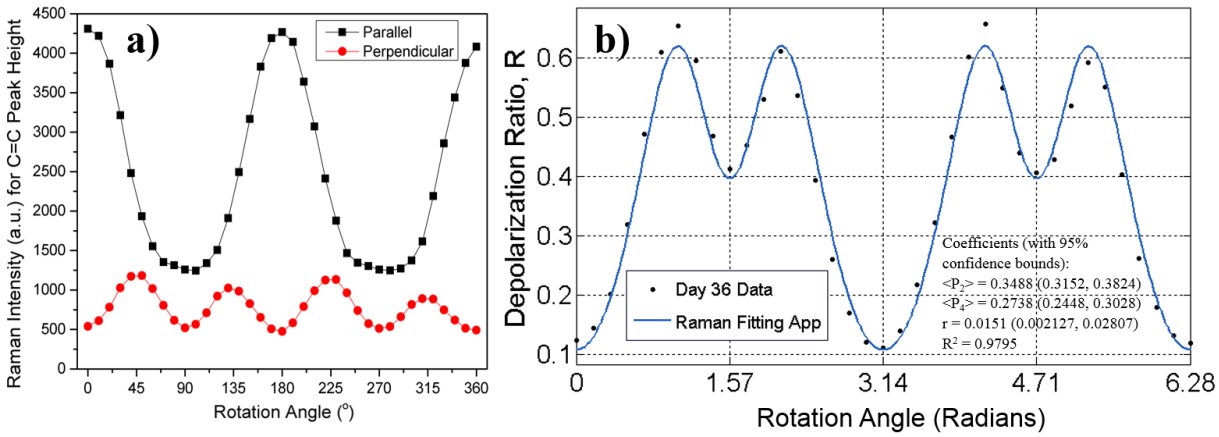

Figure A - 5 (a) Example of Raman scattered light intensity of C=C stretch peak as a function of rotation angle of capillary tube. Rotation angle of 0° corresponds to long axis of capillary perpendicular to fixed analyzer for both polarized (parallel) and depolarized (perpendicular) geometries. Capillary filled with 36-day aged P3HT/TCB solution. (b) Corresponding depolarization ratio, R = $\frac{I_{\perp}(\theta)}{I_{\parallel}(\theta)}$, (with θ in radians), fit to equation 9 to obtain P_2 and P_4 order parameters as described in literature.[116]

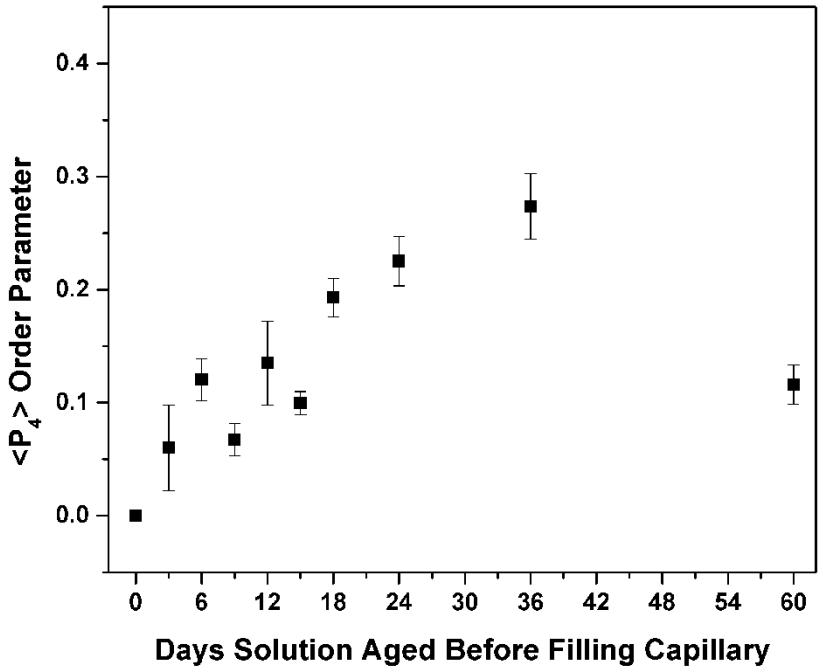

Figure A - 6 <P_4> Order parameter for P3HT / TCB solutions in capillary tube as a function of solution aging time before filling capillary.

Depolarized Dynamic Light Scattering Details:

The DDLS method measures the effect of partial depolarization of incident light scattered by anisotropic entities suspended in a liquid.[121] The time dependence of the light scattering intensity is recorded using two geometries: Vv (detector vertical, incident light vertical) and Hv (detector horizontal, incident light vertical). The detected signal gives the electric field autocorrelation function $g^{(1)}(t)$:[132]

$$g^{(1)}(t) = exp(-\Gamma t) \quad \text{(A2)}$$

where Γ is the decay rate. The $g^{(1)}(t)$ mathematical construct, is converted into an intensity autocorrelation function through the Siegert relationship:[182]

$$g^{(2)}(t) = 1 + f|g^{(1)}(t)|^2 \quad \text{(A3)}$$

In this expression *f* is an instrumental parameter, 0<f<1, related to spatial coherence, dark count and solvent scatter. From the decay rate of the autocorrelation function, the translational and rotational diffusion coefficients can be extracted:

$$\Gamma_{Vv} = D_T q^2 \quad \text{(A4)}$$

$$\Gamma_{Hv} = D_T q^2 + 6D_R \quad \text{(A5)}$$

where D_T is the translational diffusion, q is the scattering vector magnitude ($q = 4\pi n \sin(\theta/2)/\lambda_0$, n-is the solvent refractive index, θ is the scattering angle and λ_0 is the incident light wavelength *in vacuo*) and D_R is end-over-end rotational diffusion coefficient. For a non-spherical, rodlike object the diffusion coefficients give information about the axial ratio L/d:[183]

$$D_R = \frac{3k_B T ln(L/d)}{\pi \eta L^3} \quad \text{(A6)}$$

$$D_T = \frac{k_B T ln(L/d)}{3\pi\eta L} \quad \text{(A7)}$$

In this expression k_B is the Boltzmann constant, T is the absolute temperature, L is taken as the length and d as the diameter of the scattering rodlike object.

Another concept used, especially in depolarized static light scattering experiments, is the depolarization ratio ρ_v,[122,123] that is related to excess Rayleigh scattering. The excess of scattering is due to optical anisotropy of anisotropic entities.[123]

$$\rho_v = \frac{I_{Hv}}{I_{Vv}} \quad \text{(A8)}$$

where the v subscript means that the incident light is vertically polarized. I_{Hv} and I_{Vv} are the intensities of the horizontal and vertical polarizations of scattered light recorded by detector.

A.2 Chapter 3 Supporting Information

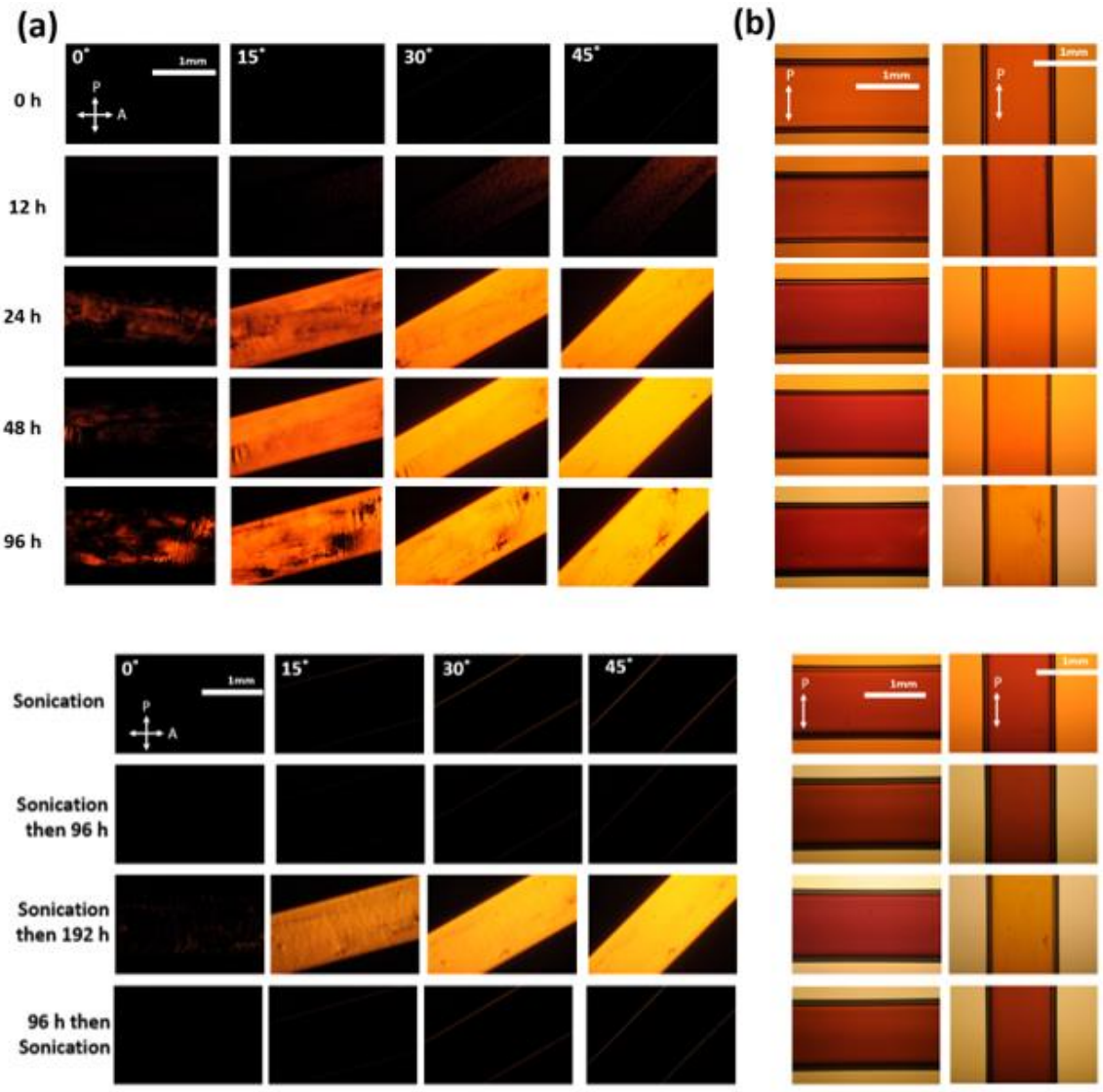

Figure A - 7 (A) Polarized Optical Microscopy (POM) images of capillaries filled with 5 mg/mL P3HT/Chloroform solutions processed as indicated, before filling. Angles refer to angle between long axis of capillary and analyzer. (B) Images taken with only one polarizer, showing linear dichroism as capillary is oriented parallel or perpendicular to polarizer. This change in absorbance suggests chains are perpendicular to capillary long-axis and fibers are parallel to capillary long-axis.[139] **All scale bars are 1mm.**

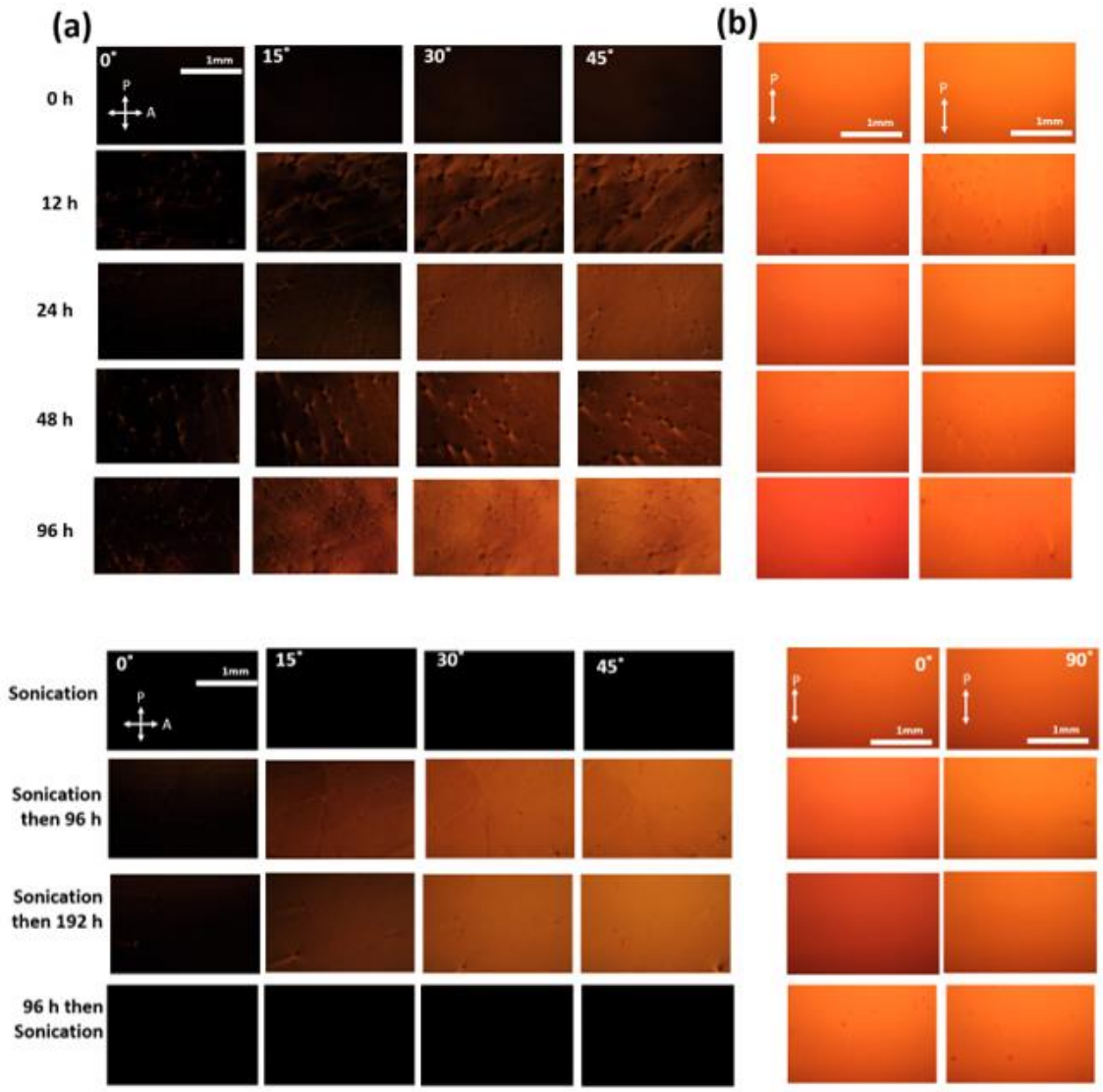

Figure A - 8 (A) Polarized Optical Microscopy (POM) images of films spin coated from 5 mg/mL P3HT/Chloroform solutions processed as indicated. Angles refer to angle of stage as it rotates away from analyzer. (B) Images taken with only one polarizer, showing linear dichroism as film is rotated. All scale bars are 1mm.

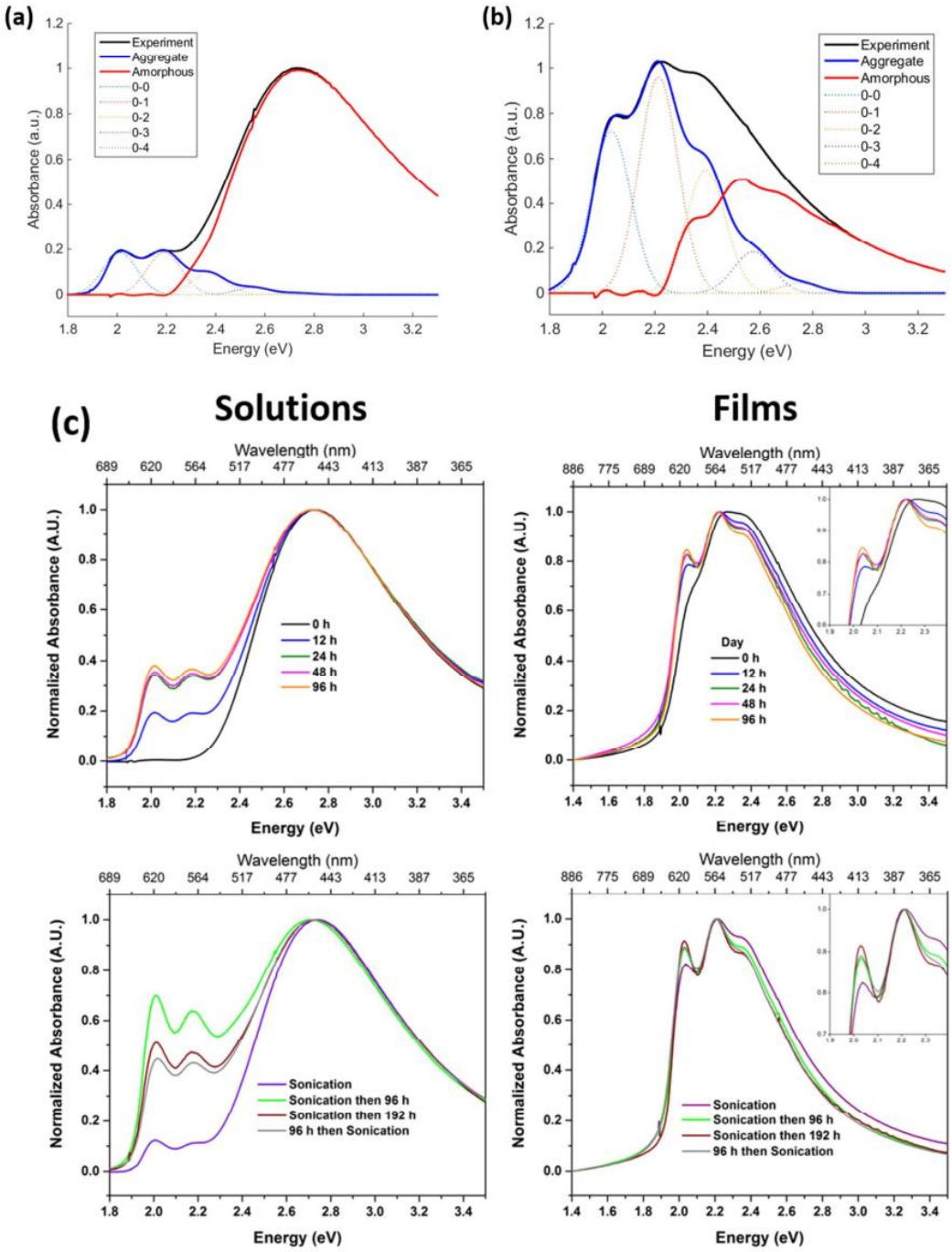

Figure A - 9 (A) Example of Franck-Condon fitting of normalized UV-Vis absorption spectra for obtaining percent aggregates and 0-0 and 0-1 peak intensities for exciton bandwidth calculation in P3HT / Chloroform solution (a) and film (b) after 12 hours of aging, using methods described in literature:[142] (c) UV-vis curves for all samples.

Fits in Figure A - 9a,b were made using equation A1, with parameters:

M=5
N=10
S=1
Ep=0.18

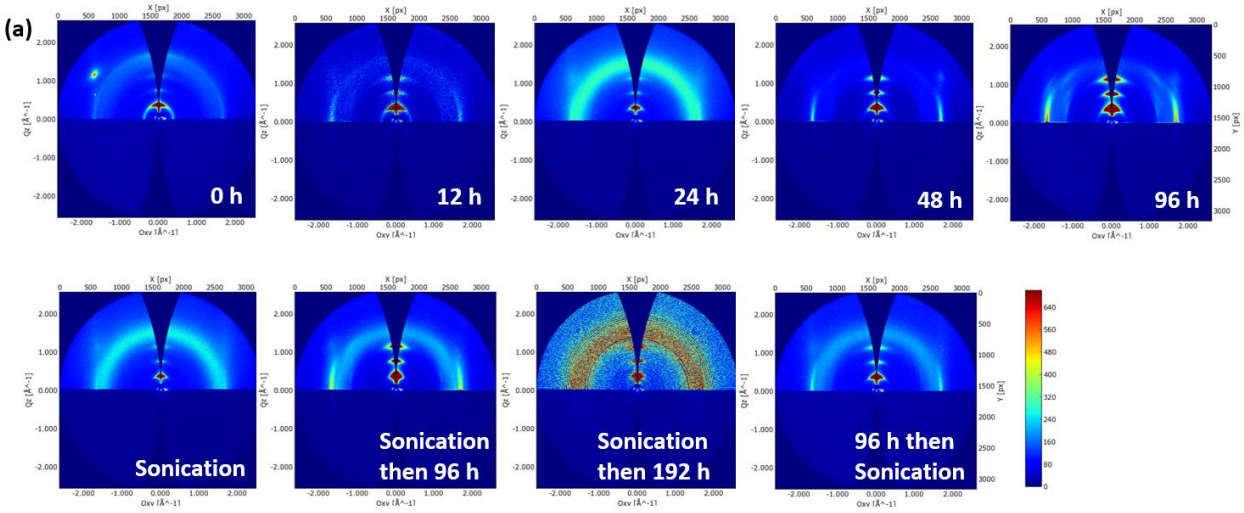

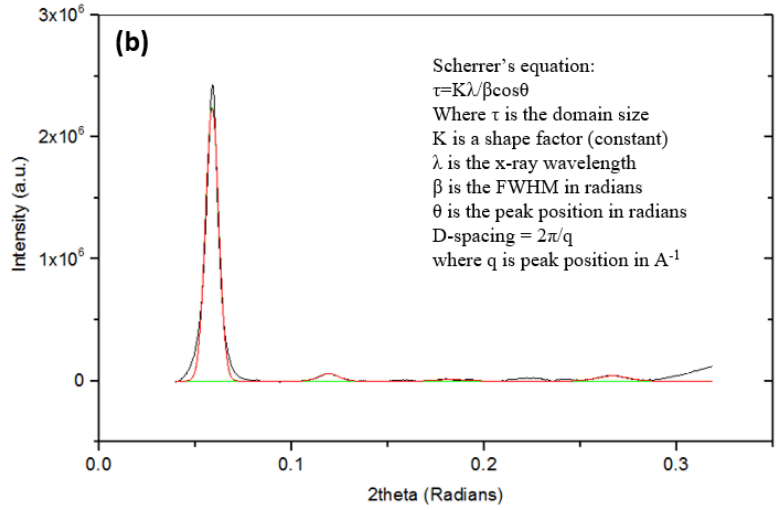

Fitting Results

Peak Index	Peak Type	Area Intg	FWHM	Max Height	Center Grvty	Area IntgP
1	Gaussian	19295.55304	0.00808	2.24232E6	0.05876	91.38982
2	Gaussian	754.45696	0.01167	60722.69696	0.11935	3.57335
3	Gaussian	228.65783	0.01755	12241.50051	0.18358	1.083
4	Gaussian	834.79176	0.01881	41686.87363	0.26662	3.95384

Figure A - 10 (A) All 2-D GIWAXS diffraction patterns. Note: Sonication then 192 h sample has lower signal to noise ratio, possibly due to an abnormally thin region of film that was exposed or an errant shorter beam time exposure. (B) Sample plot of 2-D images reduced to 1-D plots via integration of cake segments and analyzed using Origin Pro software for peak fitting.

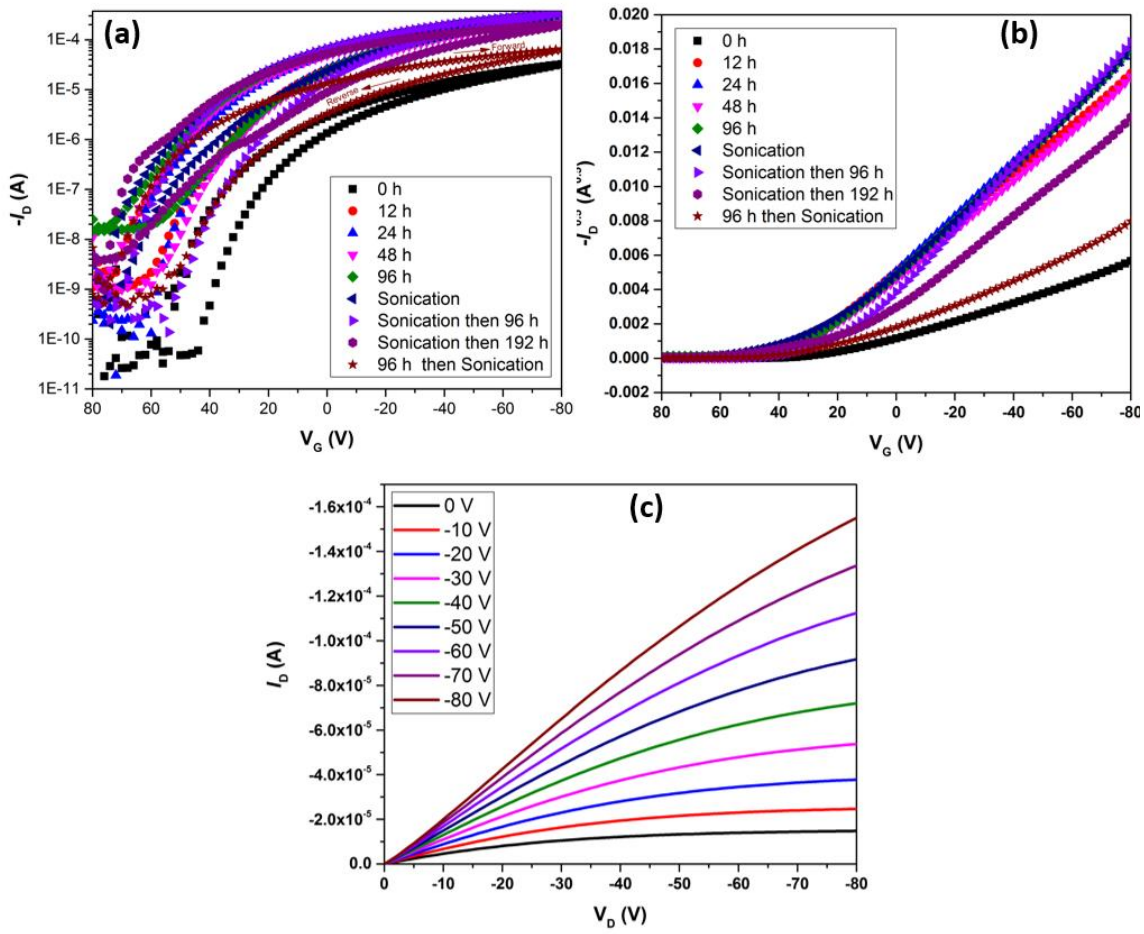

Figure A - 11 (a) Transfer characteristics of representative P3HT OFET devices (V_D = -80 V) swept in both forward (80 to -80 V) and backward (-80 to 80 V) directions. (b) Square root of drain current plotted vs V_G in backward direction, used to calculate slope for mobility. (c) Output characteristics of a Sonicated then 96 h aged sample.

Table A - 1 Threshold Voltages and On/Off Ratios

	V_T	V_T Standard Deviation	On/Off Ratio	On/Off Ratio Standard Deviation
0 h	2.20E+01	2.34E+00	6.67E+06	1.00E+07
12 h	3.16E+01	2.82E+00	2.10E+05	2.41E+05
24 h	2.75E+01	2.08E+00	6.78E+06	7.82E+06
48 h	3.13E+01	8.76E-01	1.04E+05	8.45E+04
96 h	3.33E+01	2.56E+00	3.99E+04	1.53E+04
Sonication	2.69E+01	1.83E+00	1.95E+05	1.43E+05
Sonication then 96 h	2.48E+01	2.97E+00	3.84E+06	3.74E+06
Sonication then 192 h	2.76E+01	8.47E-01	1.16E+05	1.01E+05
96 h then Sonication	2.29E+01	4.36E-03	2.86E+05	2.26E+05

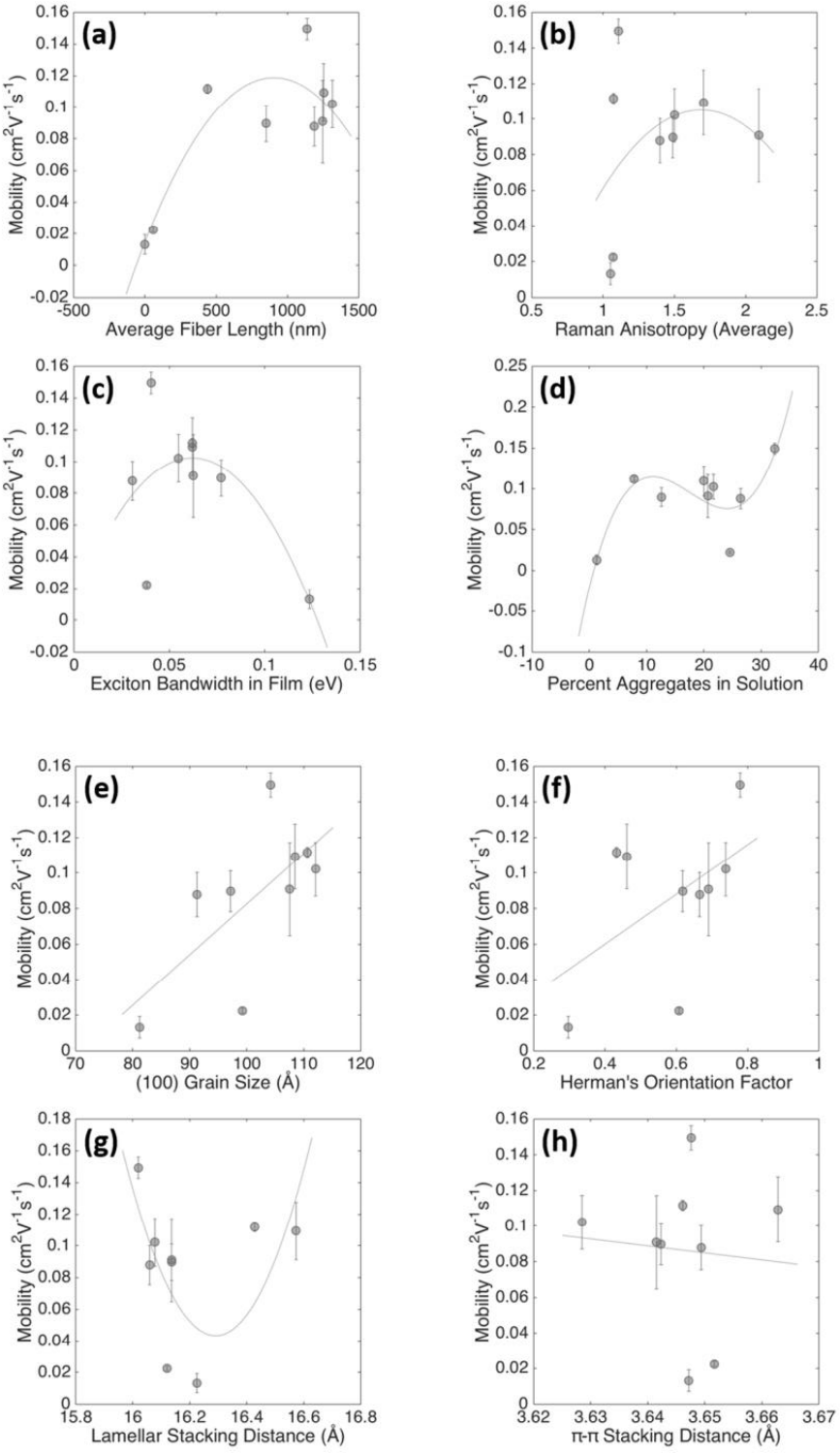

Figure A - 12 Mobility as a function of (a) average fiber length, (b) Raman anisotropy, (c) film exciton bandwidth, (d) percent aggregates in solution, (e) (100) grain size, (f) Herman's Orientation Factor, (g) lamellar stacking distance, and (h) π-π stacking distance.

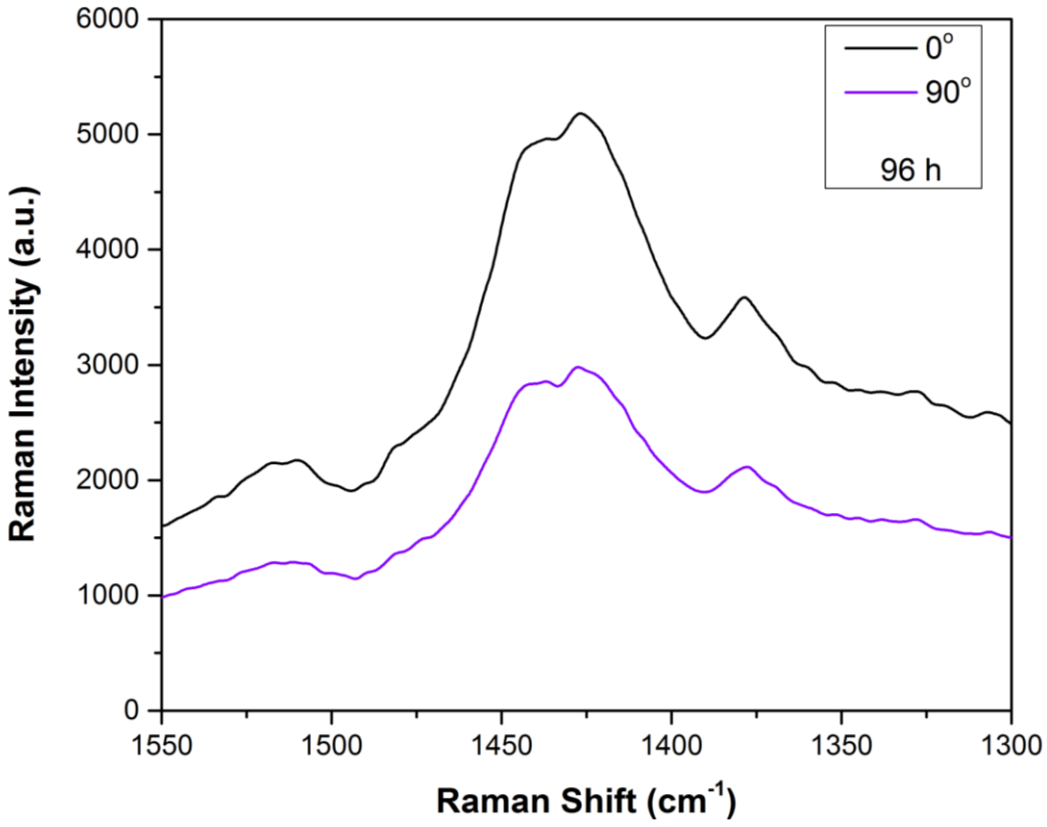

Figure A - 13 Example of Raman spectra obtained from P3HT film spin coated from solution aged 96 h. Region of interest is C=C double bond stretch: peaks fit from 1495 to 1390 cm^{-1} with Lorentzian curves to obtain peak height and compare for highest peak vs when sample was rotated by a further 90˚.

A.3 Chapter 4 Supporting Information

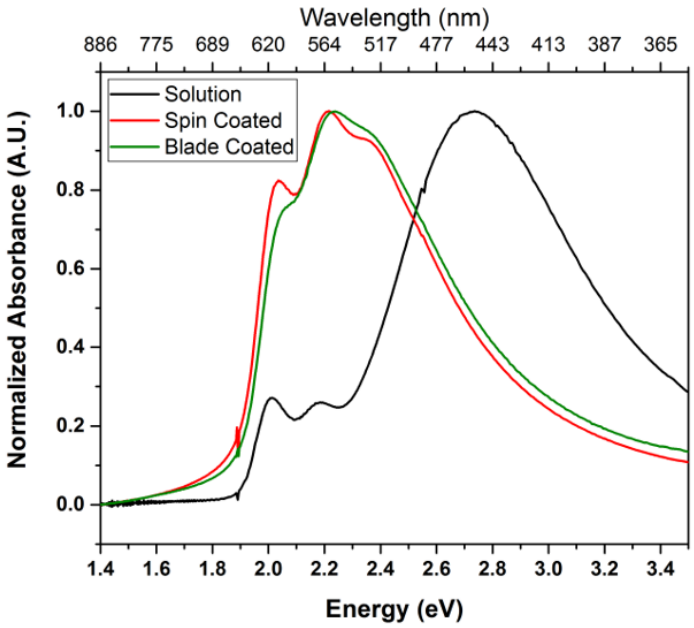

Figure A - 14 UV-Vis spectra for 96 hr aged P3HT/$CHCl_3$ 5mg/mL solution and for films blade coated and spin coated from this solution.

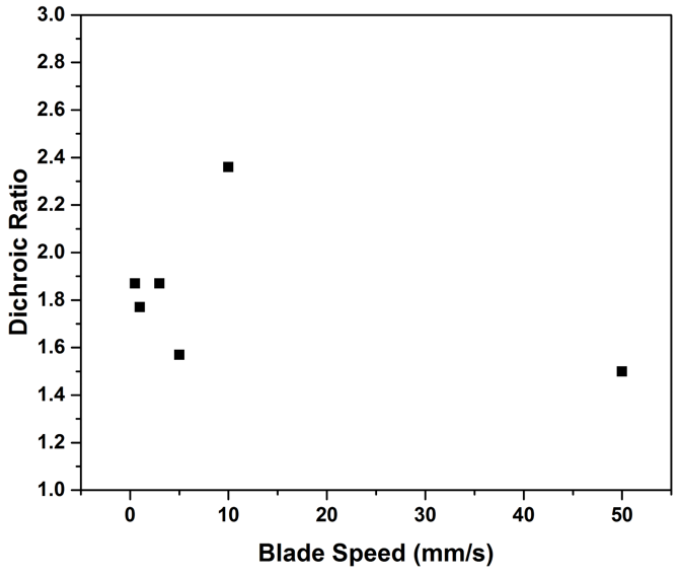

Figure A - 15 Dichroic ratio as a function of blade coating speed for 96 hr aged P3HT/$CHCl_3$ 5mg/mL solution. The 10mm/s speed was chosen as it gave the highest dichroic ratio.

REFERENCES

(1) Bao, Z.; Locklin, J. J. *Organic Field-Effect Transistors*; CRC Press, 2007.

(2) Tang, C. W. Two-Layer Organic Photovoltaic Cell. *Appl. Phys. Lett.* **1986**, *48* (2), 183.

(3) Li, G.; Zhu, R.; Yang, Y. Polymer Solar Cells. *Nat. Photonics* **2012**, *6* (3), 153–161.

(4) Burroughes, J. H.; Bradley, D. D. C.; Brown, A. R.; Marks, R. N.; Mackay, K.; Friend, R. H.; Burns, P. L.; Holmes, A. B. Light-Emitting Diodes Based on Conjugated Polymers. *Nature* **1990**, *347* (6293), 539–541.

(5) Kamtekar, K. T.; Monkman, A. P.; Bryce, M. R. Recent Advances in White Organic Light-Emitting Materials and Devices (WOLEDs). *Adv. Mater.* **2010**, *22* (5), 572–582.

(6) Koezuka, H.; Tsumura, A.; Ando, T. Field-Effect Transistor with Polythiophene Thin Film. *Synth. Met.* **1987**, *18* (1), 699–704.

(7) Braga, D.; Horowitz, G. High-Performance Organic Field-Effect Transistors. *Adv. Mater.* **2009**, *21* (14–15), 1473–1486.

(8) Exposolar.org. DailyTech - Measuring Purity, Size of Organic Solar Cells Ups Efficiency 42 Percent http://www.dailytech.com/Measuring+Purity+Size+of+Organic+Solar+Cells+Ups+Efficiency+42+Percent/article29592.htm.

(9) OLED Lighting Trends and Energy Efficiency | eCubed Ventures http://www.ecubedventures.com/oled-lighting-trends-and-energy-efficiency/.

(10) Organic Field-Effect Transistor (OFET) | Chihaya Adachi lab http://www.cstf.kyushu-u.ac.jp/~adachilab/lab/?page_id=3898.

(11) Kearns, D.; Calvin, M. Photovoltaic Effect and Photoconductivity in Organic Laminated Systems. *J. Chem. Phys.* **1958**, *29*, 950–951.

(12) Bernanose, A. Electroluminescence of Organic Compounds. *Br. J. Appl. Phys.* **1955**, *6* (S4), S54–S55.

(13) Ferraris, J.; Cowan, D. O.; Walatka, V.; Perlstein, J. H. Electron Transfer in a New Highly Conducting Donor-Acceptor Complex. *J. Am. Chem. Soc.* **1973**, *95* (3), 948–949.

(14) Batail, P. Introduction: Molecular Conductors. *Chem. Rev.* **2004**, *104* (11), 4887–4890.

(15) Walatka, V. V.; Labes, M. M.; Perlstein, J. H. Polysulfur Nitride—a One-Dimensional Chain with a Metallic Ground State. *Phys. Rev. Lett.* **1973**, *31* (18), 1139–1142.

(16) Greene, R. L.; Street, G. B.; Suter, L. J. Superconductivity in Polysulfur Nitride (SN)X. *Phys. Rev. Lett.* **1975**, *34* (10), 577–579.

(17) Shirakawa, H.; Louis, E. J.; MacDiarmid, A. G.; Chiang, C. K.; Heeger, A. J. Synthesis of Electrically Conducting Organic Polymers: Halogen Derivatives of Polyacetylene, (CH) X. *J. Chem. Soc. Chem. Commun.* **1977**, No. 16, 578.

(18) Shacklette, L. W.; Chance, R. R.; Ivory, D. M.; Miller, G. G.; Baughman, R. H. Electrical and Optical Properties of Highly Conducting Charge-Transfer Complexes of Poly(p-Phenylene). *Synth. Met.* **1980**, *1* (3), 307–320.

(19) John Rabolt, B. F.; Clarke, T. C.; Keiji Kanazawa, K.; Reynolds, J. R.; Street, B. Organic Metals : Poly-(P-Phenylene Sulphide) Hexafluoroarsenate. *J.C.S. CHEM. COMM* **1980**, No. 8, 347–348.

(20) Keiji Kanazawa, K.; Diaz, A. F.; Gill, W. D.; Grant, P. M.; Street, G. B.; Piero Gardini, G.; Kwak, J. F. Polypyrrole: An Electrochemically Synthesized Conducting Organic Polymer. *Synth. Met.* **1980**, *1* (3), 329–336.

(21) Kaneto, K.; Hayashi, S.; Ura, S.; Yoshino, K. ESR and Transport Studies in Electrochemically Doped Polythiophene Film. *J. Phys. Soc. Japan* **1985**, *54* (3), 1146–1153.

(22) Chiang, J.-C.; MacDiarmid, A. G. “Polyaniline”: Protonic Acid Doping of the Emeraldine Form to the Metallic Regime. *Synth. Met.* **1986**, *13* (1), 193–205.

(23) Sato, M.; Tanaka, S.; Kaeriyama, K. Soluble Conducting Polythiophenes. *J. Chem. Soc. Chem. Commun.* **1986**, No. 11, 873.

(24) Elsenbaumer, R. L.; Jen, K. Y.; Miller, G. G.; Shacklette, L. W. Processible, Environmentally Stable, Highly Conductive Forms of Polythiophene. *Synth. Met.* **1987**, *18* (1), 277–282.

(25) Kahng, D.; Atalla, M. M. Silicon-Silicon Dioxide Field Induced Surface Devices. In *IRE Solid-State Device Research Conference*; 1960.

(26) Garnier, F.; Horowitz, G.; Peng, X.; Fichou, D. An All-Organic “soft” thin Film Transistor with Very High Carrier Mobility. *Adv. Mater.* **1990**, *2* (12), 592–594.

(27) Sariciftci, N. S.; Smilowitz, L.; Heeger, A. J.; Wudl, F. Photoinduced Electron Transfer from a Conducting Polymer to Buckminsterfullerene. *Science (80-.).* **1992**, *258* (5087).

(28) Morita, S.; Zakhidov, A. A.; Yoshino, K. Doping Effect of Buckminsterfullerene in Conducting Polymer: Change of Absorption Spectrum and Quenching of Luminescene. *Solid State Commun.* **1992**, *82* (4), 249–252.

(29) Embracing the Organics World. *Nat. Mater.* **2013**, *12* (7), 591–591.

(30) The Nobel Prize in Chemistry 2000 https://www.nobelprize.org/nobel_prizes/chemistry/laureates/2000/.

(31) Holliday, S.; Donaghey, J. E.; McCulloch, I. Advances in Charge Carrier Mobilities of Semiconducting Polymers Used in Organic Transistors. *Chem. Mater.* **2014**, *26* (1), 647–663.

(32) Bittle, E. G.; Basham, J. I.; Jackson, T. N.; Jurchescu, O. D.; Gundlach, D. J. Mobility Overestimation due to Gated Contacts in Organic Field-Effect Transistors. *Nat. Commun.* **2016**, *7*, 10908.

(33) Noriega, R.; Rivnay, J.; Vandewal, K.; Koch, F. P. V.; Stingelin, N.; Smith, P.;

Toney, M. F.; Salleo, A. A General Relationship between Disorder, Aggregation and Charge Transport in Conjugated Polymers. *Nat. Mater.* **2013**, *12* (11), 1038–1044.

(34) Anthony, J. E. Organic Electronics: Addressing Challenges. *Nat. Mater.* **2014**, *13* (8), 773–775.

(35) Coropceanu, V.; Cornil, J.; da Silva Filho, D. A.; Olivier, Y.; Silbey, R.; Brédas, J.-L. J.-L. Charge Transport in Organic Semiconductors. *Chem. Rev.* **2007**, *107* (4), 926–952.

(36) Heeger, A. J. Semiconducting and Metallic Polymers: The Fourth Generation of Polymeric Materials. *Nobel Lect.* **2000**.

(37) Greenham, N. C.; Friend, R. H. Semiconductor Device Physics of Conjugated Polymers. *Solid State Phys.* **1996**, *49*, 1–149.

(38) LMOM. Electron Delocalization in Small Organic Molecules and Polymers http://lmom.epfl.ch/courses/class_organic_electronic_materials_2.pdf (accessed Sep 7, 2016).

(39) Brédas, J.-L.; Marder, S. R.; André, J.-M. An Introduction to the Electronic Structure of π -Conjugated Molecules and Polymers, and to the Concept of Electronic Bands. In *The WSPC Reference on Organic Electronics: Organic Semiconductors, Volume 1*; 2016; pp 1–18.

(40) Peierls, R. E. *Quantum Theory of Solids*; Oxford: Clarendon Press, 1955.

(41) Clean Energy Wiki. The Polyene Series - CleanEnergyWIKI http://photonicswiki.org/index.php?title=The_Polyene_Series.

(42) Brédas, J.-L.; Beljonne, D.; Coropceanu, V.; Cornil, J. Charge-Transfer and Energy-Transfer Processes in π-Conjugated Oligomers and Polymers: A Molecular Picture. *Chem. Rev.* **2004**, *104* (11), 4971–5004.

(43) Brédas, J. L.; Calbert, J. P.; Da, D. A.; Filho, S.; Cornil, J.; Heeger, A. J. Organic Semiconductors: A Theoretical Characterization of the Basic Parameters Governing Charge Transport. *Proc. Natl. Acad. Sci. U. S. A.* **2002**, *99* (9).

(44) Haddon, R. C.; Siegrist, T.; Fleming, R. M.; Bridenbaugh, P. M.; Laudise, R. A. Band Structures of Organic Thin-Film Transistor Materials. *J. Mater. Chem.* **1995**, *5* (10), 1719.

(45) Prins, P.; Grozema, F. C.; Schins, J. M.; Patil, S.; Scherf, U.; Siebbeles, L. D. A. High Intra-Chain Hole Mobility on Molecular Wires of Ladder Type Poly(p-Phenylenes); Bao, Z., Gundlach, D. J., Eds.; International Society for Optics and Photonics, 2006; p 63360Q.

(46) Dubin, F.; Melet, R.; Barisien, T.; Grousson, R.; Legrand, L.; Schott, M.; Voliotis, V. Macroscopic Coherence of a Single Exciton State in an Organic Quantum Wire. *Nat. Phys.* **2006**, *2* (1), 32–35.

(47) T. Dürkop; S. A. Getty; Enrique Cobas, A.; Fuhrer*, M. S. Extraordinary Mobility in Semiconducting Carbon Nanotubes. *Nano Lett.* **2004**, *4* (1), 35–39.

(48) Orlita, M.; Faugeras, C.; Plochocka, P.; Neugebauer, P.; Martinez, G.; Maude, D. K.; Barra, A.-L.; Sprinkle, M.; Berger, C.; de Heer, W. A.; Potemski, M. Approaching the Dirac Point in High-Mobility Multilayer Epitaxial Graphene. *Phys. Rev. Lett.* **2008**, *101* (26), 267601.

(49) Dresselhaus, M. S.; Dresselhaus, G.; Eklund, P. C. *Science of Fullerenes and Carbon Nanotubes*; Academic Press, 1996.

(50) Horowitz, G.; Hajlaoui, R.; Bourguiga, R.; Hajlaoui, M. Theory of the Organic Field-Effect Transistor. *Synth. Met.* **1999**, *101* (1), 401–404.

(51) Marcus, R. A. Electron Transfer Reactions in Chemistry. Theory and Experiment. *Rev. Mod. Phys.* **1993**, *65* (3), 599–610.

(52) Jortner, J. Temperature Dependent Activation Energy for Electron Transfer between Biological Molecules. *J. Chem. Phys.* **1976**, *64* (12), 4860.

(53) Jortner, J.; Bixon, M.; Prigogine, I. (Ilya); Rice, S. A. *Electron Transfer- from Isolated Molecules to Biomolecules*; J. Wiley, 1999.

(54) Menard, E.; Podzorov, V.; Hur, S.-H.; Gaur, A.; Gershenson, M. E.; Rogers, J. A. High-Performance N- and P-Type Single-Crystal Organic Transistors with Free-Space Gate Dielectrics. *Adv. Mater.* **2004**, *16* (23–24), 2097–2101.

(55) Briseno, A. L.; Mannsfeld, S. C. B.; Ling, M. M.; Liu, S.; Tseng, R. J.; Reese, C.; Roberts, M. E.; Yang, Y.; Wudl, F.; Bao, Z. Patterning Organic Single-Crystal Transistor Arrays. *Nature* **2006**, *444* (7121), 913–917.

(56) Marta Mas-Torrent, *, †; Murat Durkut, †; Peter Hadley, †; Xavi Ribas, ‡ and; Rovira‡, C. High Mobility of Dithiophene-Tetrathiafulvalene Single-Crystal Organic Field Effect Transistors. *J. Am. Chem. Soc.* **2004**, *126* (4), 984–985.

(57) Salleo, A. Charge Transport in Polymeric Transistors. *Mater. Today* **2007**, *10* (3), 38–45.

(58) Chang, M.; Choi, D.; Fu, B.; Reichmanis, E. Solvent Based Hydrogen Bonding: Impact on poly(3-Hexylthiophene) Nanoscale Morphology and Charge Transport Characteristics. *ACS Nano* **2013**, *7* (6), 5402–5413.

(59) Aiyar, A. R.; Hong, J.-I.; Nambiar, R.; Collard, D. M.; Reichmanis, E. Tunable Crystallinity in Regioregular Poly(3-Hexylthiophene) Thin Films and Its Impact on Field Effect Mobility. *Adv. Funct. Mater.* **2011**, *21* (14), 2652–2659.

(60) Bielecka, U.; Lutsyk, P.; Janus, K.; Sworakowski, J.; Bartkowiak, W. Effect of Solution Aging on Morphology and Electrical Characteristics of Regioregular P3HT FETs Fabricated by Spin Coating and Spray Coating. *Org. Electron.* **2011**, *12* (11), 1768–1776.

(61) Lü, A.; Ortmann, F.; Panhans, M.; Sanna, S.; Rauls, E.; Gerstmann, U.; Schmidt, W. G. Temperature-Dependent Hole Mobility and Its Limit in Crystal-Phase P3HT Calculated from First Principles. *J. Phys. Chem. B* **2016**, *120* (24), 5572–5580.

(62) Kline, R. J. A Fundamental Study of the Charge Transport and Morphology of Regioregular poly(3-Hexylthiophene). *PhD. Diss. Stanford Univ. Stanford* **2005**.

(63) Mazzio, K. A.; Rice, A. H.; Durban, M. M.; Luscombe, C. K. Effect of Regioregularity on Charge Transport and Structural and Excitonic Coherence in Poly(3-Hexylthiophene) Nanowires. *J. Phys. Chem. C* **2015**, *119* (27), 14911–14918.

(64) Chu, P.-H.; Wang, G.; Fu, B.; Choi, D.; Park, J. O.; Srinivasarao, M.; Reichmanis, E. Synergistic Effect of Regioregular and Regiorandom Poly(3-Hexylthiophene) Blends for High Performance Flexible Organic Field Effect Transistors. *Adv. Electron. Mater.* **2016**, *2* (2), 1500384.

(65) Skrypnychuk, V.; Wetzelaer, G.-J. A. H.; Gordiichuk, P. I.; Mannsfeld, S. C. B.; Herrmann, A.; Toney, M. F.; Barbero, D. R. Ultrahigh Mobility in an Organic Semiconductor by Vertical Chain Alignment. *Adv. Mater.* **2016**, *28* (12), 2359–2366.

(66) Kepler, R. G. Charge Carrier Production and Mobility in Anthracene Crystals. *Phys. Rev.* **1960**, *119* (4), 1226–1229.

(67) LeBlanc, O. H. Hole and Electron Drift Mobilities in Anthracene. *J. Chem. Phys.* **1960**, *33* (2), 626.

(68) Schouten, P. G.; Warman, J. M.; de Haas, M. P. Effect of Accumulated Radiation Dose on Pulse Radiolysis Conductivity Transients in a Mesomorphic Octa-N-Alkoxy-Substituted Phthalocyanine. *J. Phys. Chem.* **1993**, *97* (38), 9863–9870.

(69) Murgatroyd, P. N. Theory of Space-Charge-Limited Current Enhanced by Frenkel Effect. *J. Phys. D. Appl. Phys.* **1970**, *3*, 151.

(70) Street, R. A. Thin-Film Transistors. *Adv. Mater.* **2009**, *21* (20), 2007–2022.

(71) Zaumseil, J.; Sirringhaus, H. Electron and Ambipolar Transport in Organic Field-Effect Transistors. *Chem. Rev.* **2007**, *107* (4), 1296–1323.

(72) Newman, C. R.; Frisbie, C. D.; da Silva Filho, D. A.; Brédas, J.-L.; Ewbank, P. C.; Mann, K. R. Introduction to Organic Thin Film Transistors and Design of N-Channel Organic Semiconductors. *Chem. Mater.* **2004**, *16* (23), 4436–4451.

(73) Sirringhaus, H.; Tessler, N.; Friend, R. H. Integrated Optoelectronic Devices Based on Conjugated Polymers. *Sci. (80-.).* **1998**, *280* (5370), 1741–1744.

(74) Dicker, G.; de Haas, M. P.; Siebbeles, L. D. A.; Warman, J. M. Electrodeless Time-Resolved Microwave Conductivity Study of Charge-Carrier Photogeneration in Regioregular poly(3-Hexylthiophene) Thin Films. *Phys. Rev. B* **2004**, *70* (4), 45203.

(75) Thurn-Albrecht, T.; Thomann, R.; Heinzel, T.; Hugger, S. Semicrystalline Morphology in Thin Films of poly(3-Hexylthiophene). *Colloid Polym. Sci.* **2004**, *282* (8), 932–938.

(76) Cunningham, P. D.; Hayden, L. M. Carrier Dynamics Resulting from Above and Below Gap Excitation of P3HT and P3HT/PCBM Investigated by Optical-Pump Terahertz-Probe Spectroscopy †. *J. Phys. Chem. C* **2008**, *112* (21), 7928–7935.

(77) Ikawa, M.; Yamada, T.; Matsui, H.; Minemawari, H.; Tsutsumi, J.; Horii, Y.; Chikamatsu, M.; Azumi, R.; Kumai, R.; Hasegawa, T. Simple Push Coating of Polymer Thin-Film Transistors. *Nat. Commun.* **2012**, *3*, 1176.

(78) Chang, M.; Lee, J.; Kleinhenz, N.; Fu, B.; Reichmanis, E. Photoinduced Anisotropic Supramolecular Assembly and Enhanced Charge Transport of Poly(3-Hexylthiophene) Thin Films. *Adv. Funct. Mater.* **2014**, *24* (28), 4457–4465.

(79) Wang, G.; Hirasa, T.; Moses, D.; Heeger, A. J. Fabrication of Regioregular poly(3-Hexylthiophene) Field-Effect Transistors by Dip-Coating. *Synth. Met.* **2004**, *146* (2), 127–132.

(80) Wang, G.; Persson, N.; Chu, P.-H.; Kleinhenz, N.; Fu, B.; Chang, M.; Deb, N.; Mao, Y.; Wang, H.; Grover, M. A.; Reichmanis, E. Microfluidic Crystal Engineering of π-Conjugated Polymers. *ACS Nano* **2015**, *9* (8), 8220–8230.

(81) Cho, S.; Lee, K.; Yuen, J.; Wang, G.; Moses, D.; Heeger, A. J.; Surin, M.; Lazzaroni, R. Thermal Annealing-Induced Enhancement of the Field-Effect Mobility of Regioregular poly(3-Hexylthiophene) Films. *J. Appl. Phys.* **2006**, *100* (11), 114503.

(82) Aiyar, A. R.; Hong, J.-I.; Reichmanis, E. Regioregularity and Intrachain Ordering: Impact on the Nanostructure and Charge Transport in Two-Dimensional Assemblies of Poly(3-Hexylthiophene). *Chem. Mater.* **2012**, *24* (15), 2845–2853.

(83) Dimitrakopoulos, C. D.; Malenfant, P. R. L. Organic Thin Film Transistors for Large Area Electronics. *Adv. Mater.* **2002**, *14* (2), 99–117.

(84) Pei, Q.; Yu, G.; Zhang, C.; Yang, Y.; Heeger, A. J. Polymer Light-Emitting Electrochemical Cells. *Science* **1995**, *269* (5227), 1086–1088.

(85) Kang, I.; An, T. K.; Hong, J.; Yun, H.-J.; Kim, R.; Chung, D. S.; Park, C. E.; Kim, Y.-H.; Kwon, S.-K. Effect of Selenophene in a DPP Copolymer Incorporating a Vinyl Group for High-Performance Organic Field-Effect Transistors. *Adv. Mater.* **2013**, *25* (4), 524–528.

(86) Sirringhaus, H. 25th Anniversary Article: Organic Field-Effect Transistors: The Path Beyond Amorphous Silicon. *Adv. Mater.* **2014**, *26* (9), 1319–1335.

(87) Dong, H.; Fu, X.; Liu, J.; Wang, Z.; Hu, W. 25th Anniversary Article: Key Points for High-Mobility Organic Field-Effect Transistors. *Adv. Mater.* **2013**, *25* (43), 6158–6183.

(88) Tseng, H.-R.; Phan, H.; Luo, C.; Wang, M.; Perez, L. A.; Patel, S. N.; Ying, L.; Kramer, E. J.; Nguyen, T.-Q.; Bazan, G. C.; Heeger, A. J. High-Mobility Field-Effect Transistors Fabricated with Macroscopic Aligned Semiconducting Polymers. *Adv. Mater.* **2014**, *26* (19), 2993–2998.

(89) Tsao, H. N.; Cho, D.; Andreasen, J. W.; Rouhanipour, A.; Breiby, D. W.; Pisula, W.; Müllen, K. The Influence of Morphology on High-Performance Polymer Field-Effect Transistors. *Adv. Mater.* **2009**, *21* (2), 209–212.

(90) Brinkmann, M.; Hartmann, L.; Biniek, L.; Tremel, K.; Kayunkid, N. Orienting Semi-Conducting π-Conjugated Polymers. *Macromol. Rapid Commun.* **2014**, *35* (1), 9–26.

(91) Pisula, W.; Zorn, M.; Chang, J. Y.; Müllen, K.; Zentel, R. Liquid Crystalline Ordering and Charge Transport in Semiconducting Materials. *Macromol. Rapid Commun.* **2009**, *30* (14), 1179–1202.

(92) O'Connor, B. T.; Reid, O. G.; Zhang, X.; Kline, R. J.; Richter, L. J.; Gundlach, D. J.; DeLongchamp, D. M.; Toney, M. F.; Kopidakis, N.; Rumbles, G. Morphological Origin of Charge Transport Anisotropy in Aligned Polythiophene Thin Films. *Adv. Funct. Mater.* **2014**, *24* (22), 3422–3431.

(93) Surin, M.; Leclère, P.; Lazzaroni, R.; Yuen, J. D.; Wang, G.; Moses, D.; Heeger, A. J.; Cho, S.; Lee, K. Relationship between the Microscopic Morphology and the Charge Transport Properties in poly(3-Hexylthiophene) Field-Effect Transistors. *J. Appl. Phys.* **2006**, *100* (3), 33712.

(94) O'Neill, M.; Kelly, S. M. Liquid Crystals for Charge Transport, Luminescence, and Photonics. *Adv. Mater.* **2003**, *15* (14), 1135–1146.

(95) Sun, K.; Xiao, Z.; Lu, S.; Zajaczkowski, W.; Pisula, W.; Hanssen, E.; White, J. M.; Williamson, R. M.; Subbiah, J.; Ouyang, J.; Holmes, A. B.; Wong, W. W. H.; Jones, D. J. A Molecular Nematic Liquid Crystalline Material for High-Performance

Organic Photovoltaics. *Nat. Commun.* **2015**, *6*, 6013.

(96) Sirringhaus, H.; Wilson, R. J.; Friend, R. H.; Inbasekaran, M.; Wu, W.; Woo, E. P.; Grell, M.; Bradley, D. D. C. Mobility Enhancement in Conjugated Polymer Field-Effect Transistors through Chain Alignment in a Liquid-Crystalline Phase. *Appl. Phys. Lett.* **2000**, *77* (3), 406.

(97) McCulloch, I.; Heeney, M.; Bailey, C.; Genevicius, K.; MacDonald, I.; Shkunov, M.; Sparrowe, D.; Tierney, S.; Wagner, R.; Zhang, W.; Chabinyc, M. L.; Kline, R. J.; McGehee, M. D.; Toney, M. F. Liquid-Crystalline Semiconducting Polymers with High Charge-Carrier Mobility. *Nat. Mater.* **2006**, *5* (4), 328–333.

(98) Samulski, E. T.; Tobolsky, A. V. The Liquid Crystal Phase of Poly-γ-Benzyl-L-Glutamate in Solution and in the Solid State. *Mol. Cryst.* **2007**, 433–442.

(99) Park, H.-S.; Lavrentovich, O. D. Lyotropic Chromonic Liquid Crystals: Emerging Applications. In *Liquid Crystals Beyond Displays*; John Wiley & Sons, Inc.: Hoboken, NJ, USA, 2012; pp 449–484.

(100) Kim, B.-G.; Jeong, E. J.; Chung, J. W.; Seo, S.; Koo, B.; Kim, J. A Molecular Design Principle of Lyotropic Liquid-Crystalline Conjugated Polymers with Directed Alignment Capability for Plastic Electronics. *Nat. Mater.* **2013**, *12* (5), 1–6.

(101) Lu, G.; Chen, J.; Xu, W.; Li, S.; Yang, X. Aligned Polythiophene and Its Blend Film by Direct-Writing for Anisotropic Charge Transport. *Adv. Funct. Mater.* **2014**, *24* (31), 4959–4968.

(102) Bae, Y.-J.; Yang, H.-J.; Shin, S.-H.; Jeong, K.-U.; Lee, M.-H. A Novel Thin Film Polarizer from Photocurable Non-Aqueous Lyotropic Chromonic Liquid Crystal Solutions. *J. Mater. Chem.* **2011**, *21* (7), 2074.

(103) Park, M. S.; Aiyar, A.; Park, J. O.; Reichmanis, E.; Srinivasarao, M. Solvent Evaporation Induced Liquid Crystalline Phase in poly(3-Hexylthiophene). *J. Am. Chem. Soc.* **2011**, *133* (19), 7244–7247.

(104) Born, M.; Wolf, E. *Principles of Optics : Electromagnetic Theory of Propagation, Interference and Diffraction of Light*; Cambridge University Press, 1999.

(105) Clark, J.; Silva, C.; Friend, R. H.; Spano, F. C. Role of Intermolecular Coupling in

the Photophysics of Disordered Organic Semiconductors: Aggregate Emission in Regioregular Polythiophene. *Phys. Rev. Lett.* **2007**, *98* (20), 206406.

(106) Pingel, P.; Zen, A.; Abellón, R. D.; Grozema, F. C.; Siebbeles, L. D. A.; Neher, D. Temperature-Resolved Local and Macroscopic Charge Carrier Transport in Thin P3HT Layers. *Adv. Funct. Mater.* **2010**, *20* (14), 2286–2295.

(107) Zhao, K.; Khan, H. U.; Li, R.; Su, Y.; Amassian, A. Entanglement of Conjugated Polymer Chains Influences Molecular Self-Assembly and Carrier Transport. *Adv. Funct. Mater.* **2013**, *23* (48), 6024–6035.

(108) Korevaar, P. A.; de Greef, T. F. A.; Meijer, E. W. Pathway Complexity in π-Conjugated Materials. *Chem. Mater.* **2014**, *26* (1), 576–586.

(109) Knowles, T. P. J.; Waudby, C. A.; Devlin, G. L.; Cohen, S. I. A.; Aguzzi, A.; Vendruscolo, M.; Terentjev, E. M.; Welland, M. E.; Dobson, C. M. An Analytical Solution to the Kinetics of Breakable Filament Assembly. *Science* **2009**, *326* (5959), 1533–1537.

(110) Wirix, M. J. M.; Bomans, P. H. H.; Friedrich, H.; Sommerdijk, N. A. J. M.; de With, G. Three-Dimensional Structure of P3HT Assemblies in Organic Solvents Revealed by Cryo-TEM. *Nano Lett.* **2014**, *14* (4), 2033–2038.

(111) Baibarac, M.; Lapkowski, M.; Pron, A.; Lefrant, S.; Baltog, I. SERS Spectra of poly(3-Hexylthiophene) in Oxidized and Unoxidized States. *J. Raman Spectrosc.* **1998**, *29* (9), 825–832.

(112) Brown, P. J.; Sirringhaus, H.; Harrison, M.; Shkunov, M.; Friend, R. H. Optical Spectroscopy of Field-Induced Charge in Self-Organized High Mobility poly(3-Hexylthiophene). *Phys. Rev. B* **2001**, *63* (12), 125204.

(113) Snyder, R. G.; Strauss, H. L.; Elliger, C. A. Carbon-Hydrogen Stretching Modes and the Structure of N-Alkyl Chains. 1. Long, Disordered Chains. *J. Phys. Chem.* **1982**, *86* (26), 5145–5150.

(114) Österbacka, R.; Jiang, X. M.; An, C. P.; Horovitz, B.; Vardeny, Z. V. Photoinduced Quantum Interference Antiresonances in π -Conjugated Polymers. *Phys. Rev. Lett.* **2002**, *88* (22), 226401.

(115) Pottel, H.; Herreman, W.; van der Meer, B. W.; Ameloot, M. On the Significance of the Fourth-Rank Orientational Order Parameter of Fluorophores in Membranes. *Chem. Phys.* **1986**, *102* (1), 37–44.

(116) Park, M. S.; Wong, Y. S.; Park, J. O.; Venkatraman, S. S.; Srinivasarao, M. A Simple Method for Obtaining the Information of Orientation Distribution Using Polarized Raman Spectroscopy: Orientation Study of Structural Units in Poly(lactic Acid). *Macromolecules* **2011**, *44* (7), 2120–2131.

(117) Jóhannesson, H.; Furó, I.; Halle, B. Orientational Order and Micelle Size in the Nematic Phase of the Cesium Pentadecafluorooctanoate–water System from the Anisotropic Self-Diffusion of Water. *Phys. Rev. E* **1996**, *53* (5), 4904–4917.

(118) Humphries, R. L.; James, P. G.; Luckhurst, G. R. Molecular Field Treatment of Nematic Liquid Crystals. *J. Chem. Soc. Faraday Trans. 2* **1972**, *68* (0), 1031.

(119) Wu, S.-T. Infrared Markers for Determining the Order Parameters of Uniaxial Liquid Crystals. *Appl. Opt.* **1987**, *26* (16), 3434.

(120) Sheng, P. Effect of Director Fluctuations on the Nematic Distribution Function. *Solid State Commun.* **1976**, *18* (9), 1165–1167.

(121) Collins, M. E.; Soto-Cantu, E.; Cueto, R.; Russo, P. S. Separation and Characterization of Poly(tetrafluoroethylene) Latex Particles by Asymmetric Flow Field Flow Fractionation with Light-Scattering Detection. *Langmuir* **2014**, *30* (12), 3373–3380.

(122) Doty, P. Depolarization of Light Scattered from Dilute Macromolecular Solutions. I. Theoretical Discussion. *J. Polym. Sci.* **1948**, *3* (5), 750–762.

(123) Doty, P.; Stein, S. J. Depolarization of Light Scattered from Dilute Macromolecular Solutions. II. Experimental Results. *J. Polym. Sci.* **1948**, *3* (5), 763–771.

(124) Striegel*, A. M. A Method for Studying Optical Anisotropy of Polymers As a Function of Molar Mass. *Anal. Chem.* **2002**, *74* (13), 3013–3018.

(125) Patricia M. Cotts*, †; And, T. M. S.; Zhou, Q. Equilibrium Flexibility of a Rigid Linear Conjugated Polymer. *Macromolecules* **1996**, *29* (23), 7323–7328.

(126) Yue, S.; Berry, G. C.; Green, M. M. Intermolecular Association and Supramolecular Organization in Dilute Solution. 2. Light Scattering and Optical Activity of Poly (P-Biphenylylmethyl L-Glutamate). *Macromolecules* **1996**, *29* (19), 6175–6182.

(127) G. Petekidis, †; D. Vlassopoulos, *; G. Fytas, A.; Kountourakis, N.; Kumar, S. Association Dynamics in Solutions of Hairy-Rod Polymers. *Macromolecules* **1997**, *30* (4), 919–931.

(128) Norberto Micali, *; Valentina Villari, †; Maria Angela Castriciano, ‡; Andrea Romeo, ‡ and; Luigi Monsù Scolaro*, ‡. From Fractal to Nanorod Porphyrin J-Aggregates. Concentration-Induced Tuning of the Aggregate Size. *J. Phys. Chem. B* **2006**, *110* (16), 8289–8295.

(129) Yamamoto, T.; Yamada, W.; Takagi, M.; Kizu, K.; Maruyama, T.; Ooba, N.; Tomaru, S.; Kurihara, T.; Kaino, T.; Kubota, K. π-Conjugated Soluble Poly(aryleneethynylene) Type Polymers. Preparation by Palladium-Catalyzed Coupling Reaction, Nonlinear Optical Properties, Doping, and Chemical Reactivity. *Macromolecules* **1994**, *27* (22), 6620–6626.

(130) Nikolai G. Khlebtsov, *,†, ‡; Andrei G. Melnikov, †; Vladimir A. Bogatyrev, †; Lev A. Dykman, †; Anna V. Alekseeva, †; Lyubov A. Trachuk, † and; Khlebtsov†, B. N. Can the Light Scattering Depolarization Ratio of Small Particles Be Greater Than 1/3? *J. Phys. Chem. B* **2005**, *109* (28), 13578–13584.

(131) Kubota, K.; Urabe, H.; Tominaga, Y. Spectrum of Light Quasi-Elastically Scattered from Suspensions of Tobacco Mosaic Virus. Experimental Study of Anisotropy in Translational Diffusion. *Macromolecules* **1984**, *17* (10), 2096–2104.

(132) Randy Cush; Derek Dorman, A.; Russo*, P. S. Rotational and Translational Diffusion of Tobacco Mosaic Virus in Extended and Globular Polymer Solutions. *Macromolecules* **2004**, *37* (25), 9577–9584.

(133) Yue, S.; Berry, G. C.; McCullough, R. D. Intermolecular Association and Supramolecular Organization in Dilute Solution. 1. Regioregular Poly(3-Dodecylthiophene). *Macromolecules* **1996**, *29* (3), 933–939.

(134) Khlebtsov, B. N.; Khanadeev, V. A.; Khlebtsov, N. G. Attenuation, Scattering, and Depolarization of Light by Gold Nanorods with Silver Shells. *Opt. Spectrosc.* **2010**, *108* (1), 59–69.

(135) Yang, H. Single-Particle Light Scattering: Imaging and Dynamical Fluctuations in the Polarization and Spectral Response. *J. Phys. Chem. A* **2007**, *111* (23), 4987–4997.

(136) Koch, A. H. R.; Lévêque, G.; Harms, S.; Jaskiewicz, K.; Bernhardt, M.; Henkel, A.; Sönnichsen, C.; Landfester, K.; Fytas, G. Surface Asymmetry of Coated Spherical Nanoparticles. *Nano Lett.* **2014**, *14* (7), 4138–4144.

(137) Flory, P. J. Molecular Theory of Liquid Crystals; Springer Berlin Heidelberg, 1984; pp 1–36.

(138) Wirix, M. J. M.; Bomans, P. H. H.; Hendrix, M. M. R. M.; Friedrich, H.; Sommerdijk, N. A. J. M.; de With, G. Visualizing Order in Dispersions and Solid State Morphology with Cryo-TEM and Electron Tomography: P3HT : PCBM Organic Solar Cells. *J. Mater. Chem. A* **2015**, *3* (9), 5031–5040.

(139) Kleinhenz, N.; Rosu, C.; Chatterjee, S.; Chang, M.; Nayani, K.; Xue, Z.; Kim, E.; Middlebrooks, J.; Russo, P. S.; Park, J. O.; Srinivasarao, M.; Reichmanis, E. Liquid Crystalline Poly(3-Hexylthiophene) Solutions Revisited: Role of Time-Dependent Self-Assembly. *Chem. Mater.* **2015**, *27* (7), 2687–2694.

(140) Park, B.; Ko, D.-H. Charge Transport in Ordered and Disordered Regions in Pristine and Sonicated-Poly(3-Hexylthiophene) Films. *J. Phys. Chem. C* **2014**, *118* (3), 1746–1752.

(141) Choi, D.; Chang, M.; Reichmanis, E. Controlled Assembly of Poly(3-Hexylthiophene): Managing the Disorder to Order Transition on the Nano- through Meso-Scales. *Adv. Funct. Mater.* **2015**, *25* (6), 920–927.

(142) Turner, S. T.; Pingel, P.; Steyrleuthner, R.; Crossland, E. J. W.; Ludwigs, S.; Neher, D. Quantitative Analysis of Bulk Heterojunction Films Using Linear Absorption Spectroscopy and Solar Cell Performance. *Adv. Funct. Mater.* **2011**, *21* (24), 4640–4652.

(143) Clark, J.; Chang, J.-F.; Spano, F. C.; Friend, R. H.; Silva, C. Determining Exciton Bandwidth and Film Microstructure in Polythiophene Films Using Linear Absorption Spectroscopy. *Appl. Phys. Lett.* **2009**, *94* (16), 163306.

(144) Clark, J.; Chang, J.-F.; Spano, F. C.; Friend, R. H.; Silva, C. Determining Exciton Bandwidth and Film Microstructure in Polythiophene Films Using Linear

Absorption Spectroscopy. *Appl. Phys. Lett.* **2009**, *94* (16), 163306.

(145) Manas, E. S.; Spano, F. C. Absorption and Spontaneous Emission in Aggregates of Conjugated Polymers. *J. Chem. Phys.* **1998**, *109* (18), 8087.

(146) Beljonne, D.; Cornil, J.; Silbey, R.; Millié, P.; Brédas, J. L. Interchain Interactions in Conjugated Materials: The Exciton Model versus the Supermolecular Approach. *J. Chem. Phys.* **2000**, *112* (10), 4749.

(147) Barford, W. *Exciton Transfer Integrals Between Polymer Chains*; 2007.

(148) Cornil, J.; dos Santos, D. A.; Crispin, X.; Silbey, R.; Brédas, J. L. Influence of Interchain Interactions on the Absorption and Luminescence of Conjugated Oligomers and Polymers: A Quantum-Chemical Characterization. *J. Am. Chem. Soc.* **1998**, *120* (6), 1289–1299.

(149) Gierschner, J.; Huang, Y.-S.; Van Averbeke, B.; Cornil, J.; Friend, R. H.; Beljonne, D. Excitonic versus Electronic Couplings in Molecular Assemblies: The Importance of Non-Nearest Neighbor Interactions. *J. Chem. Phys.* **2009**, *130* (4), 44105.

(150) Spano, F. C.; Silva, C. H- and J-Aggregate Behavior in Polymeric Semiconductors. *Annu. Rev. Phys. Chem.* **2014**, *65* (1), 477–500.

(151) Spano, F. C. Modeling Disorder in Polymer Aggregates: The Optical Spectroscopy of Regioregular poly(3-Hexylthiophene) Thin Films. *J. Chem. Phys.* **2005**, *122* (23), 234701.

(152) Usov, I.; Mezzenga, R. FiberApp: An Open-Source Software for Tracking and Analyzing Polymers, Filaments, Biomacromolecules, and Fibrous Objects. *Macromolecules* **2015**, *48* (5), 1269–1280.

(153) Onsager, L. THE EFFECTS OF SHAPE ON THE INTERACTION OF COLLOIDAL PARTICLES. *Ann. N. Y. Acad. Sci.* **1949**, *51* (4), 627–659.

(154) Jordens, S.; Isa, L.; Usov, I.; Mezzenga, R. Non-Equilibrium Nature of Two-Dimensional Isotropic and Nematic Coexistence in Amyloid Fibrils at Liquid Interfaces. *Nat. Commun.* **2013**, *4*, 1917.

(155) Keum, J. K.; Xiao, K.; Ivanov, I. N.; Hong, K.; Browning, J. F.; Smith, G. S.; Shao, M.; Littrell, K. C.; Rondinone, A. J.; Andrew Payzant, E.; Chen, J.; Hensley, D. K. Solvent Quality-Induced Nucleation and Growth of Parallelepiped Nanorods in Dilute poly(3-Hexylthiophene) (P3HT) Solution and the Impact on the Crystalline Morphology of Solution-Cast Thin Film. *CrystEngComm* **2013**, *15* (6), 1114–1124.

(156) Liem, H.-M.; Etchegoin, P.; Whitehead, K. S.; Bradley, D. D. C. Raman Anisotropy Measurements: An Effective Probe of Molecular Orientation in Conjugated Polymer Thin Films. *Adv. Funct. Mater.* **2003**, *13* (1), 66–72.

(157) Welch, P.; Muthukumar, M. Molecular Mechanisms of Polymer Crystallization from Solution. *Phys. Rev. Lett.* **2001**, *87* (21), 218302.

(158) Liu, J.; Haynes, D.; Balliet, C.; Zhang, R.; Kowalewski, T.; McCullough, R. D. Self Encapsulated Poly(3-Hexylthiophene)-Poly(fluorinated Alkyl Methacrylate) Rod-Coil Block Copolymers with High Field Effect Mobilities on Bare SiO2. *Adv. Funct. Mater.* **2012**, *22* (5), 1024–1032.

(159) Sirringhaus, H.; Brown, P. J.; Friend, R. H.; Nielsen, M. M.; Bechgaard, K.; Langeveld-Voss, B. M. W.; Spiering, A. J. H.; Janssen, R. A. J.; Meijer, E. W.; Herwig, P.; de Leeuw, D. M. Two-Dimensional Charge Transport in Self-Organized, High-Mobility Conjugated Polymers. *Nature* **1999**, *401* (6754), 685–688.

(160) Scherrer, P. Bestimmung der Größe und der inneren Struktur von Kolloidteilchen mittels Röntgenstrahlen. *Nachrichten von der Gesellschaft der Wissenschaften zu Göttingen, Math. Klasse 1918*, 98–100.

(161) Perez, L. A.; Zalar, P.; Ying, L.; Schmidt, K.; Toney, M. F.; Nguyen, T.-Q.; Bazan, G. C.; Kramer, E. J. Effect of Backbone Regioregularity on the Structure and Orientation of a Donor–Acceptor Semiconducting Copolymer. *Macromolecules* **2014**, *47* (4), 1403–1410.

(162) Duong, D. T.; Ho, V.; Shang, Z.; Mollinger, S.; Mannsfeld, S. C. B.; Dacuña, J.; Toney, M. F.; Segalman, R.; Salleo, A. Mechanism of Crystallization and Implications for Charge Transport in Poly(3-Ethylhexylthiophene) Thin Films. *Adv. Funct. Mater.* **2014**, *24* (28), 4515–4521.

(163) Lucovsky, G.; Wu, Y.; Niimi, H.; Misra, V.; Phillips, J. C. Bonding Constraints and Defect Formation at Interfaces between Crystalline Silicon and Advanced Single Layer and Composite Gate Dielectrics. *Appl. Phys. Lett.* **1999**, *74* (14), 2005.

(164) Kwiatkowski, J. J.; Jimison, L. H.; Salleo, A.; Spakowitz, A. J. A Boltzmann-Weighted Hopping Model of Charge Transport in Organic Semicrystalline Films. *J. Appl. Phys.* **2011**, *109* (11), 113720.

(165) Kleinhenz, N.; Persson, N.; Xue, Z.; Chu, P. H.; Wang, G.; Yuan, Z.; McBride, M. A.; Choi, D.; Grover, M. A.; Reichmanis, E. Ordering of Poly(3-Hexylthiophene) in Solutions and Films: Effects of Fiber Length and Grain Boundaries on Anisotropy and Mobility. *Chem. Mater.* **2016**, *28* (11), 3905–3913.

(166) Diao, Y.; Shaw, L.; Bao, Z.; Mannsfeld, S. C. B. Morphology Control Strategies for Solution-Processed Organic Semiconductor Thin Films. *Energy Environ. Sci.* **2014**, *7* (7), 2145–2159.

(167) Søndergaard, R. R.; Hösel, M.; Krebs, F. C. Roll-to-Roll Fabrication of Large Area Functional Organic Materials. *J. Polym. Sci. Part B Polym. Phys.* **2013**, *51* (1), 16–34.

(168) Toney, M. F.; Russell, T. P.; Logan, J. A.; Kikuchi, H.; Sands, J. M.; Kumar, S. K. Near-Surface Alignment of Polymers in Rubbed Films. *Nature* **1995**, *374* (6524), 709–711.

(169) Grell, M.; Knoll, W.; Lupo, D.; Meisel, A.; Miteva, T.; Neher, D.; Nothofer, H.-G.; Scherf, U.; Yasuda, A. Blue Polarized Electroluminescence from a Liquid Crystalline Polyfluorene. *Adv. Mater.* **1999**, *11* (8), 671.

(170) Wittmann, J. C.; Smith, P. Highly Oriented Thin Films of Poly(tetrafluoroethylene) as a Substrate for Oriented Growth of Materials. *Nature* **1991**, *352* (6334), 414–417.

(171) Misaki, M.; Ueda, Y.; Nagamatsu, S.; Yoshida, Y.; Tanigaki, N.; Yase, K. Formation of Single-Crystal-like Poly(9,9-Dioctylfluorene) Thin Film by the Friction-Transfer Technique with Subsequent Thermal Treatments. *Macromolecules* **2004**, *37* (18), 6926–6931.

(172) Shaw, L.; Hayoz, P.; Diao, Y.; Reinspach, J. A.; To, J. W. F.; Toney, M. F.; Weitz, R. T.; Bao, Z. Direct Uniaxial Alignment of a Donor–Acceptor Semiconducting Polymer Using Single-Step Solution Shearing. *ACS Appl. Mater. Interfaces* **2016**, *8* (14), 9285–9296.

(173) Schott, S.; Gann, E.; Thomsen, L.; Jung, S.-H.; Lee, J.-K.; McNeill, C. R.; Sirringhaus, H. Charge-Transport Anisotropy in a Uniaxially Aligned

Diketopyrrolopyrrole-Based Copolymer. *Adv. Mater.* **2015**, *27* (45), 7356–7364.

(174) Choi, D.; Kim, H.; Persson, N.; Chu, P.-H.; Chang, M.; Kang, J.-H.; Graham, S.; Reichmanis, E. Elastomer–Polymer Semiconductor Blends for High-Performance Stretchable Charge Transport Networks. *Chem. Mater.* **2016**, *28* (4), 1196–1204.

(175) Persson, N. E.; McBride, M. A.; Grover, M. A.; Reichmanis, E. Automated Analysis of Orientational Order in Images of Fibrillar Materials. *Chem. Mater.* **2016**, acs.chemmater.6b01825.

(176) Murphy, J. N.; Harris, K. D.; Buriak, J. M. Automated Defect and Correlation Length Analysis of Block Copolymer Thin Film Nanopatterns. *PLoS One* **2015**, *10* (7), e0133088.

(177) Ping-Hsun Chu, Nabil Kleinhenz, Nils Persson, Michael McBride, Jeff L. Hernandez, Boyi Fu, Guoyan Zhang, and E. R. Toward Precision Control of Nanofiber Orientation in Conjugated Polymer Thin Films: Impact on Charge Transport. *Submitted*.

(178) Bi, D.; Xu, B.; Gao, P.; Sun, L.; Grätzel, M.; Hagfeldt, A. Facile Synthesized Organic Hole Transporting Material for Perovskite Solar Cell with Efficiency of 19.8%. *Nano Energy* **2016**, *23*, 138–144.

(179) Conings, B.; Baeten, L.; De Dobbelaere, C.; D'Haen, J.; Manca, J.; Boyen, H.-G. Perovskite-Based Hybrid Solar Cells Exceeding 10% Efficiency with High Reproducibility Using a Thin Film Sandwich Approach. *Adv. Mater.* **2014**, *26* (13), 2041–2046.

(180) Kwiatkowski, J. J.; Jimison, L. H.; Salleo, A.; Spakowitz, A. J. A Boltzmann-Weighted Hopping Model of Charge Transport in Organic Semicrystalline Films. *J. Appl. Phys.* **2011**, *109* (11), 113720.

(181) Schneider, C. A.; Rasband, W. S.; Eliceiri, K. W. NIH Image to ImageJ: 25 Years of Image Analysis. *Nat. Methods* **2012**, *9* (7), 671–675.

(182) Berne, B. J.; Pecora, R. *Dynamic Light Scattering : With Applications to Chemistry, Biology, and Physics*; Dover Publications, 1976.

(183) Riseman, J.; Kirkwood, J. G. The Intrinsic Viscosity, Translational and Rotatory

Diffusion Constants of Rod-Like Macromolecules in Solution. *J. Chem. Phys.* **1950**, *18* (4), 512.